RIJKSUNIVERSITEIT GRONINGEN

Measuring MRI noise

Proefschrift

ter verkrijging van het doctoraat in de
Wiskunde en Natuurwetenschappen
aan de Rijksuniversiteit Groningen
op gezag van de
Rector Magnificus, dr. F. Zwarts,
in het openbaar te verdedigen op
vrijdag 27 mei 2005
om 16.15 uur

door

Gerke Jan Hoiting
geboren op 3 juni 1975
te Groningen

Promotor: prof. dr. ir. H. Duifhuis

Beoordelingscommissie: prof. dr. L.P. Kok
prof. dr. V. Mellert
prof. dr. ir. N.B. Roozen

ISBN 90-367-2234-9

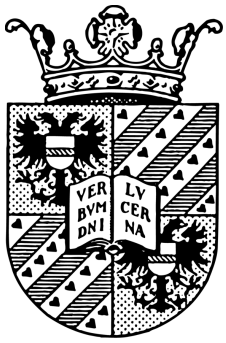

Verbum Domini lucerna pedibus nostris

Het Woord van de HEER is een lamp voor mijn voet

psalm 119: 105

Paranimfen: Jelle Bezemer
Remco Renken

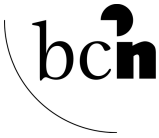

The research presented in this thesis has been conducted in the Graduate School of Behavioral and Cognitive Neurosciences BCN.

Printed by PrintPartners Ipskamp, www.ppi.nl

Published by Bibliotheek der Rijks*universiteit* Groningen

ISBN 90-367-2234-9
ISBN 90-367-2235-7 (Online version)

Contents

1 Introduction **1**

2 Introduction MRI **5**
2.1 MR physics 5
2.2 MR imaging 8
2.3 Gradient magnetic fields 9
2.4 MRI scanner system 9

3 Theory **13**
3.1 Lorentz forces acting on gradient coils 13
3.2 Sound 13
3.3 Transfer function 15
3.4 Harmonic distortion 15
3.5 Sound pressure transfer function 16
3.6 Frequency sweep response 18
3.7 Digitizing signals 18
3.8 Windowing 19

4 Materials and methods **21**
4.1 Materials 21
4.2 Signals 22
4.2.1 Signals at 1.5 T 22
4.2.2 Signals at 3 T 22
4.3 Methods 23
4.3.1 Fourier analysis 24
4.3.2 Root-mean-square 24

5 Towards a more silent scanner; an analysis of sound reducing methods **27**
5.1 Introduction 27
5.2 Sound sources in the scanner room 28
5.2.1 Air-handling system 28
5.2.2 Liquid helium pump 28

5.2.3 Electric current leads . . . 29
5.2.4 Eddy currents . . . 29
5.2.5 Gradient coil noise . . . 29
5.3 Effects of acoustic noise . . . 29
5.3.1 Hearing threshold shift . . . 29
5.3.2 Discomfort and anxiety . . . 30
5.3.3 Confounding stimulus . . . 31
5.4 Sound reducing methods . . . 31
5.4.1 Passive methods . . . 32
5.4.2 Active methods . . . 36
5.4.3 Silent sequences . . . 40
5.5 General issues . . . 44
5.6 Discussion and conclusion . . . 45

6 Determining the acoustic transfer function with frequency sweep signals 47
6.1 Introduction . . . 47
6.2 Results . . . 47
6.2.1 Fourier analysis . . . 48
6.2.2 Root-mean-square . . . 51
6.3 Discussion . . . 55
6.4 Conclusions . . . 57

7 Comparison of transfer functions 59
7.1 Introduction . . . 59
7.2 Results . . . 59
7.2.1 Noise response . . . 59
7.2.2 Pulse response . . . 60
7.2.3 Frequency sweep response . . . 61
7.3 Discussion . . . 64
7.4 Conclusions . . . 66

8 Considerations in laser Doppler interferometry of MR scanner bore vibrations 67
8.1 Introduction . . . 67
8.2 Laser interferometers . . . 68
8.2.1 Mach-Zehnder based interferometer . . . 68
8.2.2 Mach-Zehnder based interferometer with fibers . . . 69
8.3 Theory laser Doppler interferometer . . . 69
8.3.1 Doppler shift . . . 69
8.3.2 Interferometry . . . 71
8.3.3 Measured vibrational data . . . 73
8.4 Optical considerations . . . 73
8.5 Practical considerations . . . 75

8.6 Problems/restrictions 77
8.6.1 Placement and alignment 77
8.6.2 Limits of LDI 79
8.7 Conclusion 80

9 Conclusion **81**
9.1 Summary and conclusions 81
9.2 Perspectives 82

A Acquisition **85**
A.1 Acquisition program 85
A.2 Acquisition hardware 87

B Mathematical derivations **89**
B.1 Fourier transform of frequency sweep signal 89
B.2 Noise cancellation 90

Bibliography **91**

Samenvatting **99**

Dankwoord **103**

Chapter 1

Introduction

The interaction between the strong magnetic field of a Magnetic Resonance Imaging (MRI) scanner and changing electric currents in its gradient coils turns the scanner into a giant loudspeaker. The acoustic noise produced by an MRI scanner is a serious threat for persons in the scanner, as well as for persons in the scanner room (Brummett *et al.* [1988]; Cho *et al.* [1997]; McJury *et al.* [1994]). Sound pressure levels of 110 dB are common and levels over 130 dB have been measured for high magnetic field scanners (Counter *et al.* [2000]; Foster *et al.* [2000]; McJury and Shellock [2000]; Price *et al.* [2001]; Ravicz *et al.* [2000]). MRI is used not only to obtain anatomical images, but also for functional brain mapping; during this functional imaging (fMRI), the produced sound is a confounding stimulus. In particular, this affects functional imaging of brain activation by auditory stimuli (Ravicz and Melcher [2001]; Talavage *et al.* [1999]). Furthermore, this unwanted side effect causes anxiety, distraction, results in (auditory) brain stimulation not related to the task at hand, and possibly causes hearing damage (Bandettini *et al.* [1998]; Brummett *et al.* [1988]; Cho *et al.* [1998a]; Elliott *et al.* [1999]; Mazard *et al.* [2002]).

Several methods have been investigated to reduce vibration at the gradient coils (Mansfield *et al.* [1995]; Kuijpers [1999]), to block the conduction pathway (Katsunuma *et al.* [2002]), and to reduce the airborne acoustic output (Moelker *et al.* [2003a]). Without modifications to the scanner or the scanner room, the acoustic output of the scanner can be reduced by changing the frequency content of the pulse sequences (Hedeen and Edelstein [1997]; Tomasi and Ernst [2003]). The above issues are discussed in **chapter 5**.

It is almost impossible to make physical modifications to an MRI scanner in a clinical setting. Modifications to the scanner for sound reducing measures are typically done by MRI manufacturers. The only property that can be altered during normal operation of a scanner is the pulse sequence that is used for scanning. A pulse sequence defines the way in which the magnetic field is changed to obtain location information. In principle, when scanning starts, the time courses of the

electric gradient currents are known (Bilecen *et al.* [1998]; Chapman *et al.* [2003]; Cho *et al.* [1998b]; de Zwart *et al.* [2002]; Hedeen and Edelstein [1997]). They depend on scanning parameters like the repetition time (TR), the echo time (TE), and the field of view (FOV). Hence, adjustments of these parameters affect the gradient currents, in time as well as in spectrum (Tomasi and Ernst [2003]). Such a pulse sequence controls the electric gradient currents. The vibrations arising from the gradient currents contain the same frequencies as the gradient currents. This methodology, together with the physical principles of MRI, are treated in **chapter 2**.

The amplitude of the vibrations is depending on the acoustic transfer of the scanner system. This transfer is a function of frequency, and is high at the resonance frequencies of the scanner. To reduce the sound pressure produced by a scanner, these resonance frequencies should be avoided in the gradient current. When the acoustic transfer function of the gradient system is known, it should be straightforward to calculate the acoustic noise generated by the gradient currents (Hedeen and Edelstein [1997]). However, the acoustic output is not necessarily linear with the input (Moelker *et al.* [2003b]), and not only the frequencies in the electric current are found in the scanner noise, *e.g.*, the spectrum of the output may also show nonlinear components. Such components hamper a simple input-output analysis. In the theory, **chapter 3**, the standard definition of the transfer function is given by the division of output and input spectra. In the same chapter a proposal is given for a new transfer function, the sound pressure transfer function, that takes nonlinearities into account. This transfer function is derived with a root-mean-square method, which relates closely to the determination of sound pressure levels. Furthermore, in this chapter, additional theoretical background for the following chapters is given.

The frequency sweep signals used in chapters 6 and 7 evoke all frequencies of interest consecutively, in contrast to impulse response or noise response measurements. That makes these signals suitable for the derivation of the sound pressure transfer function. In the Materials and methods chapter (**chapter 4**), all variations with sweep rate and amplitude are described, as well as the settings for pulse response and noise response measurements. Further, the frequency signal response is not only analyzed with the proposed method, but also with the conventional method. The analysis methods are described in detail in this chapter.

With the proposed method for a sound pressure transfer function (**section 3.5**), the objective is not to find the exact sound a scanner will produce. For that, a function is needed that also calculates nonlinearities, *e.g.*, the production of harmonic distortion or overtones. In this work, the aim is to find the *sound pressure* transfer function. The electric gradient current time signal convolved with this transfer function will give a time signal that predicts the sound pressure, and not so much the real sound of a scanner. With this sound pressure time signal, the sound pressure level can be calculated. This sound pressure level is subjected to standards regarding exposure levels, and exposure time.

The sweep rate of the frequency modulated signals is bounded by the use of

time-averaging in the root-mean-square method. In **chapter 6**, the frequency sweep signals are varied over sweep rate and amplitude. The transfer functions are both derived with Fourier transforms and root-mean-square analysis. As expected, the transfer function cannot be derived with a sensible accuracy when the sweep rate becomes too high. Further, it is shown that harmonic distortion is high in the scanner noise. The major differences between the analysis methods are found where the transfer is low. Neglecting the harmonic distortion leads to wrong predictions of the sound pressure levels at these frequencies of low transfer. From these experiments, it becomes clear that the acoustic noise does not linearly depend on the input signal amplitude.

The frequency sweep experiments described in **chapter 7** make use of only one sweep rate. The analysis of these data leads to the same conclusions as in chapter 6. The results are compared with the transfer functions derived with pink noise and pulses. With such signals, no discrimination can be made between first and second-order responses. Frequency sweep signals provide a good control over frequency and amplitude, in contrast to noise signals (amplitude) and pulse signals (frequency).

Not all parts of the scanner's surface vibrate as much as other parts. By probing the scanner with one microphone at one location, no information on this phenomenon can be extracted. With laser Doppler interferometry the surface vibrations can be measured in a noncontact manner. When the complete scanner surface responses are known, the surface responses to gradient currents can be modelled. With this information, the sound field can be calculated, as sound pressure distributions. In **chapter 8**, the possible difficulties with laser Doppler measurements of scanner bore vibrations are discussed. After solving all technical difficulties, time seems to be the biggest constraint of such measurements.

Chapter 2

Introduction MRI

2.1 MR physics

Protons and neutrons have an intrinsic angular momentum, called spin. The combination of these particles in a nucleus, possesses a total angular momentum $\hbar\vec{I}$. Nuclear spin is the term often used to represent this total angular momentum of a nucleus. A characteristic of a nucleus is that with an even mass number, it has integer spin ($I = 0, 1, \ldots$), and a nucleus with an odd mass number has half-integer spin ($I = \frac{1}{2}, \frac{3}{2}, \ldots$). As a result of the rotating charge (figure 2.1A), these nuclei have a magnetic moment $\vec{\mu}$, with

$$\vec{\mu} = \gamma\hbar\vec{I}, \tag{2.1}$$

with γ the gyromagnetic ratio for the specific nucleus. When placed inside a magnetic field, this magnetic moment tends to align with the applied magnetic field. The quantization of the magnetic moment results in a misalignment with the magnetic field. The nucleus experiences a torque due to this misalignment, causing a precessional movement around the applied magnetic field (figure 2.1B). The angular frequency ω_L (Larmor frequency) of this movement is given by

$$\omega_L = \gamma B, \tag{2.2}$$

where B is the local magnetic field strength.

In an ensemble of nuclei, all the magnetic moments add to give the magnetization $\vec{M}$:

$$\vec{M} = \sum_i \vec{\mu}_i. \tag{2.3}$$

At room temperature, due to the Brownian motion, the ensemble has no net magnetization due to random orientation of the magnetic moments (figure 2.2A). Inside a magnetic field, the quantization of the magnetic moments results in parallel and

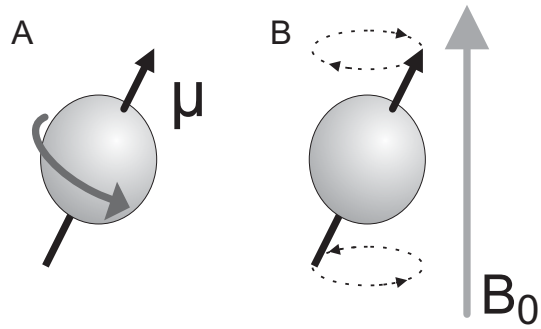

Figure 2.1: A: A nucleus has a property called spin. The spinning positive charge causes a magnetic moment μ. B: Inside a magnetic field, B_0, the magnetic moment aligns with the magnetic field. Due to quantum spin states, the alignment is not perfect. The resulting torque on the magnetic moment makes it spin with the Larmor angular frequency ω_L.

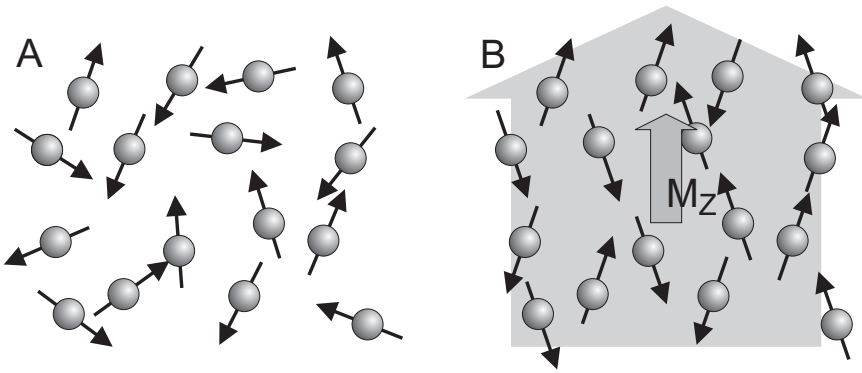

Figure 2.2: A: At room temperature, no net magnetization exists due to Brownian motion. B: Inside a magnetic field, B_0, the magnetic moments aligns with the magnetic field. There is a slight preference for the parallel alignment.

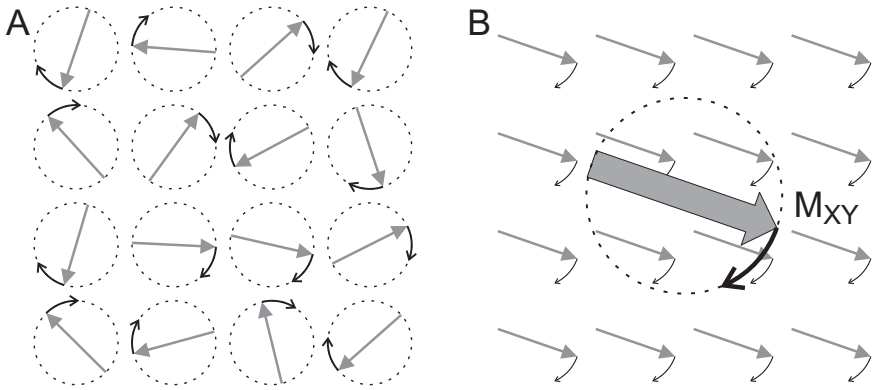

Figure 2.3: Top view of the system depicted in figure 2.2B. A: The phases are randomly distributed, and there is no net transversal magnetization. B: After an RF pulse, the precession of the $N_{\mathrm{p}} - N_{\mathrm{ap}}$ magnetic moments in the parallel state is in-phase, resulting in a transverse magnetization.

anti-parallel alignment. For protons ($I = \frac{1}{2}$), there are two states, which are populated by about the same number of protons. There is a slight preference for the parallel alignment. The population difference $N_{\mathrm{p}} - N_{\mathrm{ap}}$ (p for parallel, ap for anti-parallel), causes a longitudinal magnetization M_Z (figure 2.2B). The population ratio at equilibrium is given by the Boltzmann factor for the energy difference $\gamma\hbar B$:

$$\frac{N_{\mathrm{ap}}}{N_{\mathrm{p}}} = \exp(-\frac{\gamma\hbar B}{k_B T}), \tag{2.4}$$

with k_B Boltzmann's constant, and T the absolute temperature (Kittel [1996]).

In the following, only the population difference $N_{\mathrm{p}} - N_{\mathrm{ap}}$ at thermal equilibrium is considered. In the transversal plane, perpendicular to the magnetic field B_0, there is also no magnetization in the absence of a magnetic field (figure 2.3A). A radio frequency (RF) pulse, matching the Larmor frequency, can alter the state of the individual magnetic moments. The anti-parallel state becomes occupied, and the parallel state becomes less occupied. This leads to a decrease of the longitudinal magnetization. The RF signal makes the magnetic moments precess in coherent phase, as well. The ensemble of magnetic moments produces a transverse magnetization (M_{XY}) due to this in-phase precessing (figure 2.3B), which rotates with the Larmor frequency. A receiver can be set to detect this transverse magnetization.

The return to the favored parallel alignment state is a stochastic process with a time constant T_1. The energy difference between the favored parallel alignment state and the anti-parallel state, $\hbar\omega_L = \gamma\hbar B$, is dissipated as heat to the ensemble. This return to thermal equilibrium leads to an increase of the longitudinal magnetization. Although the transverse and longitudinal magnetization are components of one magnetization, the decay time T_2 of the transversal magnetization is shorter

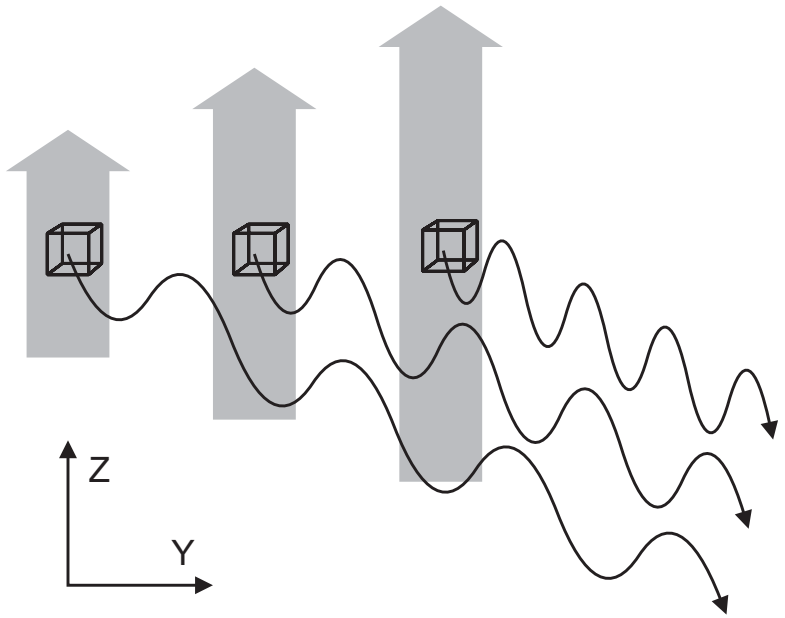

Figure 2.4: The frequency of rotation of the transverse magnetization depends on the local magnetic field strength. Different volume elements therefore emit electromagnetic waves with different frequencies. This radiation is received with an antenna.

than T_1. The spins interact with each other, resulting in dephasing (returning to the state of figure 2.3A), leading to a decrease of the transverse magnetization. Dephasing, however, does not influence the state of the individual magnetic moments which determine the longitudinal magnetization (Sanders [1995]).

2.2 MR imaging

After exciting the spins with an RF pulse, the frequency of precession can be modified by applying a gradient G to the magnetic field (figure 2.4). Seen along a line, the Larmor frequency is now depending on location x:

$$\omega_L(x) = \gamma\big(B + G(x)\big). \tag{2.5}$$

When taking the Fourier transform of the receiver signal, the different frequencies are coding for location, while the amplitude of the spectrum at several frequencies is depending on nucleus abundance.

The time integral of the measurement gradient corresponds to a value k:

$$k = \gamma \int G\mathrm{d}t, \tag{2.6}$$

with $k_x = \int G_x \mathrm{d}t$, *et cetera*, where k is the symbol for wave number, the Fourier transform of coordinates. All volume elements emit RF signals that add to one MR signal. Recording MR signals is as if k space is filled. With one gradient strength, one k line is produced. For different gradient strengths, other k lines are produced. If k space is full, then a 2D-Fourier transform results in a 'space' representation of the data: the well-known MR images.

From equation 2.6, it is clear that longer measuring, with one gradient strength, leads to a larger k space. This produces images with a better spatial resolution. In general, image resolution is enhanced by stronger gradients or longer measurement time. Traversing the same k space in a shorter time, requires stronger gradients.

2.3 Gradient magnetic fields

The spatial variation of the magnetic field over space, due to the application of gradient magnetic fields, is well known. To acquire several k lines, these have to be selected by the appropriate gradients in the perpendicular directions; with gradients in three orthogonal directions the imaging volume can be scanned entirely.

It should be noted that the gradient magnetic fields vary the main magnetic field in the direction of this main magnetic field:

$$G(x) = \frac{\partial B_z}{\partial x}, \quad G(y) = \frac{\partial B_z}{\partial y}, \quad G(z) = \frac{\partial B_z}{\partial z}. \tag{2.7}$$

2.4 MRI scanner system

These gradient fields in the three orthogonal directions are produced with the gradient coils. Extra magnetic fields are produced by these coils, which on superposition to the main magnetic field, produce linear gradient magnetic fields. The gradient coil array is often a molded construction, containing a complex structure of conducting wires. The total length of wires is several hundreds of meters, carrying currents of up to several hundreds of amperes. Lorentz forces acting on the gradient coils can therefore be as high as 10^5 N.

The imaging-volume is located inside the static magnetic field; this field is commonly generated by electric currents flowing through magnet coils. These coils are inside a dewar containing liquid helium to make the coils superconductive; the electric currents flowing without resistance make that the static magnetic field is maintained very stably. Field homogeneity is very important for imaging. Inhomogeneities are compensated for with strategically placed blocks of iron for shimming.

The superconducting coils attract each other with a force in the order of 10^6 N; the structure needs to withstand these internal forces and be able to withstand the low temperature ($\sim$ 4 K).

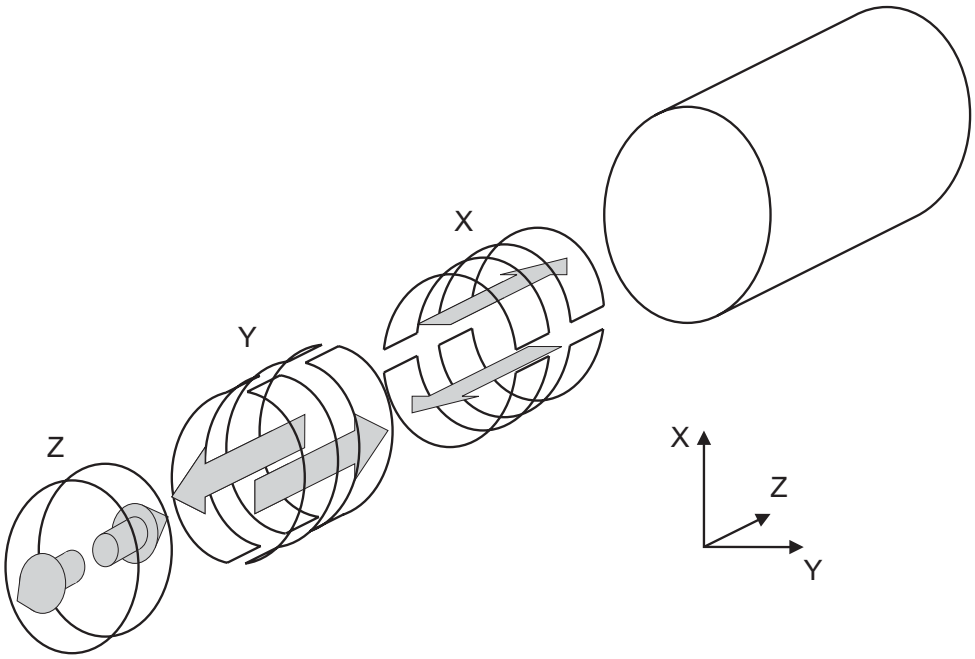

Figure 2.5: A schematic representation of an MR scanner with the separate gradient coils. Grey arrows depict the extra magnetic fields that are produced by the specific coil.

A common choice in inner diameter of the scanner bore, requested by patient comfort, is 60 cm for state-of-the-art scanners. Between the patient and the dewar is the outer casing of the scanner, the RF body coil (send and receive), the gradient coil array, and the temperature shields. Within the bore, space is expensive: the cost of an MR system is roughly 1 million US$ per tesla. Moreover, increasing the diameter makes the price go up with the fifth power of diameter. 5 centimeters more diameter makes the price go up by approximately 50 %.

RF coils can either be incorporated in the MR scanner, like body coils, or be dedicated coils, like head coils, knee coils, or any other surface coil. The send coils must be able to produce a (near) uniform field over the imaging volume. Signals received in the RF coil are passed on to acquisition and control devices for analysis and reconstruction.

The room in which the scanner is located needs to shield the surroundings from stray magnetic fields, but also shield the scanner from sources that might affect the field homogeneity. Stray magnetic fields outside the scanner room can unintentionally affect computers, credit cards, and other magnetic materials; a potential health risk occurs when people with pacemakers pass through the magnetic field. Shielding by surrounding the magnet with iron plates or active shielding helps to keep stray

magnetic field strengths within accepted risk levels. Furthermore, the RF coil is a transmitter that can influence other radio signals. Vice versa, the MR signals are weak and easily influenced by radio signals from outside the scanner room. Scanner room walls are therefore covered with a copper plates, comprising a Faraday cage.

Chapter 3

Theory

3.1 Lorentz forces acting on gradient coils

The gradient magnetic fields are generated by electric currents carried by the gradient coils. These gradient coils are positioned within the main magnetic field. Electric currents I within a magnetic field experience a force (figure 3.1), the so-called Lorentz force:

$$\vec{F_L} = \int_{\ell} I \mathrm{d}\vec{\ell} \times \vec{B}, \tag{3.1}$$

where $\mathrm{d}\vec{\ell}$ is a wire element inside the magnetic field $\vec{B}$. The resultant force on the gradient coil structure deflects the structure (figure 3.2). With an alternating current, the varying Lorentz forces induce vibrations in the gradient coil structure. These vibrations are transferred to the rest of the scanner and the surroundings. Airborne vibrations are the acoustic noise under investigation in this thesis.

3.2 Sound

Sound is the part of the acoustic radiation spectrum that can be perceived. Acoustic waves propagate through a compressible medium. In air, this implies a variation of the pressure. The auditory system is capable of detecting these variations between 20 Hz and 20 kHz. When the acoustic pressure becomes too high, the auditory system may be damaged. Health regulations prescribe the permissible sound pressure levels (SPLs) (*e.g.*, 29 CFR 1910.95, Occupational Noise Exposure). For plane waves, this acoustic pressure p is a function of the specific acoustic impedance Z_s, and the associated particle velocity u:

$$p = Z_s u. \tag{3.2}$$

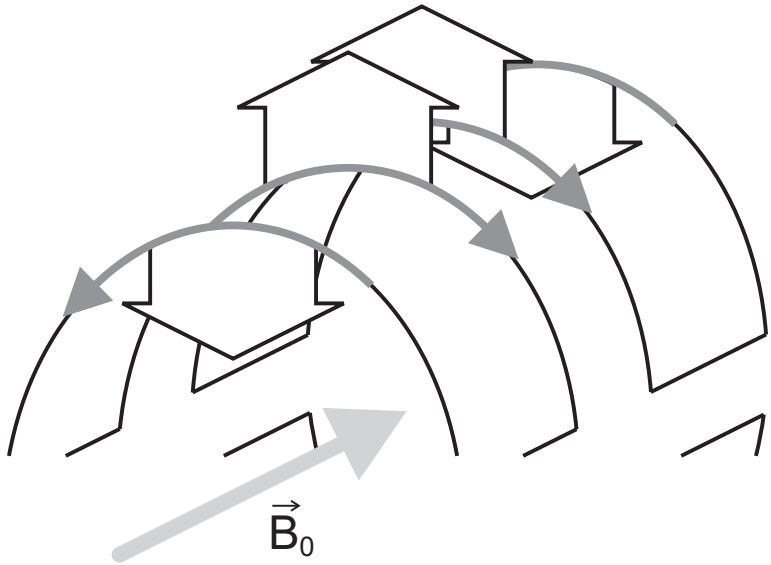

Figure 3.1: Part of the X-gradient coil from figure 2.5, with the electric currents generating the gradient magnetic fields depicted in grey. The broad white arrows depict the resultant Lorentz forces acting on the gradient coils.

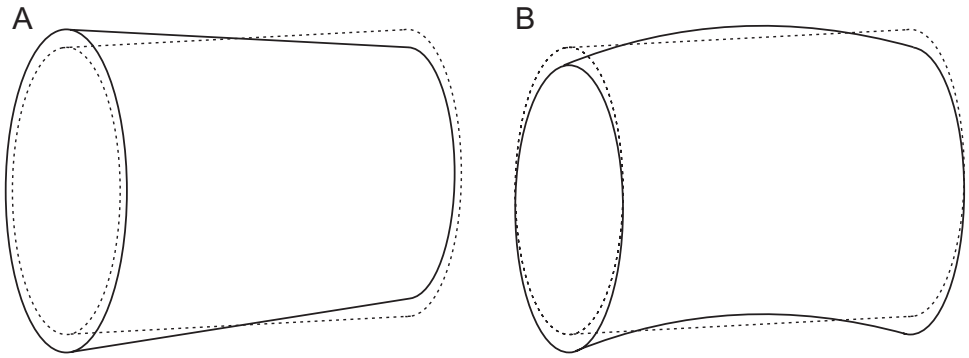

Figure 3.2: Two of the vibrational modes in which the gradient structure can vibrate, the rest position is dotted. A: The cone-shape mode due to the Z-gradient vibrations, and B: the banana-shape mode due to X- or Y-gradient coil vibrations (X-gradient coil in this case, with a deflection due to a force distribution as in figure 3.1).

Sound pressure levels are stated in decibels (dB), that is

$$\mathrm{SPL} = 20 \log_{10} \frac{p_{\mathrm{rms}}}{p_{\mathrm{ref}}}, \tag{3.3}$$

where p_{ref} is 2.10^{-5} Pa, and p_{rms} is the root-mean-square (rms) pressure variation of the air (ANSI S1.13-1995 [R1999]; Kinsler *et al.* [2000]).

The vibration distribution over an MRI scanner is complex, and for that reason the sound pressure levels vary over locations within the scanner bore and inside the scanner room. Measuring the acoustic radiation of these vibrations at the location of the head of a subject is supposed to give a good indication of what subjects will endure during scanning.

3.3 Transfer function

The transfer function $H(\omega)$ of a system is defined as the ratio of the output spectrum $R(\omega)$ and the input spectrum $S(\omega)$,

$$H(\omega) = \frac{R(\omega)}{S(\omega)}. \tag{3.4}$$

$H(\omega)$ is a complex function of ω, which can be separated in a gain part (the modulus),

$$A(\omega) = |H(\omega)|, \tag{3.5}$$

and a phase part (the argument),

$$\phi(\omega) = \arg(H(\omega)). \tag{3.6}$$

$H(\omega)$ can either be measured directly in the frequency domain through acquisition of $R(\omega)$ and $S(\omega)$ at the ω values of interest, by Fourier transform of the (im)pulse response in the time domain, or by indirect measurement of the response to broadband noise. The latter two methods assume a linear system, and miss nonlinear effects. Nonlinear components in the response do contribute to the rms measurements.

3.4 Harmonic distortion

To obtain the transfer, the ratio of response and stimulus spectra suffices if the transmission is linear. Due to nonlinearities in systems, harmonic distortion occurs, thereby introducing frequencies in the output signal which are not present in the input signal. These additional frequencies are easily shown with a Fourier transform, but they are not considered in the evaluation of the transfer function.

The ratio of the power contribution of these harmonics and the power of the fundamental frequency, is called the total harmonic distortion (THD):

$$\text{THD} = 20\log_{10}\frac{\sqrt{\sum_{n=2}^{N} a_n^2}}{a_1}, \tag{3.7}$$

where a_1 and a_n are the amplitudes of the fundamental and the nth harmonic, respectively. The power of signals is related to the square of the amplitude of sinusoidal signals.

During measurement of the response, not only the response due to the input signal is measured, but also the noise. Especially at low signal-to-noise ratios, the noise may contribute significantly to the measured signal. The number to represent all contributions to the response, which are not at the fundamental frequency, is the total harmonic distortion plus noise (THD + N):

$$\text{THD+N} = 20\log_{10}\frac{\sqrt{\text{TP} - a_1^2}}{a_1}, \tag{3.8}$$

where TP is the total power in the response.

3.5 Sound pressure transfer function

The sound pressure level (SPL) is based on the root-mean-square of the sound pressure. Time-averaging the sound pressure does not discriminate between frequencies like the Fourier transform, but integrates over frequencies. These frequencies may be the overtones caused by harmonic distortion, which should be taken into account when evaluating the transfer function, and also the noise in the signal. Sound pressure levels are calculated with this time-average of the sound pressure p_{rms} (equation 3.3); for the determination of the transfer function, this p_{rms} should be related to the rms value of the input signal:

$$H'(\omega) = A'(\omega) = \frac{p_{\text{rms}}\big(I(\omega)\big)}{I_{\text{rms}}(\omega)} \tag{3.9}$$

where $p_{\text{rms}}\big(I(\omega)\big)$ is the rms value of the sound pressure due to the gradient current of a single frequency ω, and $I_{\text{rms}}(\omega)$ is the rms value of that same current. In decibels, it is stated as

$$L_A = \text{SPL}\big(I(\omega)\big) - 20\log_{10} I_{\text{rms}}(\omega). \tag{3.10}$$

Figure 3.3 shows an example where a single frequency signal gives a response that contains the same frequency and some of its harmonics. Evaluating the transfer as

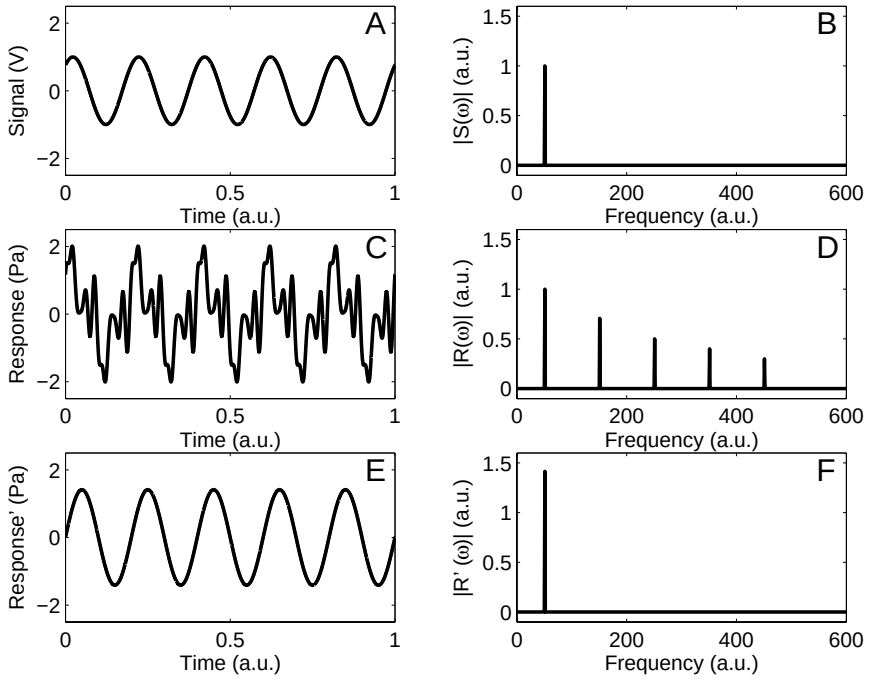

Figure 3.3: Sound pressure transfer. A: A single frequency input signal has an amplitude spectrum as in B. The response to such a signal may be distorted and produce a sound as in C (harmonic distortion of 0 dB), with an amplitude spectrum as in D. The transfer at the input signal frequency is 1 Pa/V, while the total sound pressure in this case is 3 dB higher. E: The sound pressure transfer function sums all harmonic distortion and projects that onto the input frequency: the Response' signal amplitude is 1.4 times higher to give a 3 dB higher transfer.

in section 3.3, would lead to a transfer of 1 Pa/V. However, the harmonic distortion of 0 dB (*viz.*, as much energy in the harmonics as in the fundamental) contributes significantly to the sound pressure of the response (figure 3.3C). Neglecting this contribution leads to a transfer function that cannot predict the sound nor the sound pressure accurately. The sound pressure transfer function is capable of predicting the sound pressure level as it also takes harmonic distortion into account. With an input signal containing more frequencies, all responses can be superposed. Phase information is not relevant, as by calculating the sound pressure (which is time averaging), phase information is lost.

If the input signal is a frequency modulated signal as described in section 3.6, then the transfer function can be determined with consecutive rms values of output and input signal. From the time signal it is known which frequency was presented to the system; with this information the frequency response can be determined.

In this method, the frequency resolution of the transfer function of the system is determined by the sweep rate and the time over which the rms values are calculated. One of the standard intervals for SPL calculations is 125 ms which is used throughout this thesis.

3.6 Frequency sweep response

To retrieve the transfer information for all frequencies of interest separately, a linear frequency sweep can be used. The instantaneous frequency ω of a linear frequency sweep is determined by the starting frequency ω_0 (rad/s), the sweep rate β (rad/s^2), and the time t (s):

$$\omega(t) = \omega_0 + 2\beta t. \tag{3.11}$$

The input signal $s(t)$ is then described by

$$s(t) = A\cos((\omega_0 + \beta t)t), \tag{3.12}$$

and the response $r(t)$ for a linear system (no distortion or noise) by

$$r(t) = A_r(\omega)\cos((\omega_0 + \beta t)t + \varphi(\omega)), \tag{3.13}$$

with φ_ω the frequency dependant phase shift. In this ideal case, the gain and phase part of the transfer function would be described by

$$\text{gain}(\omega) \quad = \tfrac{A_r(\omega)}{A} \quad = |H(\omega)| \tag{3.14}$$

$$\text{phase}(\omega) \quad = \varphi(\omega) \quad = \arctan\frac{\text{Im}(H(\omega))}{\text{Re}(H(\omega))}, \tag{3.15}$$

where the transfer function $H(\omega)$ is given by equation 3.4. Linearity assumes that $A_r(\omega)$ is always proportional to the stimulus amplitude A, independent of the magnitude of A. The analytic Fourier transform of a frequency sweep signal is given in appendix B.1, and practical Fourier analysis is described in section 4.3.1.

3.7 Digitizing signals

In order to accurately represent all frequencies in a time signal, the sample rate must be higher than twice the highest frequency ν in the time signal. This is the Nyquist frequency:

$$f_{\text{Nyquist}} \geq 2\nu. \tag{3.16}$$

If a frequency sweep is used for a fixed bandwidth, then a higher sweep rate takes less time to cover the bandwidth:

$$t = \frac{2\pi f_{\text{BW}}}{\beta}. \tag{3.17}$$

The acquisition time t must be matched with equation 3.16 and the sweep rate β.

The Discrete or Fast Fourier Transform (DFT or FFT) returns as many points in the spectrum as are available in the time domain. Less time results in a lower frequency resolution after Fourier transformation. An in advance defined frequency resolution in combination with the sample rate sets the time signal length t. The time signal length in combination with the highest frequency sets upper boundaries for the set of sweep signal parameters (ω_0, β).

3.8 Windowing

Practical Fourier analysis (see section 4.3.1) is performed on a finite part s_T within the time window T of a continuous signal $s(t)$. For a sampled signal (interval dt), this implies a limited number N of sample points, $N = T/dt$. In principle, the Fast Fourier Transform assumes that the periodic repetition of s_T with period T, gives the time signal $s(t) = \sum_{n=-\infty}^{\infty} s_T(t - nT)$. The Nyquist criterium requires that beginning and end of $s_T(t)$ connect smoothly, otherwise aliasing occurs. This smooth continuation is usually realized with the application of a proper time window $w(t)$ (Harris [1978]). Multiplicative weighting time signals is equivalent to convolving the spectrum of the time signal with the Fourier transform $W(\omega)$ of the time weighting function $w(t)$:

$$H(\omega) = \frac{R(\omega) * W(\omega)}{S(\omega) * W(\omega)} \approx \frac{R(\omega)}{S(\omega)}. \tag{3.18}$$

For stationary signals, windowing affects stimulus and response similarly and does not affect the transfer function. Nonstationary signals that vary sufficiently smoothly provide a similar result, *viz.*, that $H(\omega)$ does not depend on the window $W(\omega)$.

Thus, apart from spectral broadening as a result of the frequency sweep, the convolution with $W(\omega)$ broadens the spectral lines of the Fourier transform of the time signal. This might result in the masking of neighboring frequency peaks. By choosing the right window, both these effects should be optimized.

Chapter 4

Materials and methods

To compare the analysis of frequency modulated signals with Fourier transforms and the root-mean-square method, programmed test signals are fed directly to the gradient amplifiers of a Magnetic Resonance Imager.

4.1 Materials

All the experiments described in chapter 6 are performed on a 1.5 tesla Philips S15/ACS, located at the Magnetic Resonance Laboratories of the Eindhoven University of Technology. The gradient coils are driven by Copley Model 232M/S gradient amplifiers. Input signals to the gradient amplifiers are limited between -10 V and $+10$ V and the maximum gradient strength is 10 mT/m with a minimum gradient rise time of 1 ms. The same experiment with only one sweep rate is performed on a Philips Intera 3 tesla MRI scanner (maximum gradient strength 30 mT/m, minimum gradient rise time 200 μs), located at the BCN Neuroimaging Center in Groningen. On this scanner, the responses to pink noise and to pulses were also recorded. These data are all presented in chapter 7. For both scanners, experiments were carried out for all three gradient directions.

A LabVIEW program (National Instruments, LabVIEW 6) is custom built to feed the programmed signals to the gradient amplifier and simultaneously acquire the gradient current monitor signal (a voltage proportional to the electric gradient current) and the microphone signal (see appendix A.1). These tools were used to generate input signals to the scanner within the range from 0.1 V up to 5.0 V, or less if necessary to avoid clipping. The signal to the scanner was transmitted, and the output signal of the current monitor and the microphone signal were recorded to hard disk via a digital acquisition board (National Instruments, NI 6052E).

The microphone is a Brüel & Kjær 4190 condenser microphone, which is attached to a ZC0026 Preamplifier. This is connected to a Modular Precision Sound Analyzer

Type 2260 via a 10 m long extension cable (AO0442). Microphone and preamplifier are located in the iso-center of the scanner.

As no RF signals are used for these measurements, a phantom was not needed, and the head coil was removed from the scanner. Although during the measurements no phantom or head were present in the scanner which would influence the sound field, recording the sound pressure level at the scanner's isocenter is believed to give a good indication of the SPLs that patients will be subjected to.

During analysis, sound pressure levels were calculated from the microphone signal. A control experiment has been performed which showed that the calculations were within 0.1 dB of the Sound Analyzer readings.

All analog signals are low-pass filtered (KEMO, 8-pole Bessel, cut-off frequency 14 kHz) before feeding the signals to the scanner, or before acquisition.

4.2 Signals

4.2.1 Signals at 1.5 T

Input signals are programmed in MATLAB (The MathWorks Inc., version 6) and stored as 16-bit integer files. These files contain frequency modulated signals with bandwidths between 80 and 2200 Hz, depending on the sweep rate. All signals are sampled at 51.2 kHz. The lengths of the input signals are kept constant at 25 s. To avoid onset effects, all signals had a 5 s fade-in. The frequency modulated signals have a constant frequency during the fade-in; after the fade-in the amplitude is kept constant while the frequency is increasing. At the end of the signal, the frequency is also kept constant while the amplitude is decreasing in order to avoid offset effects (see figure 4.1). During the period of constant amplitude, the sweep rate is set between 10 and 16384 Hz/s. For the sweep rates of 10, 20, 50, 100, and 140 Hz/s this period is 15 s, for the sweep rates between 256 and 16384 Hz/s this period is 16 s. At low sweep rates several blocks are required to cover the sweep range. For the sweep rates above 256 Hz/s, the time is too long in combination with the sweep rate. In these cases, after reaching the upper frequency limit (in all these cases 2128 Hz) the frequency is decreased again with the same sweep rate, down to the lower frequency limit in these signals (80 Hz). This is repeated until the 16 seconds have passed.

4.2.2 Signals at 3 T

For the experiment performed on the 3 T scanner, only the sweep rate of 20 Hz/s is used. The bandwidth varied from 40 Hz to 3340 Hz. All other conditions are as described in section 4.2.1.

To measure the noise response of the 3 T scanner, a noise signal was fed also directly to the gradient amplifiers. This pink noise with a bandwidth from 40

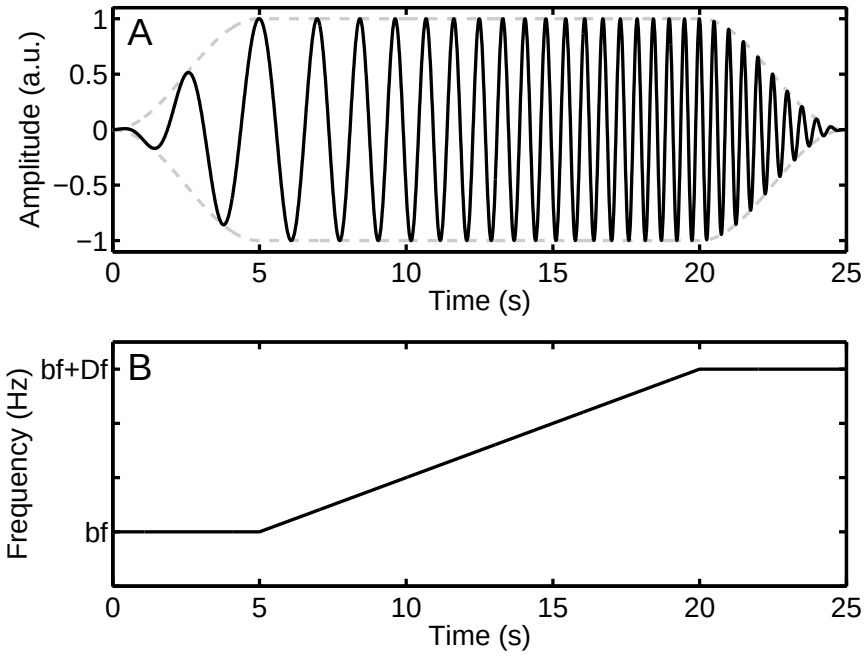

Figure 4.1: Frequency sweep time signals $s(t)$. Panel A: amplitude course of the frequency sweep time signals (solid line) with its envelope (dashed curve); first 5 seconds fade-in with constant frequency bf, next 15 seconds constant amplitude with increasing frequency, last 5 seconds fade-out with constant frequency which is Df Hz higher than the begin frequency (= bf + Df Hz). Panel B: frequency course as described under Panel A.

to 3500 Hz was generated with a noise generator (Dynamic Signal Analyzer HP 35670A). The rms amplitude of this signal was 0.2 V.

The unidirectional pulses were programmed on the scanner's pulse programming environment. No external control signal was used for this experiment. The pulses had a 0.2 ms rise time to half of the maximal gradient current; after 0.2 ms of constant current, the gradient current dropped to zero in 0.2 ms. This trapezoidal pulse has a total duration of 0.6 ms; the width of the trapezoid at half the maximum height is 0.4 ms, this width will be denoted full-width half-maximum. The repetition time of the pulses was 4 s.

4.3 Methods

Transfer functions were derived for all sweep rates and all amplitudes, as well as for the noise response and the pulse response. Comparisons have been made between amplitudes and between sweep rates. Responses to the frequency modulated

stimulus signals were analyzed with Fourier analysis and rms analysis.

4.3.1 Fourier analysis

The analysis of the data with Fourier transforms for the low sweep rates ($\leq$ 140 Hz/s) is performed to give a constant frequency resolution. A Kaiser-Bessel window ($\beta = 10$)[1] of two seconds wide was multiplied with both the current monitor signal and the sound pressure signal. The choice for a Kaiser-Bessel window was made for the good trade-off between main lobe width and side lobe level (Harris [1978]). The spectra corresponding to the bandwidth covered by the central 0.5 seconds are saved; this piecewise analysis is repeated after shifting the window 0.5 s, until the end of the file (see figure 4.2, panels E and F). All spectra from the separate files are combined and divided to give the transfer for the specific amplitude and sweep rate.

For the high sweep rates ($\geq$ 256 Hz/s), the window width is inversely proportional to the sweep rate. The window width is twice the time the signal needs to cover the desired bandwidth. As this bandwidth is covered multiple times with these sweep rates, the transfer functions of the different parts are averaged.

4.3.2 Root-mean-square

Alternating electric currents give alternating Lorentz forces that produce the vibrations which lead to acoustic radiation. In these experiments, the amplitude of the electric current is constant. With a flat frequency response of the MRI scanner, the vibration amplitude of the scanner's shrouds would also be constant over frequency. This, in turn, would lead to a constant air particle displacement. The local sound pressure, however, is proportional to the particle speed (equation 3.2). For sinusoidal plane waves, this particle speed depends linearly on frequency when the particle displacement amplitude is constant. In order to match the averaging window for SPL measurements, the rms of the electric current is taken over 125 ms intervals, and related to the corresponding root-mean-square value of the sound pressure.

The covered bandwidth within one 125 ms interval increases with the sweep rate. With the sweep rate of 16384 Hz/s, the complete bandwidth from 80 to 2128 Hz is covered within the 125 ms. Therefore, transfer functions are only derived with sweep rates up to 140 Hz/s. The frequency resolutions of the transfer functions with sweep rates from 10 to 140 Hz/s range from 1.25 Hz to 17.5 Hz, respectively.

[1] The Kaiser-Bessel window $w(t)$ between $-T$ and T is given by $w(t) = I_0\big(\beta\sqrt{1-\frac{t^2}{T^2}}\big)/I_0(\beta)$, with I_0 the modified Bessel function of the first kind.

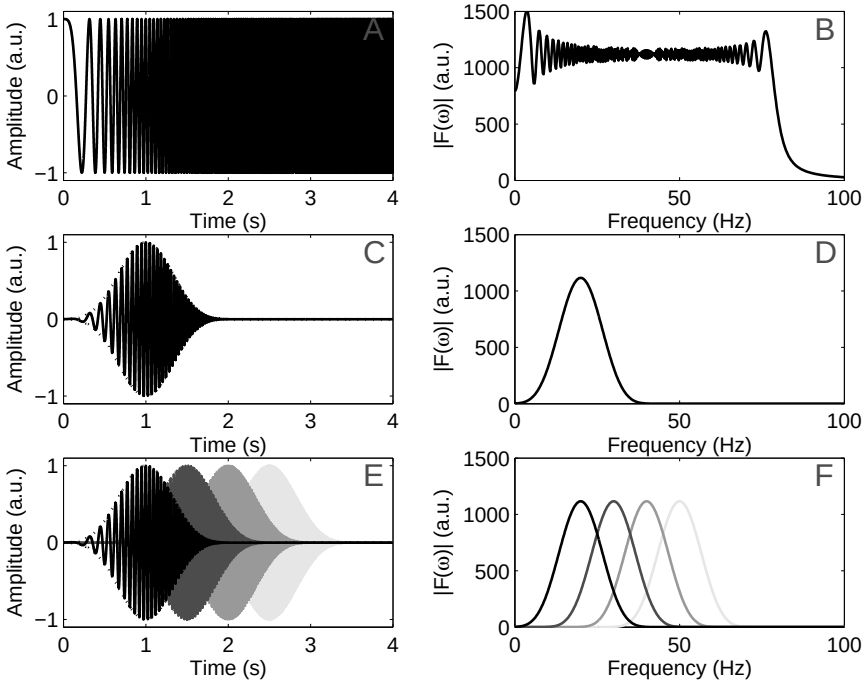

Figure 4.2: How frequency modulated time signals (left column) behave under Fourier transformation to the frequency domain (right column). Panel A: example of frequency modulated signal (0-80 Hz within 4 s); panel B: the Fourier transform of the frequency modulated signal in panel A; panel C: windowing of part of the time signal; panel D: the Fourier transform of a windowed part of panel B; panel E: stepwise taking parts of the time signal; panel F: the corresponding Fourier transforms (see section 4.3.1).

Chapter 5

Towards a more silent scanner; an analysis of sound reducing methods

5.1 Introduction

In functional Magnetic Resonance Imaging (fMRI), the demand for high spatial and temporal resolution, together with high signal-to-noise-ratio (SNR), requires Magnetic Resonance (MR) scanners with high magnetic field strengths and fast switching of strong gradients.

The effects of high static magnetic fields on humans have been investigated since the 1960s (*e.g.*, Barnothy [1964]). There is no indication that the static field of an MR scanner is of any harm with the current field strengths (< 4 T) (Schenck [2000]), except for accidents with ferromagnetic objects and pacemakers. Time-varying magnetic fields, such as switching gradient magnetic fields, may cause peripheral nerve stimulation or in extreme cases even cardiac stimulation (Schaefer *et al.* [2000]). Radio frequency (RF) pulses for selection purposes can interact with implants (Shellock *et al.* [2004]), and other foreign bodies like tattoos (Tope and Shellock [2002]). Tissue heating by RF pulses is also possible (Shellock [2000]).

The interaction between the strong electric currents carried through the gradient coils and the high magnetic field generate vibrations due to the evoked Lorentz forces acting on the gradient coils (*e.g.*, Mansfield *et al.* [1995]). Acoustic radiation originating from these induced vibrations easily reaches sound pressure levels (SPL) of 110 dB and higher (Counter *et al.* [2000]; Hedeen and Edelstein [1997]; McJury *et al.* [1994]; Moelker *et al.* [2003b]; Price *et al.* [2001]; Ravicz *et al.* [2000]). The auditory system may be damaged when exposed to these high levels (*e.g.*, 29 CFR 1910.95, Occupational Noise Exposure). Moreover, the acoustic noise is a cause

for anxiety (Quirk1989), distraction (Barrett [2002]; Elliott *et al.* [1999]; Mazard *et al.* [2002]), and spurious activation during functional brain research (Belin *et al.* [1999]; Hall *et al.* [2000]; Mathiak *et al.* [2002]; Talavage *et al.* [1999]).

Various methods are employed to reduce the sound exposure for subjects, ranging from inserting ear plugs and putting on ear muffs to redesigning the scanner. This paper addresses the technical and practical considerations in MR scanner design regarding sound generation, and discusses the various sound reducing methods, and their effectiveness.

5.2 Sound sources in the scanner room

The walls of the scanner room not only play a role in shielding electric and magnetic fields, they also fulfil a task in sound insulation. In particular, they shield the environment from the scanner noise.

Inside the scanner room, various sound sources can be distinguished (*cf.* Ravicz *et al.* [2000]). They are described in the following subsections.

5.2.1 Air-handling system

A modern air-handling system can be relatively silent. The blower inside the scanner bore gives a constant fresh air flow at the head position, but the associated sound level remains low in comparison to other sound sources.

Air-handling of the scanner room also generates a rather constant background noise. Technically it is possible to keep this noise level below 20 dB(A) (*e.g.*, Ramamoorthy *et al.* [2003]). Even at 30 dB(A), this noise is not a serious problem. Moreover, it always remains possible to switch off the system (temporarily).

5.2.2 Liquid helium pump

A pump is used to keep the helium liquid; the boiled-off helium is recycled by compression and subsequent expansion to liquify the helium again. The pump makes a pounding sound, mainly with low frequencies. SPLs reach up to 80 dB (Ravicz *et al.* [2000]). Turning the pump off results in helium boil-off; turning the pump off for a prolonged period may result in a quench: the magnetic coils loose their superconductivity due to the temperature increase; the strong currents produce heat in the resistive coils which in turn increases the boil-off rate. Turning the pump off temporarily also results in helium boil-off, this period should not be too long. Relocating the pump, or insulating it, reduces perceived SPLs.

5.2.3 Electric current leads

From our own measurements (unpublished results) we learned that loosely fastened current leads to the gradient coils may produce loud noise at the resonance frequencies of the length of wire. The alternating current through the wires interact with the static magnetic field; the evoked Lorentz forces bang the wires to the cryostat or the shields. These acoustic noise sources can be prevented by tightening the wire connections or by placing stiff current leads some distance from other objects.

5.2.4 Eddy currents

Eddy currents can be induced in the RF coils, the RF shield, and the static field magnet cryostat (Katsunuma *et al.* [2002]). Changing magnetic fields as the gradient fields in MRI, produce a changing electric field in accordance with Maxwell's laws. Lenz's law states that a changing magnetic field induces an opposing magnetic field in a conductor. For this reason, the electric gradient currents have an overshoot in the beginning of a pulse to compensate for this effect. The induced eddy currents are time-variant and the resultant Lorentz forces make the conductor vibrate. The RF coils are located near to a person's ear, so the vibrations there may be a major sound source. Likewise, eddy currents in the RF shield and the magnet cryostat cause these structures to vibrate with resultant acoustic noise.

5.2.5 Gradient coil noise

The strong electric currents flowing through the gradient coils interact with the static magnetic field. The resultant Lorentz forces are distributed over the gradient coils and try to deflect the gradient coil structure. Actual vibration patterns depend on the force distribution, material properties, frequencies of excitation, and gradient coil dimensions. These vibrations may match eigenfrequencies of the gradient coil assembly resulting in strong vibrations and high sound pressure levels (Tomasi and Ernst [2003]).

5.3 Effects of acoustic noise

In general, continuous exposure to sound with high sound pressure levels has physiologic and psychologic effects. This is also true during MR imaging.

5.3.1 Hearing threshold shift

Exposure to sound pressure levels above 80 dB(A) are considered dangerous. Hearing damage due to acoustic noise cannot be cured, and even a onetime exposure

to high sound pressure levels (disco, drill, or other noisy environments) can permanently damage the auditory system. The seriousness of damage due to acoustic noise depends on levels and exposure time. Standards, like the Occupational Noise Exposure (29 CFR 1910.95 (R1999)), prescribe a hearing conservation program when workers are subjected to a time-weighted average of 85 dB (measured on the A-scale, slow response) over an 8-hour working day. Permissable noise exposures start from 8 hours at 90 dB(A) (slow response), and are reduced by a factor of 2 for every 5 dB increment of the time-weighted averaged noise, or their combined effect for different levels. All continuous, intermittent, and impulsive sounds with levels from 80 to 130 dB are taken into account for these measurements. Exposure to impulsive or impact noise should not exceed 140 dB peak sound pressure level. Hearing protectors, as mufflers and earplugs, should attenuate the noise to the permissible noise exposure.

When the ear is exposed to high sound pressure levels, muscles in the middle ear can tighten. Through this so-called Stapedius reflex, the transfer of the middle ear can be reduced by about a factor of 6 in amplitude, giving some protection to overload. As the muscles do not relax immediately, a temporary threshold shift occurs (Brummett *et al.* [1988]) which can last from several minutes to hours, depending on exposure time and level (Elliott and Fraser [1970]).

Still, if noise reduction measures are not sufficient to reduce the exposure to noise below safety levels, permanent threshold shifts may occur.

5.3.2 Discomfort and anxiety

The loud acoustic noise can also cause discomfort or even anxiety. Being inside a relatively narrow bore can cause claustrophobia or panic attacks. Discomfort can come from the examination duration or the temperature inside the scanner bore (Brennan *et al.* [1988]; Quirk *et al.* [1989a]). People undergoing MR examination should be provided information on the MR scanner's (noninvasive) imaging techniques, the small bore that can evoke feelings of confinement, the possible rise in temperature, the acoustic noise, the duration of the examination, and the possible outcomes of the examination (Quirk *et al.* [1989b]; Harris *et al.* [2004]). It is good to note that people with a more anxious nature, are more likely to experience anxiety during MR scanning.

While not all feelings of discomfort and anxiety can be taken away, efforts can be made to prevent these feelings. The used techniques can be explained properly, perhaps some time prior to examination. The outcomes of the examination cannot be changed, and the duration of the scanning has a lower limit. A constant stream of fresh air can provide a pleasant ambient temperature. The feelings of confinement can partly be taken away in open scanner systems, or by (optically) shortening the scanner bore (DeMeester *et al.* [2002]). Finally, efforts can be taken to reduce the acoustic noise accompanying MR imaging.

5.3.3 Confounding stimulus

The acoustic noise does not only have aforementioned effects. During functional brain research, the noise itself is a stimulus with an adverse effect on the outcome of the research.

Interference between task and noise

Brain activation in the auditory cortices as a result of the scanner noise is straightforward (Hall *et al.* [2000]; Mathiak *et al.* [2002]; Schmithorst and Holland [2004]; Shah *et al.* [2000]; Talavage *et al.* [1999]; Tanaka *et al.* [2000]). The loud noise immediately hampers functional brain research of the auditory system (Ulmer *et al.* [1998]). No discrimination can be made between stimulus and noise, unless the noise is not present during the stimulus (Belin *et al.* [1999]; Di Salle *et al.* [2001]; Hall *et al.* [1999]; Schmithorst and Holland [2004]), or the stimulus is the scanner sound itself (Bandettini *et al.* [1998]; Bilecen *et al.* [1998]).

Distraction from task

"It's so noisy, you can't think straight" (Barrett [2002]). For simple tasks, the visual and motor tasks were not hampered significantly due to the scanner noise, where passive listening resulted in less auditory cortex activation (Elliott *et al.* [1999]). In a study that required more attention, the motor areas showed an increase in activation under a motor task, and the visual areas showed a decrease in activation under a visual task (Cho *et al.* [1998a]). A Positron Emission Tomography study by Mazard *et al.* [2002] showed that tasks became harder when recorded scanner sound was presented. All this does not necessarily imply that fMRI is not suitable for functional brain research, but these effects must be considered when interpreting data.

Background activation increase

The scanner noise gives a continuous activation of the auditory cortices. Effectively, this elevates the baseline of activation in auditory experiments. Differences between activation due to the target stimulus and the baseline decrease, which leads to a lower activation estimate (Bandettini *et al.* [1998]; Di Salle *et al.* [2003]; Elliott *et al.* [1999]; Hall *et al.* [1999]).

5.4 Sound reducing methods

In this section, we give a thematic overview on noise reducing methods in fMRI. Some published papers treat several of these subjects in one study and connect the different topics. A complete separation is therefore not always possible. Whenever necessary, we comment on the methods and the obtained results.

5.4.1 Passive methods

Under passive sound reducing methods, we understand every physical measure to attenuate the acoustic noise that does not use electronic components or transducers.

Mufflers and earplugs

When vibrations become airborne, the acoustic noise can only be attenuated at the level of the ear. In general, if permissible exposure levels are exceeded, then hearing protection devices (HPD) are mandatory. The HPD should bring the perceived noise levels under the level that is permitted (29 CFR 1910.95 (R1999)).

Conventional HPDs are low-pass filters, attenuation up to 2 kHz can be as much as 30 dB for earplugs. Above 2 kHz, attenuation can increase to 40 dB. Factors of importance are used materials and how well the ear canal is occluded by the inserts (Casali and Berger [1996]). Circumaural HPDs have about the same frequency characteristics, with a somewhat lower attenuation (Berger *et al.* [1998]). If earplugs are not properly inserted, or the pinnae are not properly covered, then attenuation is not maximal. The combination of earplugs and mufflers give a combined effect, insofar the threshold of bone conduction is not surpassed (Berger and Kerivan [1983]). Custom made HPDs perform better than standard devices, but feasibility of this is low for patients who come for a one-time only examination. However, for health workers whose daily work is in the MR room, personal fit HPDs are recommended.

Further increase of attenuation can be achieved by placing a helmet over a person's head to prevent acoustic noise from reaching the cochlea via bone conduction (Berger *et al.* [2003]; Ravicz and Melcher [2001]). Apart from the discomfort caused by the helmet, it takes extra space which in general is not available in a headcoil.

All these measures reduce all incident sound, regardless of being noise or instructions/stimulus. Placing headphones to the pinnae, and have earplugs inserted with a known frequency characteristic and compensate for that, can solve this problem. Another solution is having inserts that block the ear canal from noise, but with a sound guide coming from a loudspeaker. What should be kept in mind is that communication with the person in the scanner should be possible at all times (Moelker *et al.* [2004]).

What also should be realized is that the given values are maximal values. Non-proper insertion of earplugs leads to a decreased attenuation. The conduction of vibrations via the bed to the skull to the cochlea is not considered. A psychophysical evaluation of this transfer should be conducted, or at least, with an artificial head. The reported sound pressure increase with a person in the bore (Hedeen and Edelstein [1997]; Price *et al.* [2001]) needs to be investigated further as well.

Transmission pathway blocking

To prevent the vibrations of internal structures to become airborne, the transmission should be blocked. Acoustic noise reaches the subject in the scanner via different pathways, with all different contributions to the perceived sound pressure levels (Katsunuma *et al.* [2002]; Moelker *et al.* [2003a]). The same is true for a health worker near the scanner. To effectively block the acoustic transmission, the different pathways have to be discerned.

The vibrations of the gradient coils are transmitted towards the bore, and the shrouds in the bore transfer the vibrations to the air. In the other direction, the vibrations of the gradient coils are transmitted via the gradient supports to the cryostat, and via the cryostat to the outer shrouds and to the building. Indirect sound coming from reflections and vibrations of the walls contribute little to the sound pressure in the bore, but have a significant contribution to the sound pressure at a health workers location (Moelker *et al.* [2003a]). Blocking the vibrational pathway from the gradient coils by placing them in a vacuum, reveal other sound sources as eddy current induced vibrations in the cryostat (Edelstein *et al.* [2002]; Katsunuma *et al.* [2002]). Placing polyurethane liners in the acoustic pathway is the most straightforward application of passive acoustic screening (Foster *et al.* [2000]; Mechefske *et al.* [2002a]; Moelker *et al.* [2003a]).

In the bore, the highest contribution comes from the direct path of the vibrating gradient coils (Katsunuma *et al.* [2002]). Most of the work on acoustic liners is done within the bore. Liner materials are known to attenuate more at high frequencies. Foster *et al.* [2000] give only one number without frequency selectivity, namely 10 dB for foam placed between the gradient coils and the shim coils. Mechefske *et al.* [2002a] placed a fiberglass cylinder (inner diameter 62 cm, covered on the outside with a noise barrier) within the bore. This cylinder was mechanically decoupled from the MR system. Measured at the iso-center this setup provides a 10 or 17 dB SPL reduction for two different liners at 1000 Hz. Closing an open side of the scanner with an end-cap reduces the SPL with another 9 or 4 dB, respectively. The same values are found for a realistic EPI sequence. Moelker *et al.* [2003a] covered all surfaces in the scanner room with 7.5 cm thick layers of fiberglass. The results show that covering the outer shrouds and the walls does not significantly reduce the sound pressure levels in the bore for any frequency. Outside the bore, however, covering the combined surfaces lead to a 10–20 dB reduction for frequencies above 500 Hz. The separate coverage of surfaces does not give major results, suggesting that acoustic shielding should be done carefully in order to prevent sound leakage. Attenuation of the sound pressure in the bore can be as high as 29 dB (at 10 kHz), but driving the scanner with real sequences only shows 10–12 dB reduction. Having to trade 15 cm inner bore diameter for this reduction is not an option.

Placing the gradient coils inside a vacuum, and mechanically decouple it from the rest of the scanner, results in a decrease of transfer of up to 24 dB (Edelstein

et al. [2002]; Katsunuma *et al.* [2002]). This depends on the pressure in the vacuum enclosing. Both articles show a dependence on pressure that is conform the theoretical expectations for 2 sources, where the loudest decreases in contribution and the previously softer source becomes the dominant source. The maximal attenuation depends not only on the pressure, but also on the mechanical coupling between the vibrating gradient coil and for instance the cryostat. Mounting the gradient coils independently on the concrete floor leads to better attenuation than mounting the gradient coils on the magnet bore. Only 6-8 dB attenuation is reported for the latter setup.

Eddy current prevention

Vibrations can be caused by eddy currents interacting with the main magnetic field. These eddy currents come from the gradient fields intersecting a conductor, *e.g.*, the cryostat. The changing magnetic field causes a current that creates an opposing magnetic field, according to Lenz's law. Without prevention of eddy currents, the opposing field has to be compensated for by stronger gradient fields. Not only regarding vibrations, but for gradient magnetic field linearity, eddy currents should be prevented to avoid image degradation.

After blocking the vibrations from the gradient coils, the eddy current induced vibrations become the main source of vibrations. Edelstein *et al.* [2002] list the order in which the different conductors contribute to the sound pressure in the scanner bore:

1. Eddy current induced vibrations of the conducting cryostat inner bore.
2. Eddy current induced vibrations of the RF coil (body coil or head coil).
3. Eddy current induced vibrations of the cryostat that are mechanically transmitted to the patient bore.
4. Remaining vibrations of unknown source-pathways that are radiating sound to the patient bore.

The general approach to reduce eddy current-induced vibrations is by shielding. Eddy currents have typical dimensions and orientations. By changing the dimensions and/or orientation of the conductors, the eddy currents die out faster. Consequently, they have less influence. Producing a nonconducting cryostat inner bore takes care of eddy currents in that part of the scanner (Edelstein *et al.* [2002]; Katsunuma *et al.* [2002]).

Gradient coil design and modeling

Gradient coils are designed to produce adequate gradient magnetic fields. Secondly, gradient coils are designed to dampen the vibrations of the coil assembly and the

induced acoustic noise. The development of a model regarding the vibrations and acoustics of an MRI scanner starts with the choice of the modeling method (Kuijpers [1999]). By choosing a deterministic approach, the choice between analytic and an element method is the next choice to be made. The analytic approach can be used to look at the acoustics of a vibrating duct (Kuijpers [1999]), or a plate (Mansfield *et al.* [1998]), for an increase in insight. With this knowledge, finite element methods can be developed to numerically analyze the vibrations and sound of the MR scanner.

With increasing computational power, it is feasible to employ computer modeling of an MR scanner. Dedicated toolboxes or software, make it possible to compute the Lorentz force distribution over the gradient coil, the vibrational modes of a gradient coil, the shape of the (gradient) magnetic fields, and the acoustics concerned with the gradient coil vibrations. Without modeling, expensive ($\sim$ 100,000 US$) gradient coils have to be built to test its properties. Finite element analysis (FEA) has proven to be a powerful tool in different research areas, including construction. The material properties of all elements (density, Young's modulus, damping) can be adjusted, as well as their mutual interaction.

Proper arrangement of conductors produces a linear gradient magnetic field when currents are send through the coils. The exact arrangement is important for the produced magnetic fields as well as for the Lorentz force distribution. In MR sequences, the electric currents and the wire length are well known beforehand. This distribution can be calculated with equation 3.1 (Yao *et al.* [2004]). Applying the calculated (dynamic) forces to the mesh, enables to model the deflection/vibration pattern of the gradient coil assembly (Edelstein *et al.* [2002]; Mechefske *et al.* [2002b]).

In modeling, assumptions must be made. The general assumptions comprise the necessary mesh dimensions, the boundary conditions, and material parameters. The mesh dimensions must be smaller than the produced wavelengths λ ($\lambda = c/f$, where c is the velocity of sound in air, and f is the frequency of excitation). The wavelengths of airborne sound are the lowest, as the velocity of sound in solids is much higher than in air. For accurate simulation result, appropriate mesh sizes are oversampling the acoustic wavelength (Edelstein *et al.* [2002]; Mechefske *et al.* [2002c]). In this assumption, there is no room for produced overtones with consequently shorter wavelengths. The boundary conditions are the forces acting on the gradient coil, and the suspension to the rest of the scanner. The vibrations of the rest of the scanner, when this starts to vibrate as well, make it computationally harder to predict the vibrations of the gradient coil. Taking the suspension fixed is besides reality but might approximate it. Experimental evaluation is therefore necessary (Mechefske *et al.* [2002c]; Yao *et al.* [2004]).

As a gradient coil consists of several elements: the wiring for the separate gradients, the tubing for the cooling, and the resin that holds everything together, it is not feasible to model every detail. Moreover, these details are much smaller than the mesh size. Modeling several layers (wiring, resin) with appropriate parameters pre-

dicts the vibrations in a real gradient coil well. With this vibration data, the sound field and the sound pressure can be computed (Edelstein *et al.* [2002]; Yao *et al.* [2004]).

The prevention of eddy currents is also investigated by numerical methods. This shielding is about the confinement of (gradient) magnetic fields, which is especially challenging in shorter magnets (Brown *et al.* [2002]; Shvartsman *et al.* [2001]). Perfect shielding is impossible, the deviation from perfect shielding, the "shielding error", should be as low as possible. Numerical methods have been developed to assist the development of better shielding when making gradient coils.

Cho *et al.* [1998b] proposed a rotating DC gradient. The switching of the read- and phase gradients produces the loudest noise during MRI scanning. Omitting these sources leaves the slice selection gradient which produces less acoustic noise. A gradient coil, with a constant gradient field perpendicular to the selected slice, is rotated with suitable angular increment. At each angle a recording is made. Images are obtained by projection-reconstruction, like in Computed Tomography (CT) scanning. A 20.7 dB reduction in acoustic output is reported without mentioning the time needed for image acquisition.

5.4.2 Active methods

Active methods to reduce the vibrations of the scanner or the acoustic noise include counterbalancing Lorentz forces, anti-noise, and active structural acoustic control.

Vibration cancellation

The surfaces that contribute most to the sound pressure within the scanner bore, are the shrouds of the bore. If these do not vibrate, and the outer housing contribution is negligible, then no acoustic noise is radiated. Piezoelectric actuators or magnetostrictive actuators can replace the shrouds, and they can be electronically controlled to vibrate with the exact amplitude and anti-phase as the shrouds would normally vibrate. In this way, the inner surface of the bore does not vibrate and consequently does not radiate acoustic noise. This has already been investigated in the aviation industry for turbo-prop aircraft cabins (Wu *et al.* [2003]; Aurilio *et al.* [2003]). Plans exist to investigate this in MRI (Moelker *et al.* [2003a]), but to our knowledge, so far, no results have been published. The magnetostrictive method does not work in MRI, as extra magnetic fields are needed for the shrinking or enlargement of the material. These extra fields influence magnetic field homogeneity. If the changing electric fields from the piezoelectric actuators also influence the magnetic field homogeneity, or otherwise distort image acquisition, then this technique will also not be feasible in MRI.

Active noise control

"Can't you use anti-sound?" is one of the most frequently asked questions by the audience concerning acoustic noise in MRI. Recording the acoustic noise and playing it back in anti-phase seems an easy and feasible solution. The general approach is to have the subject wear earphones with microphones near the ear, if possible, close to the eardrum. Noise coming from outside the headset is measured by the microphones and send to a Digital Signal Processing unit. An adaptive filter produces the anti-noise signal that is presented to the ear via the earphones. Through constant adaptation, the noise at the ear drum should be kept as low as possible (Casali and Berger [1996]). The damping effect of this method is limited to about 40 dB. After cancellation of all sound in the ear canal, the sound that reaches the cochlea is dominated by bone conduction. To obtain a 40 dB reduction for pure sinusoids, the amplitudes of the sound and the anti-sound must not differ more than 1 % with perfect phase matching. With perfect amplitude matching, the phases need an accuracy of 0.01 radians, or 0.6 degrees (Chambers *et al.* [2001], see also appendix B.2). Inside the scanner, sub-millimeter displacements are typical for subjects. Such displacements can destroy the phase matching if it is not compensated for displacements accurately. Health workers near the scanner are moving more, and faster. Depending on the speed of the DSP and the accuracy of the feedback system, the efficacy of anti-noise for health workers is limited to low frequencies. The combination of active noise reduction with passive hearing protection, which is limited to higher frequencies, can give a 20 dB reduction above 125 Hz (Casali and Berger [1996]).

McJury *et al.* [1997] recorded MR scanner noise and replayed the sound in an audio laboratory via loudspeakers. A reference microphone, connected to a DSP unit, controls a secondary source to emit the anti-noise. An error microphone in the desired zone of quiet is also connected to the DSP to optimize the anti-noise. Results in this test were satisfying below 350 Hz, with an average reduction of 10–15 dB up to 30 dB for single frequencies.

Chambers *et al.* [2001] performed three anti-sound experiments. The first was, in a standard setup, reducing white noise and pure-tone target detection in a sound-laboratory. The second experiment used recorded scanner sound in a feed forward fashion, and was conducted within a replica scanner. Using an error reference microphone too close to the ear, gives too little time to the DSP to generate the anti-sound. Subjects were asked to report the subjective reduction in SPL. For two different EPI recordings at fundamental frequencies of 600 and 1900 Hz, the subjective attenuations were 12 and 5 dB on average, respectively. Further, filtered noise experiments (to simulate scanner noise) were conducted in the replica scanner to obtain difference spectra at 8 frequencies between 500 and 3000 Hz. At these frequencies, the attenuation was approximately 40 dB. The third experiment was conducted in a real scanner with two EPI sequences (fundamental frequencies 750 and 1500 Hz), to

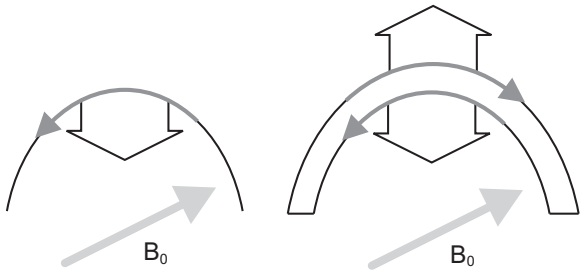

Figure 5.1: Arcuate coils experience a Lorentz force inside the magnetic field. Placing a return arc, embedded in one piece of material with the standard arc, leads to cancellation of the Lorentz forces.

find 40 dB attenuation at the fundamental frequency. No subjective data have been reported. The fundamental frequency of an EPI sequence is most prominent, and therefore most easily be detected and possibly attenuated most. The published spectra show that the rest of the spectrum is hardly affected. The removal of the most prominent peak reduces the total sound pressure to the integral of the rest of the pressure spectrum. This leads to about 20 dB reduction in total SPL. This makes it still worthwhile to use active noise control during MRI.

Lorentz force balancing

Sir Peter Mansfield and coworkers have been active in tackling the vibration problem at the source: the Lorentz forces acting on the gradient coils. Closed arc loops are fabricated in which the Lorentz forces acting on the separate wire segments are opposite, and therefore cancel. The arcs are casted in polystyrene resin mould to mechanically couple the wire segments of one arc. The segments have some space between them, else the currents through the segments would also cancel the magnetic fields produced by the currents flowing through the separate arc segments. With an optimized distribution of such coils, gradient linearity can be obtained within the imaging volume (Chapman and Mansfield [1995]). However, the resin deforms under alternating forces, and radiates an acoustic wave perpendicular to the resin surface (Mansfield *et al.* [1995]). The problem of the compressive wave in the resin has been further investigated and described theoretically in succeeding articles (Mansfield and Haywood [2000]; Mansfield *et al.* [2001]). To fully understand the problem, arcuate coils are replaced by a rectangular loop, embedded in a rectangular plate of resin. When driven with an alternating current inside a magnetic field, the rectangular plate radiates sound perpendicular to the plate. With the material parameters (size, density, Young's modulus), the acoustic emission (SPL, angular distribution) can be predicted. This is also validated experimentally. To enhance the acoustic radiation, an extra loop is added in the center of two halve plates, separated by a small air gap. Driving that loop with a current of appropriate amplitude

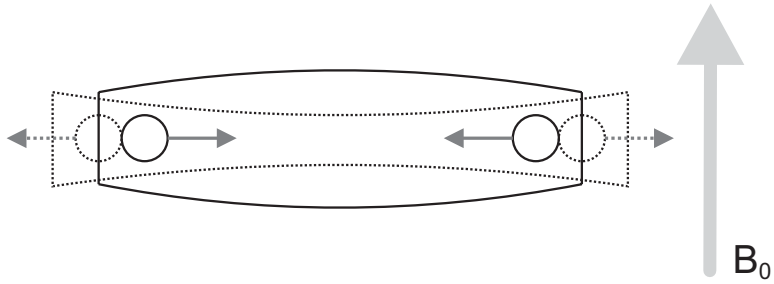

Figure 5.2: Top view of a plate containing a current loop. Lorentz forces acting on the wires causes stress. The direction of the stress causes compression (solid lines), or tension (dotted lines). With alternating forces, acoustic waves are produced, perpendicular to the plate surface.

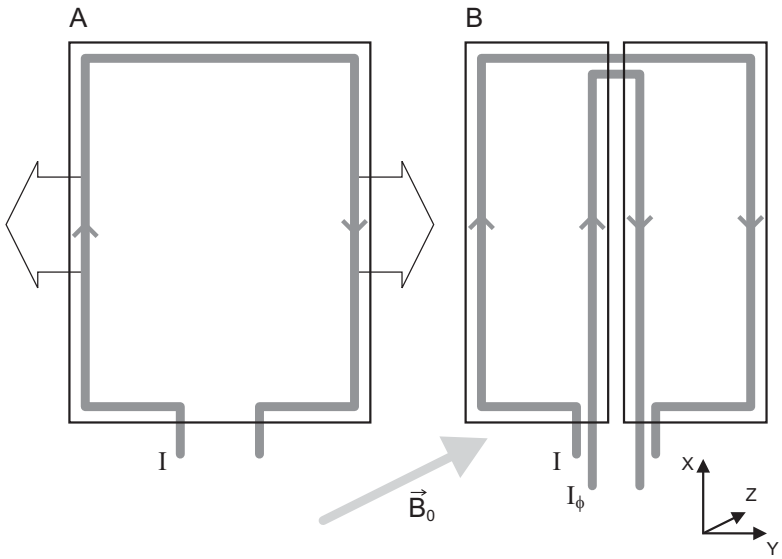

Figure 5.3: Front view of a plate containing a current loop. A: The Lorentz forces exert tension on the plate. B: The solution as proposed by Mansfield. An additional current loop, in combination with a segmented plate, prevents a compressional wave. The plate segments, however, experience a force by both wire segments in the same direction, and hence, these segments displace. The original goal of Lorentz force balancing was to prevent this displacement.

and phase-lag, the compressive wave is not building up, but more or less damped by impedance matching. The optimum phase-lag depends on the compressional wave velocity and the dimensions of the plate. Results are reported for different plate materials, which can be as high as 50 dB attenuation at specific frequencies and microphone positions. The average reduction is about 30 dB. It is shown, that with a proper placement of thus constructed coils, gradient fields can be produced.

Finally, it is shown how these coils can be used for imaging (Chapman *et al.* [2003]). The coils are driven with a sinusoidal electric current, matching the plate's compressional wave resonance frequency. Instead of just switching the currents on and off (multiplying with a tophat signal, with a sinc as Fourier transform), the currents have an envelope that is generate with the Fourier transform of a truncated sinc. This process, which is called optimized gradient pulse, gives an additional reduction in the produced SPL. A 50 dB reduction is reported. It should be noted that this is a 50 dB reduction at only the plate resonance frequency. Taking all the harmonics into account, the top hat gradient pulse does give a reduction of about 37 dB. However, the optimized gradient pulse gives a reduction of 41 dB in total SPL, instead of the reported 50 dB. When the contribution of the fundamental frequency is decreased, the influence of the harmonics cannot be neglected anymore.

It is not clear what the efficacy of Lorentz force balancing eventually is. The reduction is limited to about 10 dB at low frequencies (Mansfield *et al.* [1995]). Is this an intrinsic limit or does the compressional wave noise becomes the loudest source? No explanation is given on this topic. Further, the idea of Lorentz force balancing leans on mechanical coupling of two loop segments. The additional current loop to overcome the compressional wave problem only makes sense when there is a gap between two plate halves. In our view, the gap introduces a decoupling between the two wire segments that, for Lorentz force balancing, should be mechanically coupled. The solution to the compressional wave problem is the end of the solution to the initial problem. Without the use of active acoustic control, acoustic absorbent material can reduce the compressional wave sound, while Lorentz force balancing reduces the gradient coil sound.

5.4.3 Silent sequences

The greater part of what is described before, can be implemented in newly built scanners. For existing systems, substantial hardware modifications would be required. There are intelligent ways to deal with the scanner noise to avoid influence of scanner noise in functional imaging without these (expensive) hardware modifications (Amaro *et al.* [2002]).

Scanning techniques

Functional brain mapping uses the blood oxygenation level-dependent (BOLD) effect. After a stimulus has been presented, there is an increase in blood flow to the activated brain region to supply oxygen for the aerobic glucose metabolism. The MR signal depends on the oxygenation-level of the blood, therefore an increase in oxygenized blood flow results in an increase of signal. This hemodynamic response has a delay compared to the stimulus. Maximal MR signal is obtained 4–7 seconds after the stimulus, and the hemodynamic response is back to baseline after 12–15 seconds after stimulus onset. These numbers may depend on stimulus and the active brain area.

Scanner noise itself is a stimulus (see above), which also gives a BOLD response. The BOLD response of the scanner noise however, does not coincide with the BOLD response of a stimulus as acquisition is best done when the signal is highest. Continuous acquisition would lead to a baseline shift (in auditory fMRI), giving an apparent reduced response to stimuli. Hall *et al.* [1999] reported a sparse imaging technique, to map the auditory brain areas without scanner noise interference (figure 5.4B). An auditory stimulus is presented and the MR signal is recorded several seconds later. After the hemodynamic response of the scanner sound has vanished, the next stimulus can be presented. The repetition time can therefore be as large as 20 seconds. With more conditions of different stimuli, this can lead to undesirable long scanning sessions. As the hemodynamic responses might differ between subjects, there is a chance to miss the maximal MR signal response. Presenting stimuli of the same type repeatedly within one epoch elongate the hemodynamic response (figure 5.4C). A possible habituation effect is then not considered (Talavage *et al.* [1999]; Tanaka *et al.* [2000]).

A variation to this theme is presented by Yang *et al.* [2000]. Within a repetition time of 40 seconds between two auditory stimuli, both recordings of the BOLD response to the stimulus and of the rest condition are acquired. During the hemodynamic response due to the scanner noise, no acquisitions are made.

Assuming that the scanner noise only produces a baseline shift in the hemodynamic response, gives room for the clustered volume acquisition (Edmister *et al.* [1999]) or behavior interleaved gradient technique (Eden *et al.* [1999]). During the silent period, the auditory stimulus is presented so no scanner noise interferes with the stimulus (figure 5.4A). However, the observable dynamic range of the hemodynamic response in the auditory cortex may be affected. Resultantly, small task-related signal changes may not be observed due to scanner noise (Yang *et al.* [2000]).

In the case that continuous scanning is necessary or preferred, the scanning parameters can be adjusted to minimize the acoustic noise. The general shape of the acoustic transfer function of a gradient coils is a high-pass filter (cut-off at 600–800 Hz) with some resonance peaks (*e.g.*, from the banana-shape and the cone-shape

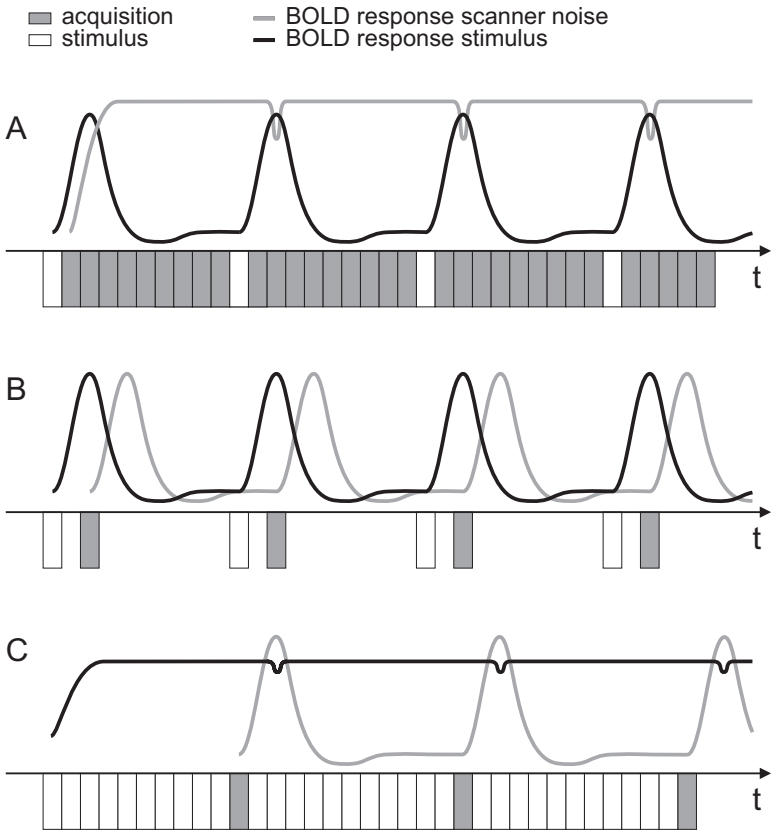

Figure 5.4: While continuously scanning, the BOLD response due to the scanner noise becomes stationary. Presenting an audio task, should lead to detectable variation of the BOLD response. A: The detectability of an audio task is enhanced by stopping the scanning while presenting the task. The variation of the BOLD response can also be too small to detect. B: Sparse sampling does not give interference between BOLD responses due to an audio task and scanner noise. C: Continuous presentation of one task condition gives a fairly constant BOLD response. The acquisition of images produces a BOLD response, but not at times of acquisition.

modes). The peaks in the spectra of the read-out gradient train pulses in EPI, and of any trapezoidal pulse, should not coincide with the peaks in the acoustic transfer function (Tomasi and Ernst [2003]; Wu *et al.* [2000]). Differences of up to 10–12 dB between read-out frequency and pulse-width settings are obtained. Making the ramps of the gradient pulses longer, automatically shifts the fundamental frequency to low frequencies, where the acoustic transfer is low, and the human ear is less sensitive (Brechmann *et al.* [2002]). This does, however, increase the acquisition time.

Sinusoidal gradients

Maximizing the slope duration is one of the guide rules for silent imaging, as set out by Hennel *et al.* [1999]. The gradient waveform should: (a) have sinusoidal gradient slopes, (b) have maximum slope duration, and (c) use a minimum number of slopes. Fast switching of gradients, introduces higher frequencies in the acoustic spectrum. Introducing soft transitions from one state to another, minimizes the harmonics that would be in the range of higher acoustic transfer. Thus limiting the bandwidth of the gradient pulses to $<$ 200 Hz, the bandwidth of the acoustic noise is also limited as the response to gradient pulses is presumably linear (Hedeen and Edelstein [1997]). In standard EPI, the time between consecutive pulses is too short to apply this technique. Applying this technique increases the acquisition time, initially limiting its use to anatomical images (Girard *et al.* [2000]) that are recorded with an SPL of 59 dB(A), just above background noise of 55 dB(A).

Later, it has been shown that this method could be improved by removing all plateaus in the gradient waveform, and use pure sinusoidal gradient waveforms (Hennel [2001]). This results in an additional 10–20 dB reduction in acoustic noise, in comparison to the use of only sinusoidal ramps. Image reconstruction first needs regridding as k-space trajectories are curved. This procedure is also necessary in spiral trajectory imaging (Oesterle *et al.* [2001]). Comparing image quality with standard pulse sequences yields only minor differences, while the acoustic noise is reduced significantly. Functional imaging with this silent technique is possible (Loenneker *et al.* [2001]; Marcar *et al.* [2002]). The BOLD response can be measured but needs a long imaging time and is therefore more sensitive to scanner drift. EPI is not replaced by this technique, but can be a better alternative when acoustic noise is not desirable. Examples are studying the influence of scanner noise, or when patients are unsettled, like pediatric of psychiatric patients.

SENSE

Undersampling k-space trajectories improves temporal resolution in MR imaging, or, with additional interpolation, it provides a better spatial resolution without changing acquisition time (Jesmanowicz *et al.* [1998]; Tsai and Nishimura [2000]). Ar-

tifacts and SNR changes due to this technique are discussed. One way to improve these limiting factors, is with Sensitivity Encoding (SENSE). Using a multi-coil array, images are obtained in less time, depending on the number of coils used (Pruessmann *et al.* [1999]). The sensitivities of the separate coils to the MR signal from one position are recorded, and these provide spatial encoding possibilities. fMRI is also possible with this technique (Golay *et al.* [2000]; Preibisch *et al.* [2003]).

SENSE can be used to acquire more lines in the same time as with full k-space imaging, or for faster imaging. By applying SENSE, but keeping the acquisition time constant, de Zwart *et al.* [2002] decreased the slew rates and the maximum gradient strength. This effectively lowers the harmonic frequencies of the gradient pulses (a change in pitch is reported), and lowers the Lorentz forces on the gradient coil structure. In this way, a reduction of the acoustic noise is achieved. Theoretically, with this method applied to rate-2 and rate-3 SENSE, a reduction of respectively 12 and 19 dB (linear) can be achieved. Averaged over three different scanners, reductions of 11.3 dB(A) and 16.5 dB(A) are found. When the read-out gradient was turned off, a reduction of 16.4 dB(A) was found. Other differences can be attributed to the shift of frequencies and scanner frequency response functions. Important to notice is that this application of SENSE does not significantly alter the sensitivity to detect brain activation.

5.5 General issues

This section presents some general considerations.

First, there are substantial differences between the measurement protocols that have been used in the sound pressure measurements reported so far. This complicates the evaluation.

Further, some sound recording devices may be affected by strong and changing magnetic fields and the RF pulses.

Sound pressure measurements taken some distance from the bore do not necessarily reflect the SPLs inside the bore. The levels outside the bore contain strong components generated by the scanner's outer shrouds, and also from multiple reflections from the walls. The same complexity makes the evaluation of reported attenuation more difficult. For the proper acoustical assessment, both room characteristics and precise microphone position and properties are required, and both attenuation outside the scanner and inside the bore should be reported.

In general, attenuation of acoustic waves is frequency dependent. It appears to be common practice, however, to present a single value. This is usually the attenuation value at the frequency for which maximum attenuation is achieved, which overestimates the broadband result. This can lead to the situation where frequency bands which at first sight looked harmless, are going to play an important role in the result. Formally, the sound pressure level is an rms measure, which averages across

a certain time window. It contains contributions from the entire spectrum.

Shifting frequencies of signal components, or the removal of higher frequencies in signals, changes the SPL. Therefore, when results are presented, the end value after sound reducing measures only has meaning when the frequency content of the pulse sequence is known. In that respect the comparison of scanners driven with 'worst case' sequences is of little value. Driving the scanners with the same gradient strengths, and same slew rates gives results that can be compared. The acoustic noise should in such a comparison be one of many parameters. In such a way it is like comparing a sports car and a family car driving at top speed, and only looking at fuel economy.

Displaying measured waveforms is of little use, just like presenting reductions in percentages. Under a factor 10 in amplitude reduction ($\triangleq$ -20 dB), a visual display is not able to give a precise impression of the achieved attenuation. Linear axes when displaying spectra, or frequency selective attenuation, does not lead to a correct idea of what is presented or achieved. In the end, the perception of sound pressure levels is about logarithmic scales. Presenting attenuations in percentages should therefore be discouraged. Further, it should be made clear whether the reduction comprises energy or waveform amplitude. Attenuations of 99 % in energy correspond to 20 dB reduction, while an attenuation of 99 % in waveform amplitude corresponds to a 40 dB reduction. Further, the just noticeable difference between sound pressure levels is about 1 dB. Presenting numbers in tenths of dBs does not add much value to the results that are found.

Finally, the general idea about linearity of gradient systems (Girard *et al.* [2000]; Hedeen and Edelstein [1997]) should be reconsidered. This is true for the occurrence of harmonic distortion and for a nonlinear amplitude response as well. When determining the acoustic transfer function, often only one current intensity is used. It has been shown that the sound pressure does not linearly increases with the Lorentz forces (Moelker *et al.* [2003b]).

5.6 Discussion and conclusion

A number of approaches, both passive and active, aiming to reduce MR-related acoustic noise, has been analyzed. In general, the attenuation results of more than one measure are not simply additive in dBs (= multiplicative in power). Moreover, it is necessary to consider the precise frequency characteristics of the single steps. MRI scanning at a lower rate changes the dB(A) level, because on the one hand, the fundamental frequency is reduced in strength under 500 Hz, on the other hand, more overtones are present in the frequency range from 500 to 4000 Hz.

Passive attenuation with earplugs and mufflers (the most widely used attenuators) gives less attenuation at the lower frequencies (Moelker and Pattynama [2003]). A combination with active noise reduction that performs well at low fre-

quencies, should give appreciable results. The combination of SENSE and a gradient coil in a vacuum chamber should also give good results, only until the eddy current evoked vibrations start to become the main contributor to the sound pressure.

The conclusion that acoustic noise need not be considered an annoying but unavoidable feature of MR imaging examinations (Girard *et al.* [2000]) is wrong. Effort should be put in to the research of sound reducing methods in (functional) MR imaging. The combination of various approaches should be tested to the limit to have the highest possible sound reduction.

Chapter 6

Determining the acoustic transfer function with frequency sweep signals[1]

6.1 Introduction

In this chapter, data acquired from a 1.5 T scanner are reported. The acoustic noise as a response to frequency sweep signal is recorded and analyzed as described in chapter 4. The variation of the sweep rate and the variation of the input signal amplitude are made to show possible differences between the responses to different sweep rates and input signal amplitudes, respectively. As already pointed out in chapter 5, the harmonic components are often neglected when determining transfer functions. The contribution of these harmonic components have been studied, and the necessity of the proposed sound pressure transfer function has been examined.

6.2 Results

In this chapter, a selection of the results for amplitudes and sweep rates from the X-gradient data are shown. The results for other amplitudes, sweep rates, and gradients yield similar results. Per analysis method, the transfer functions are calculated for all sweep rates and input signal amplitudes. All these transfer functions are then normalized to the highest transfer within this data set. Normalization was performed for reasons of confidentiality.

[1]The measurements described in this chapter are performed together with Larry de Graaf, Magnetic Resonance Laboratories, Eindhoven, The Netherlands.

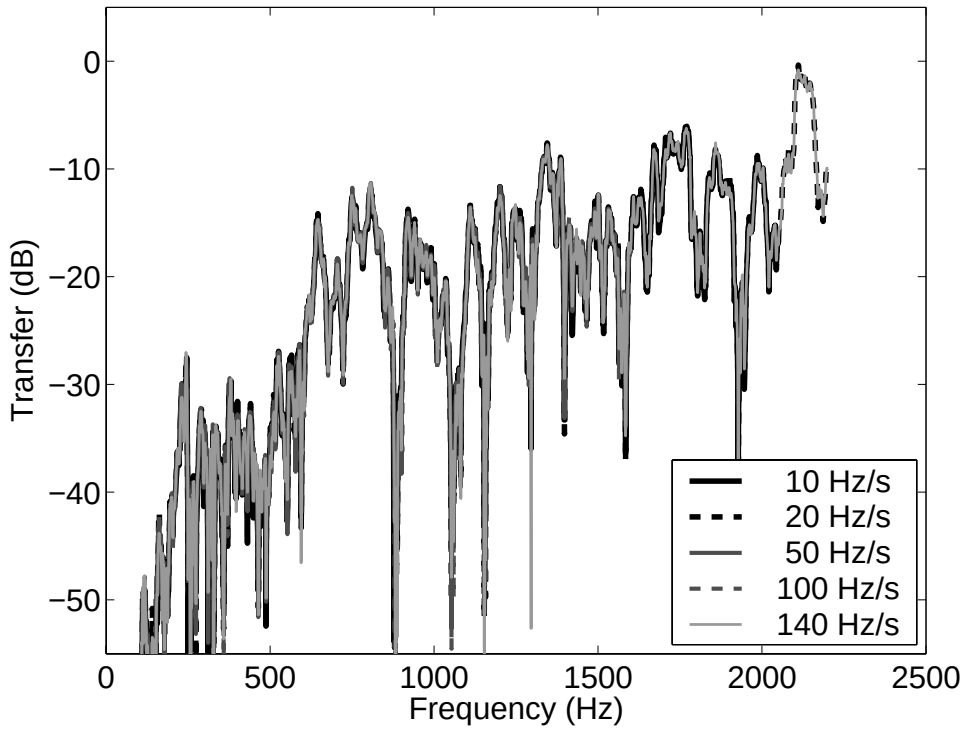

Figure 6.1: Frequency spectrum of the acoustic transfer function of an MR scanner. The amplitudes of the input signals are kept constant while the sweep rates were varied. The transfer is normalized to the highest value of transfer at 0 dB.

6.2.1 Fourier analysis

In this section, the transfer functions are derived by the division of output and input spectra. The transfer functions are obtained for a wide range of sweep rates (from 10 to 16384 Hz/s) and a wide range of input signal amplitudes (from 0.1 to 5.0 V, or less if clipping occured), as explained in more detail in chapter 4. Differences between these input signals are most prominent at frequencies of low transfer.

Figures 6.1, 6.2, and 6.3 present results for one constant input signal amplitude (0.5 V). All sweep rates lead to equally shaped transfer functions. The differences between the different sweep rates can mainly be found in the troughs of the transfer functions. With increasing sweep rate, the depth of the troughs reduces, as does the frequency resolution (figure 6.3). Due to the low frequency resolution, especially the frequency ranges with high dynamics in transfer are influenced by the increasing sweep rate.

The results for all different amplitudes obtained at one sweep rate (20 Hz/s) are shown in figure 6.4. For a large part of the spectrum, the transfer is independent of

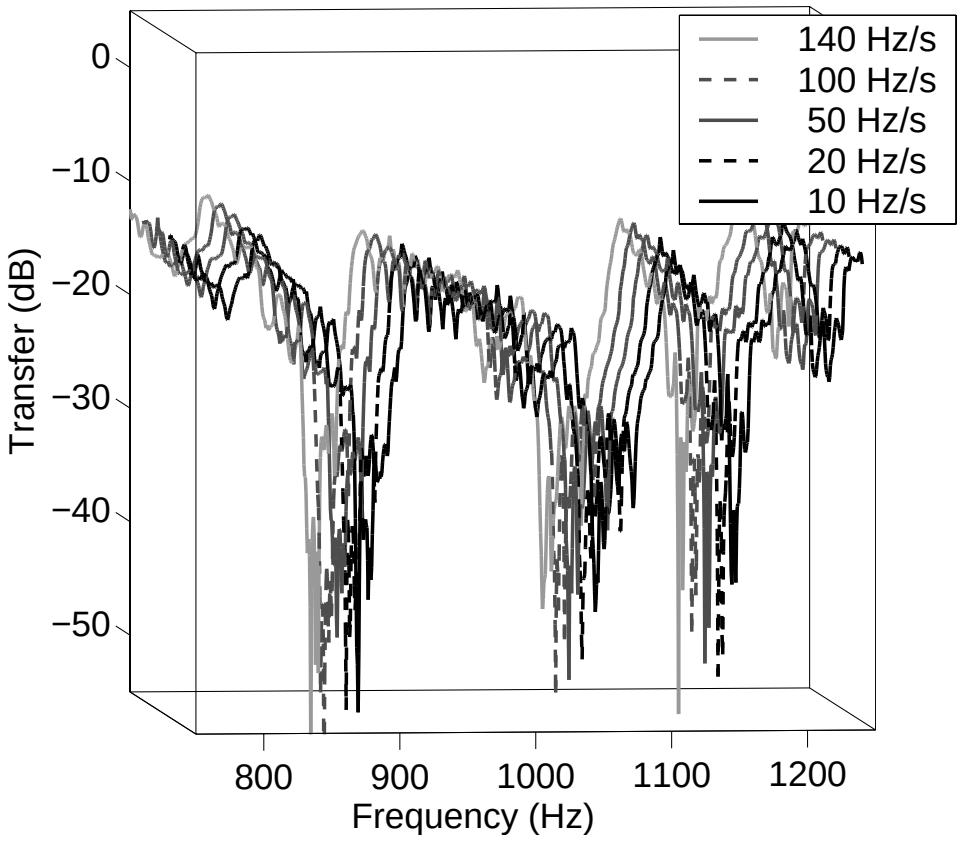

Figure 6.2: All parameters as in figure 6.1. The frequencies between 750 and 1250 Hz are shown. For clarity, the graphs are shown in a 3D plot. The transfer is equal at high transfer, and at low transfer, the differences can clearly be seen.

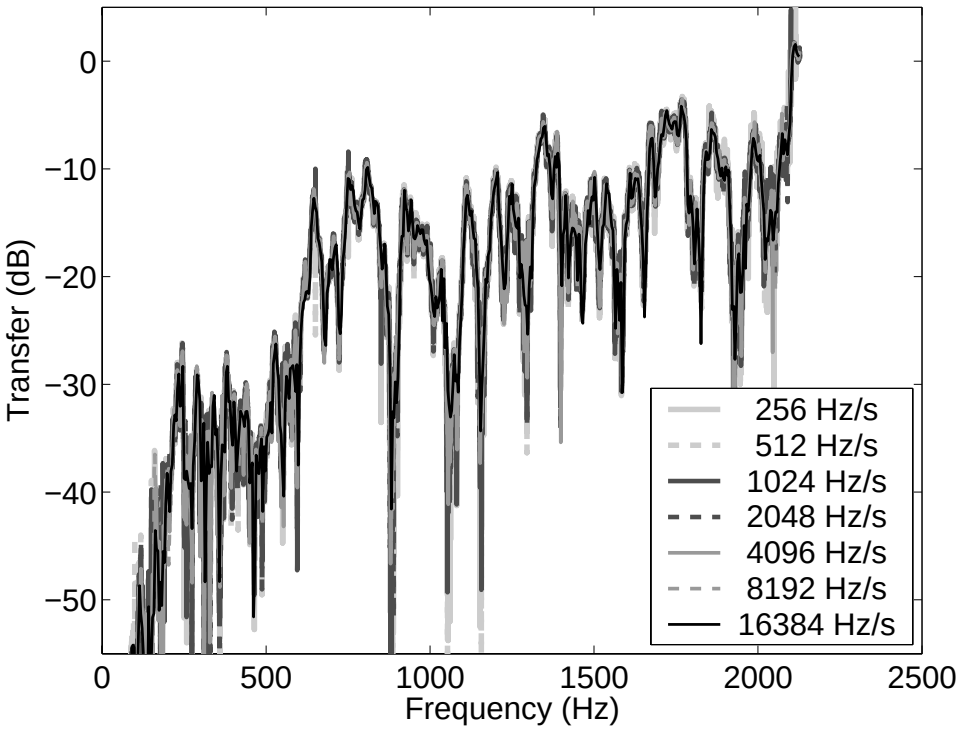

Figure 6.3: Frequency spectrum of the acoustic transfer function of an MR scanner. The amplitudes of the input signals are kept constant while the sweep rates were varied. The transfer is normalized to the highest value of transfer between 150 and 1500 Hz at 0 dB.

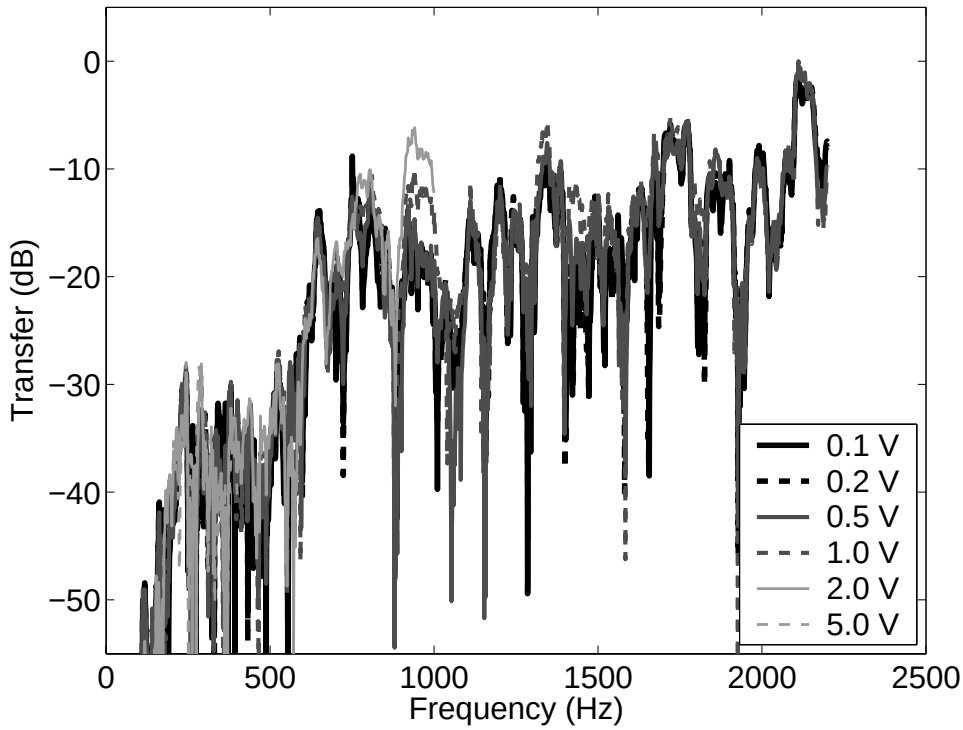

Figure 6.4: Frequency spectrum of the acoustic transfer function of an MR scanner. The sweep rates of the input signals are kept constant at 20 Hz/s while the amplitudes were varied. The transfer is normalized to the highest value of transfer at 0 dB.

amplitude. Again, differences are primarily found in the troughs. Notably around 800 and 940 Hz the transfer increases with increasing input signal. For input signals with amplitudes of 2.0 V and 5.0 V, the transfer is only derived up to 1000 and 550 Hz, respectively, as the distortion due to system limits became too high for higher frequencies. From figure 6.5, it can be seen that the transfer is not independent of input signal amplitude. This might explain the nonlinearities as found in Moelker *et al.* [2003b], with the difference that in that experiment the magnetic field strength was changed. Both changing the magnetic field strength and keeping the gradient currents the same, and changing the gradient current amplitudes at a constant magnetic field strength, lead to a variation of the Lorentz forces acting on the gradient coil structure.

6.2.2 Root-mean-square

In the previous section, the transfer functions are calculated without considering produced harmonic distortion. By using a root-mean-square method as proposed in

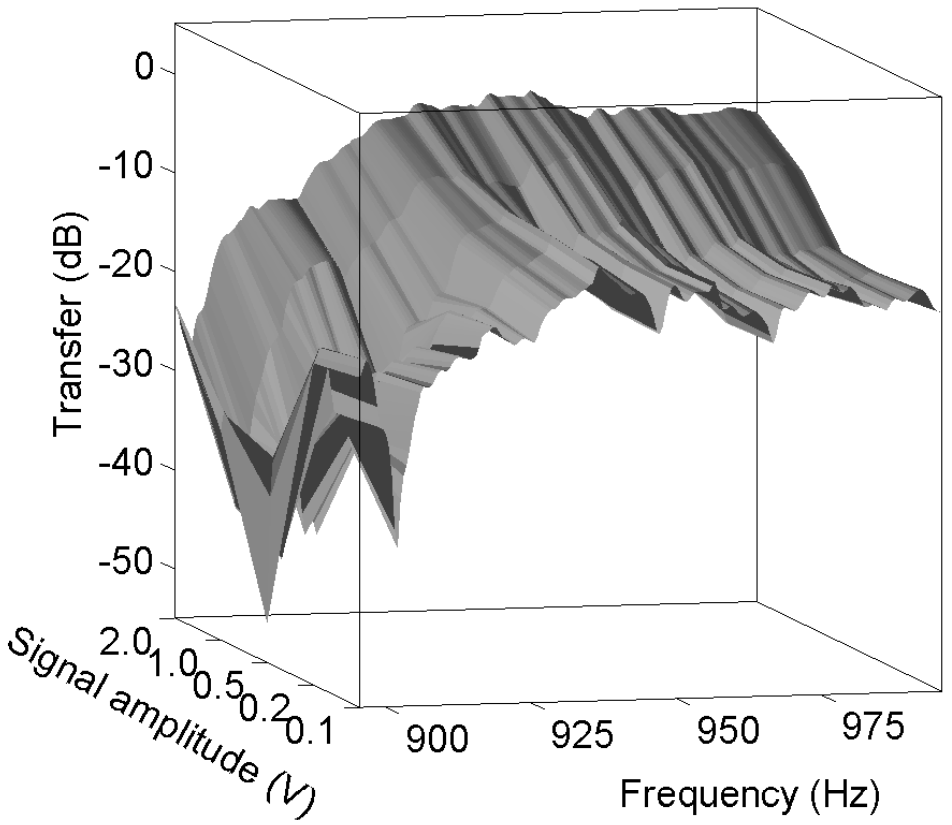

Figure 6.5: Part of the spectra as displayed in figure 6.4. The transfer is not linear with respect to amplitude, not even at frequencies of high transfer. This in contrast to figure 6.2, where the transfer is constant over the variable sweep rate.

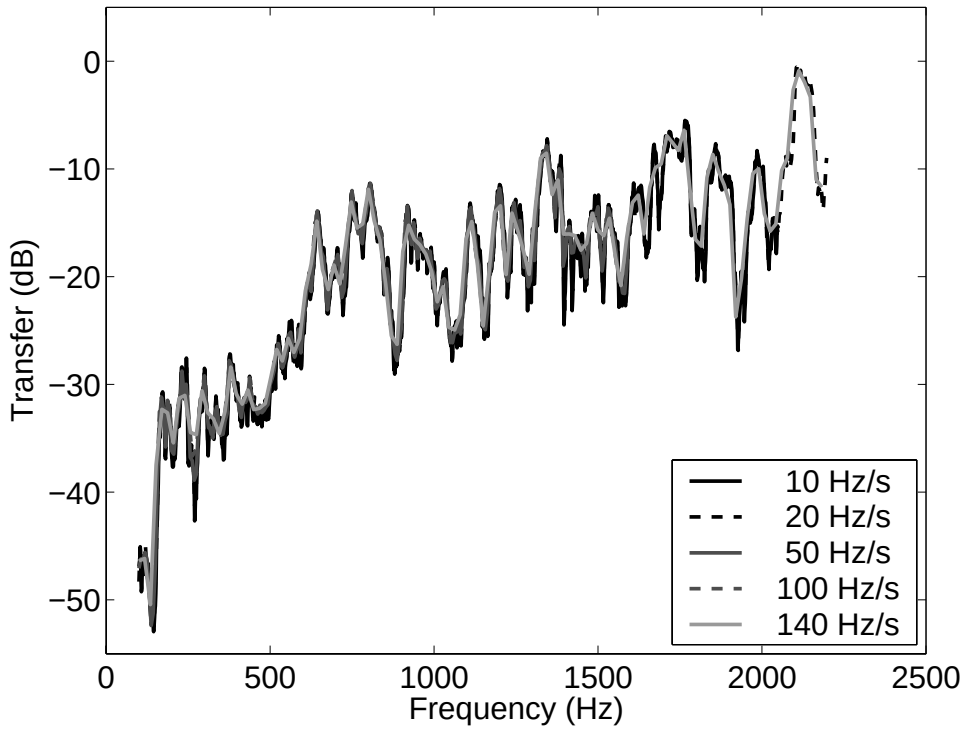

Figure 6.6: Frequency spectrum of the acoustic transfer function of an MR scanner determined with the rms method. The amplitudes of the input signals are kept constant while the sweep rates were varied. The transfer is normalized to the highest value of transfer at 0 dB.

section 3.5, all produced sound pressure is considered. Such transfer functions are presented in this section.

The acoustic transfer of the scanner is presented in figure 6.6, for all sweep rates between 10 and 140 Hz/s. Only results of one input amplitude (0.5 V) are presented. For the peaks, there is no significant difference between the rms method and the Fourier method (figure 6.1); for the troughs on the other hand, the differences are prominent. The variation in transfer of over 40 dB are brought back to only 15 dB. With increasing sweep rate, the frequency resolution drops. This is most notable around 250 and 1430 Hz, where the dynamics of the transfer function are decreased due to spectral smearing.

In figure 6.7, the results from one sweep rate are given for all input amplitudes. As in figure 6.4, around 800 and 940 Hz an increase in transfer is shown with increasing input signal amplitude. In addition to this, at frequencies below 700 Hz, the transfer is not linear with input signal amplitude.

Two effects are important for the latter result: first, at low signal amplitude

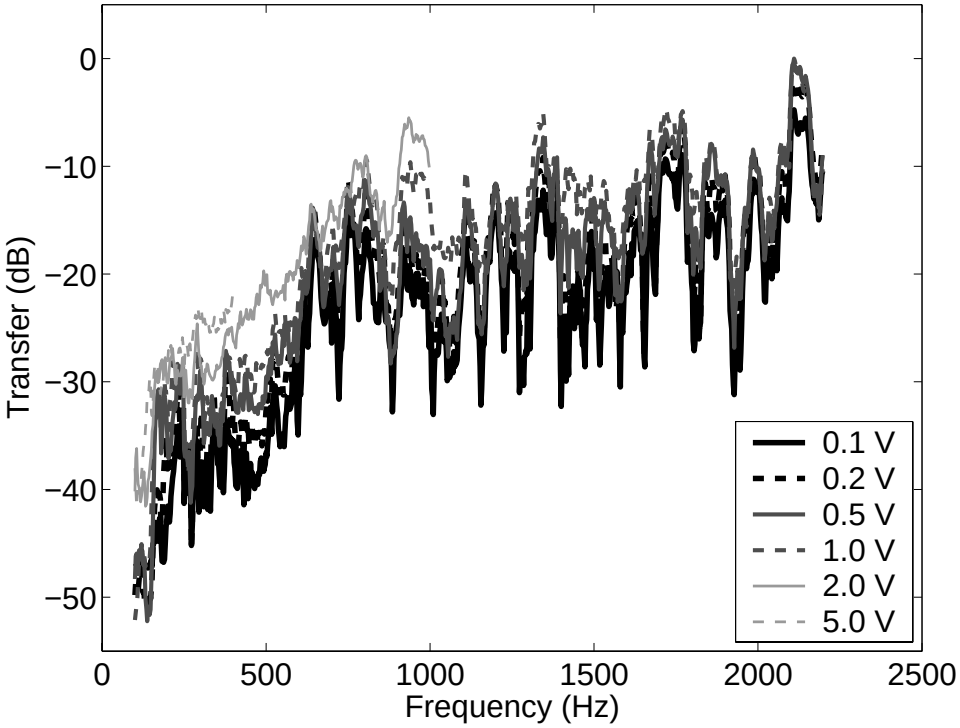

Figure 6.7: Frequency spectrum of the acoustic transfer function of an MR scanner determined with the rms method. The sweep rates of the input signals are kept constant while the amplitudes were varied. The transfer is normalized to the highest value of transfer at 0 dB.

with low frequencies, the signal-to-noise ratio (SNR) is very low for the gradient current. Secondly, there is an increase in total harmonic distortion (THD). To show that the contribution of harmonics to the acoustic output cannot be ignored, the total harmonic distortion (THD) for the bandwidth of interest is calculated:

$$\mathrm{THD} = 20 \log_{10} \frac{\sqrt{\sum_{n=2}^{7} a_n^2}}{a_1}, \tag{6.1}$$

where a_1 and a_n are the amplitudes of the fundamental and the nth harmonic respectively.

The current amplifiers produce a constant electric background hum with a broad spectrum. For the rms transfer, this means that the denominator in the transfer function (I_{rms}) is fairly constant at low frequencies; with an increasing numerator (p_{rms}), this gives an increasing transfer with increasing input signal amplitude. The acoustic response has a much better SNR, and is therefore hardly hampered in this analysis: the acoustic output caused by the sinusoidal gradient current is always above the background noise. With both increasing signal amplitude and increasing frequency, the THD of the gradient current increases. This has a distinct effect on the acoustic output, which also shows an increase in THD with increasing input signal amplitude. The SNR is significantly higher at these amplitudes, so the increase in transfer with increasing signal amplitude is THD governed. If at high input signal amplitudes the frequency becomes too high, then the gradient current displays as a triangular signal. The THD of the gradient current then rises to almost -20 dB, which is close to the THD of -18 dB for perfect triangular signals.

6.3 Discussion

For a system that is linear, the transfer should be independent of amplitude and therefore the transfer functions for the different input signal amplitudes should overlay.

The comparison of figures 6.1 through 6.3, shows that the shape of the transfer function is not depending on the sweep rate, except for the frequency resolution, which decreases with increasing sweep rate (figure 6.3).

Decreasing trough depth with increasing sweep rate may be explained by the same energy of the response signal being distributed over fewer bins, thereby increasing the energy content per bin.

The results of the root-mean-square method, displayed in figure 6.6, show the same general shape as the Fourier method, except for the deep troughs in figures 6.1 through 6.3. Here, the frequency resolution of the transfer function decreases with increasing sweep rate due to the increasing bandwidth covered in the time used for averaging.

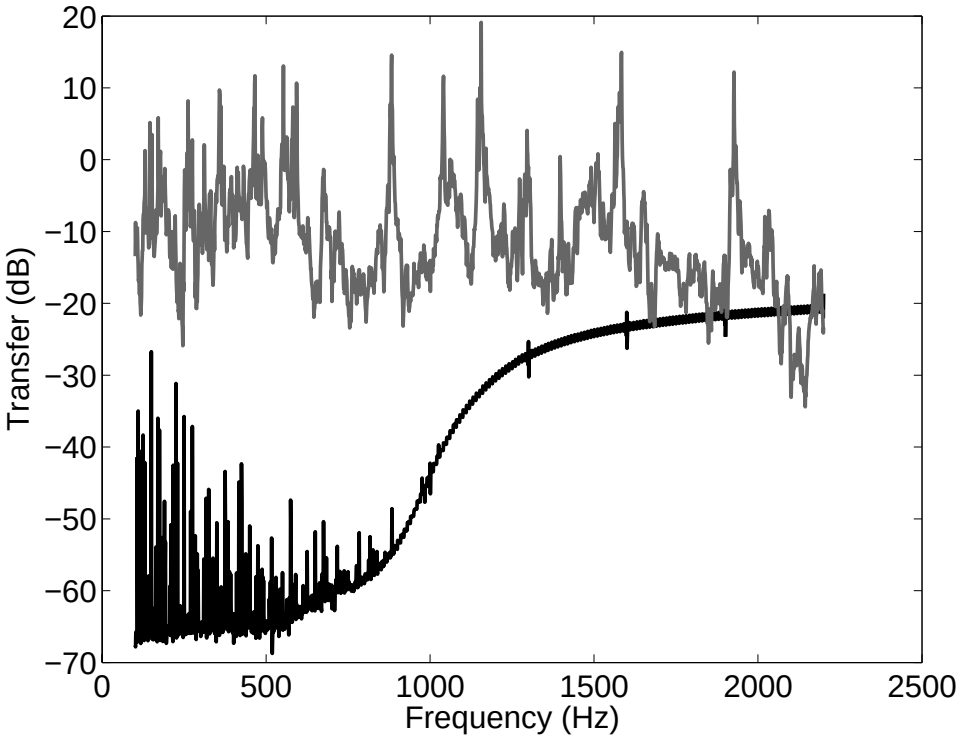

Figure 6.8: Total harmonic distortion for the gradient currents (black trace, 1.0 V input signal amplitude) and the sound pressure (grey trace), as a function of frequency.

For the rms method, the transfer at frequencies below 700 Hz is higher than for the Fourier method. This can be explained by harmonic distortion, which contributes significantly to the sound pressure level.

In figures 6.4, 6.5, and 6.7 around frequencies 780, 940, and 1340 Hz, it can be seen that the transfer increases with increasing input signal amplitude, while at other frequencies, within a few dBs range, the transfer does not change with amplitude. The mentioned frequencies are probably resonance frequencies of the scanner system, where little input energy is needed to generate a high response.

In all graphs obtained with the Fourier method (figures 6.1 through 6.5), deep troughs are present in the transfer function. At these frequency locations, the transfer is never the same for different amplitudes nor for different sweep rates. When such low transfers are not reproduced over input signal amplitudes or sweep rate, it is not sensible to assume that these transfers are correct, in particular because the rms method gives consistent results over input signal amplitudes and sweep rates alike. This effect of low transfer must be a result of taking the Fourier transform, where harmonic distortion is neglected.

6.4 Conclusions

Frequency modulated signals give a good control of input signal amplitude and frequency; therefore, these signal are suitable for determining the acoustic transfer function.

The sweep rate is of little importance when the transfer function is determined by dividing the Fourier transform of the output signal by the Fourier transform of the input signal, as long as the frequencies in the signals concur with the Nyquist theorem. The sweep rate becomes important when the transfer function is determined by the ratio of the root-mean-square values of the sound pressure and the gradient current. With this method, the frequency resolution drops with increasing sweep rate. Another downside is that this method is sensitive to background noise present in the scanner, this negative effect disappears when the sound caused by the changing gradient currents has a sufficiently higher SPL than the background noise. Electric noise or hum from the gradient amplifiers may also result in incorrect transfer for low signal amplitudes in combination with low frequencies.

If the resonance frequencies or the eigenfrequencies of the MRI scanner need to be found, then frequency sweep signals, in combination with the root-mean-square method, provide an easy and fast method to determine the absolute value of the transfer function. With this method, as it is described in chapter 3, the phase information is not obtained. As the signal, obtained by convolving the transfer function with the current time signal, will be time-averaged as well, this phase information is not important.

Once the eigenfrequencies are determined, these frequencies should be avoided

in the gradient currents. Apart from these eigenfrequencies, the sound pressure can be accurately predicted with the transfer functions as these are almost independent of input signal amplitude.

The major advantage of a transfer function obtained with the root-mean-square method, is that it will give a more accurate prediction of the sound pressure than the transfer function obtained with the Fourier method. In this root-mean-square method, all sounds present during scanning are taken into account, including harmonic distortion and noise. This is especially relevant at frequencies of low transfer, which is interesting to make a scanner more quiet.

Chapter 7

Comparison of transfer functions

7.1 Introduction

The analysis of frequency sweep signals in the previous chapter, showed differences between Fourier analysis and the rms method. Transfer functions are also derived by measuring noise responses (Hedeen and Edelstein [1997]) and pulse responses (Tomasi and Ernst [2003]). These are broadband signals that present all frequencies at the same time. In this chapter, first the transfer functions are presented from the broadband noise input signal and the pulse signal; these are derived with Fourier analysis. Second, the frequency sweep signals are analyzed by Fourier analysis and by the rms method. The data are acquired on a 3 T scanner.

7.2 Results

Here, only results for the X gradient are shown. The data for the Y and the Z gradient are analyzed in the same way and produce the same differences with respect to analysis method. Resonances occur at different frequencies for the Y and Z-gradient coils.

To obtain transfer functions for A-weighted SPLs, the sound pressure data can be weighted before determining the transfer function.

7.2.1 Noise response

For 25 seconds, pink noise (bandwidth from 40 to 3500 Hz, 0.2 V rms amplitude) was presented directly to the gradient amplifier input and the sound pressure in the scanner's isocenter was recorded. 50 successive 0.5-second pieces of data are

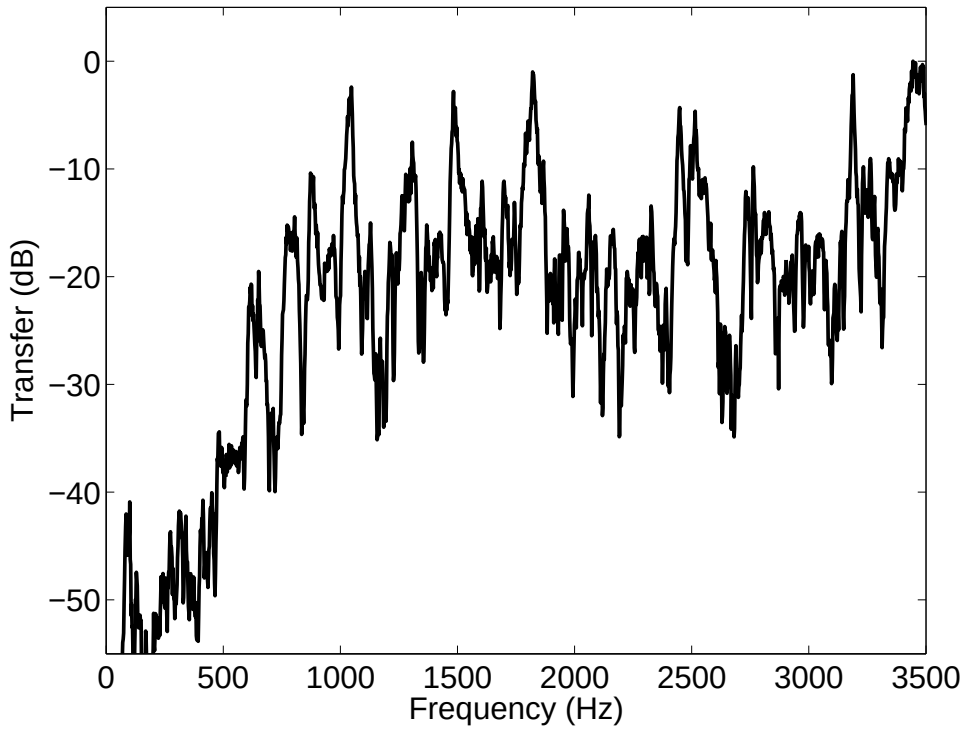

Figure 7.1: Noise transfer function (normalized).

considered to be repetitions of the noise experiment. Pieces of 0.5 seconds are chosen to still have a good frequency resolution and also to have a high number of repetitions for averaging (Papoulis [1984]). Over the bandwidth of interest, the gradient currents showed a spectrum corresponding to pink noise; because of the noisy features of the input signal, instead of dividing by the spectrum of the noise gradient current, a theoretical adjustment of the sound pressure spectrum is made by multiplying the Fourier transforms with the square root of the frequency. The resulting transfer function is plotted in figure 7.1.

7.2.2 Pulse response

The pulses as described in section 4.2.2, were the shortest possible pulses that could be programmed on the scanner. Six pulses and the acoustic responses were recorded and the Fourier transforms were taken of 6 samples of 1 second long, all beginning directly before the rise of the pulse current.

The full-width half-maximum of 0.4 ms of the pulses gives zero amplitude in the spectrum at integer multiples of 2500 Hz, this means that at these frequencies, the transfer cannot be calculated with meaning. The high peak in the transfer at 2500

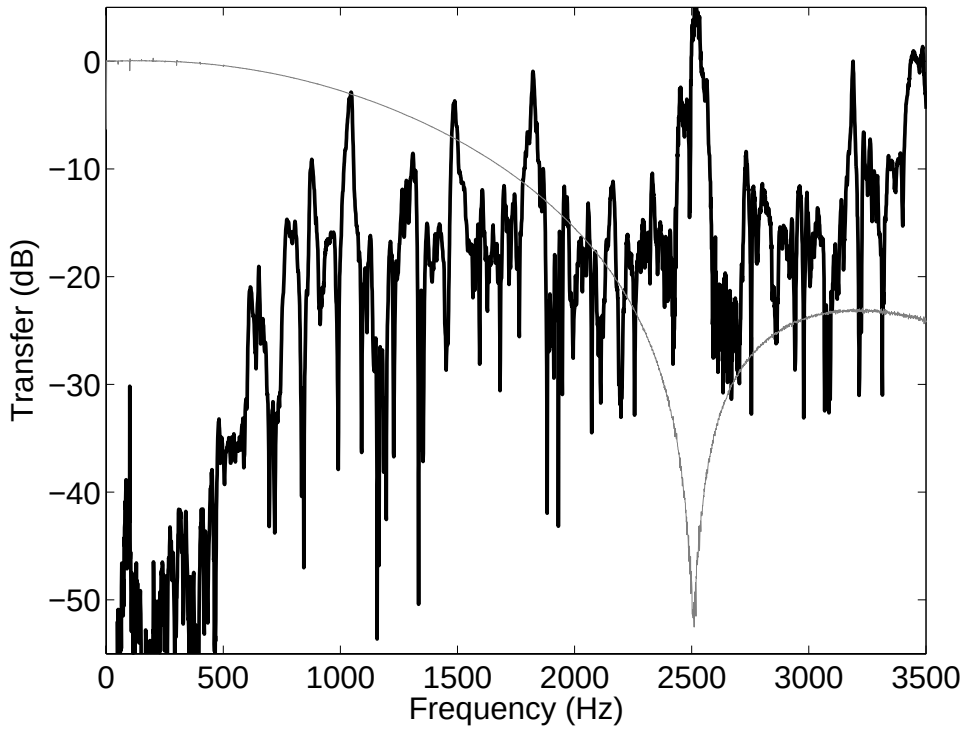

Figure 7.2: Pulse transfer function (normalized). The black line is the transfer function, and the grey line is the Fourier transform of the pulses. At 2500 Hz, a clear minimum is visible in the spectrum of the pulses; at this frequency, the transfer function cannot be calculated with meaning.

Hz (figure 7.2) should therefore not be considered.

7.2.3 Frequency sweep response

The acoustic response of the scanner to frequency sweep signals is analyzed by dividing the output spectrum by the input spectrum, and the proposed root-mean-square method (equation 3.9).

The input signal amplitude was varied between 0.1 Volts and 5.0 Volts (see also appendix A.1), where 10 Volts is maximal for the input signals. The sweep rate of 20 Hz/s was chosen to give a good enough frequency resolution when averaging takes place over 125 ms (equation 3.17).

Fourier analysis

Before taking a Fourier transform of the data, a Kaiser-Bessel window ($\beta = 10$) was multiplied with the data. The width of the window equalled 2 seconds, where the

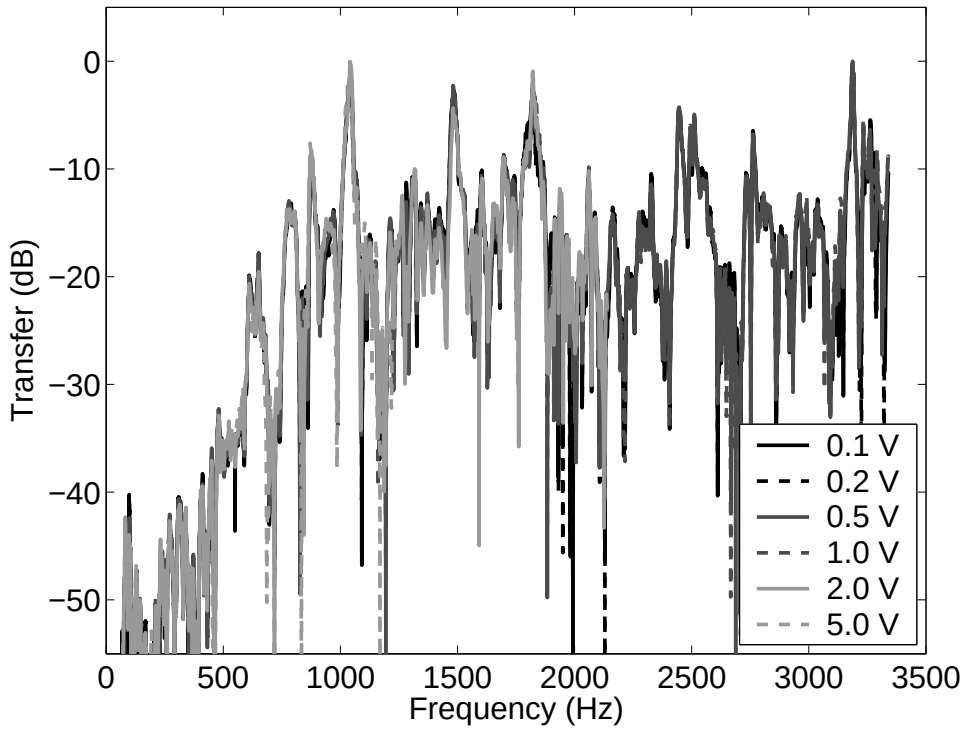

Figure 7.3: Frequency sweep transfer function, derived with Fourier analysis (normalized). All input signal amplitudes result in transfer functions that are identical at resonance frequencies but differ considerably at frequencies of low transfer.

window was stepwise shifted by 0.5 seconds (see figure 4.2). After deriving the transfer function for the 2 seconds of data, the part of the spectrum corresponding to the central 0.5 seconds (thus corresponding to 10 Hz) was stored. All small parts combined give the complete transfer function (figure 7.3) for the bandwidth of interest.

Harmonic distortion

On playback of the recorded sound, there is a considerable dynamic range in the sound pressure level, but not the 50 dB suggested by figure 7.3 in some limited bandwidth (*e.g.*, 1000–1200 Hz). Calculating the SPL over time (and with a frequency sweep thus over frequency) shows a dynamic range under 35 dB within the same limited bandwidth.

Figure 7.4 displays the THD for the sound pressure (upper trace) and the electric gradient current (lower trace). For all frequencies, equation 6.1 is evaluated and the calculated THD is displayed at the fundamental frequency. The distortion of the

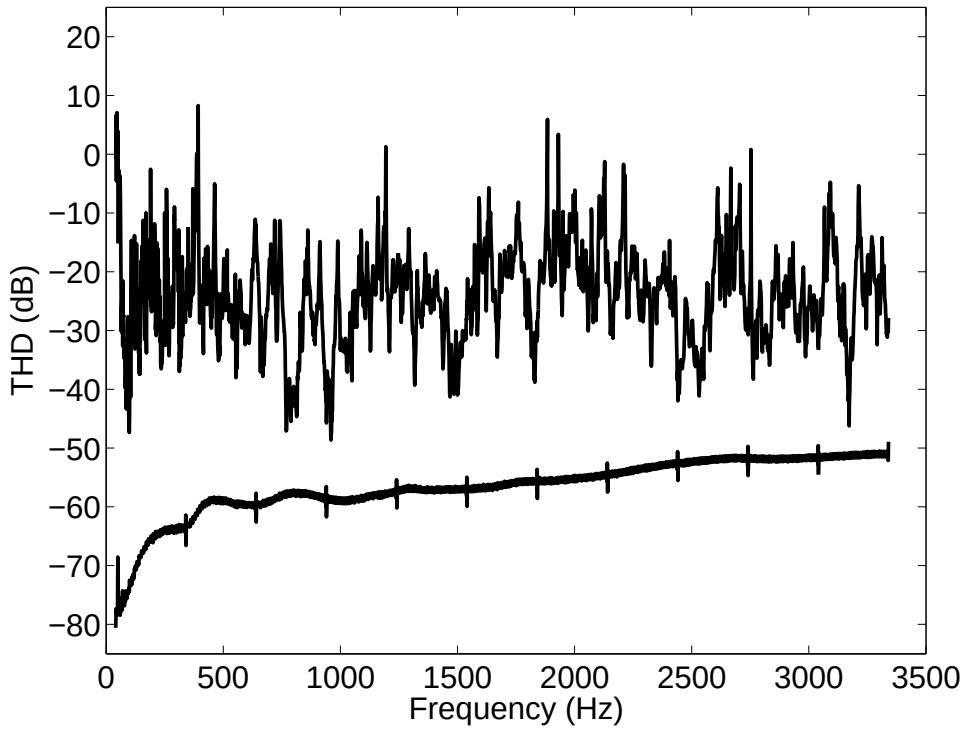

Figure 7.4: Total harmonic distortion for the sound pressure (upper trace) and the electric gradient current (lower trace). Results are shown for one signal amplitude (1.0 V). The little peaks in the lower trace at 300-Hz intervals are caused by overlap between the acquired data files. The maxima in the THD are at frequency locations where the (sweep) transfer function derived with Fourier analysis has extreme minima (see figure 7.3).

sound pressure is hardly caused by the distortion in the gradient current as this trace stays well under the THD trace of the sound pressure.

Root-mean-square analysis

The root-mean-square values of the sound pressure and the gradient current were calculated in consecutive 125 ms long pieces of data. For the sound pressure, this leads to the SPL. The quotient of the rms values (equation 3.9) gives the sound pressure transfer at the frequency of the input signal. For the complete spectrum and the various input signal amplitudes, these data are shown in figure 7.5.

For the low frequency part of the transfer function, the background noise SPL present in the scanner room is higher than the SPL generated by the gradient currents. Only with higher amplitudes of the input signal, the gradient noise rises above the background noise (horizontal lines at the low frequency part of the trans-

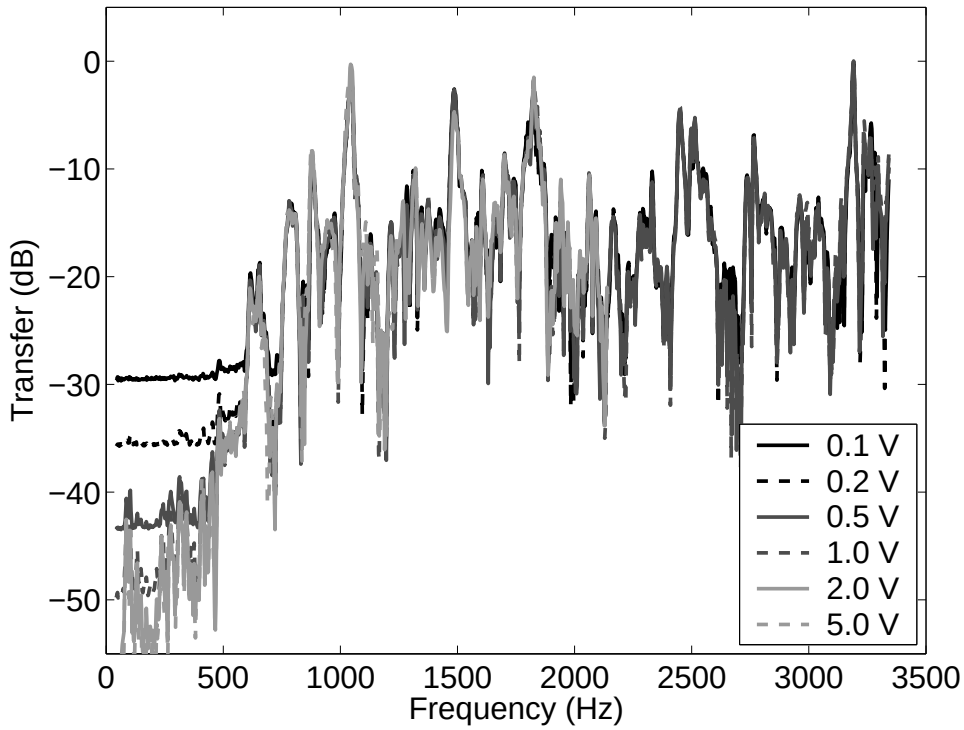

Figure 7.5: Frequency sweep transfer function, derived with root-mean-square method (normalized). All input signal amplitudes result in transfer functions that are identical at resonance frequencies. At frequencies of low transfer, the root-mean-square method leads to transfer functions that are almost identical with respect to amplitude. Below 480 Hz the gradient noise is below the background noise for the lower input signal amplitudes.

fer). With sufficiently high signal-to-noise ratio, the transfer is largely input signal amplitude independent. In comparison to figure 7.3, the deep troughs in the transfer disappear. This disappearing is not due to spectral smearing, *e.g.*, that surrounding frequencies contribute to the transfer at the frequency of interest. Analyzing the data with a time averaging window of only 1.3 ms also gives a transfer function without deep troughs.

7.3 Discussion

Comparison of the four different transfer functions (noise, pulse, sweep-rms, and sweep-FFT) reveals similarity at the peaks, and differences at the troughs. The peaks of the different transfer functions are within a 4 dB range, except for the peak around 2500 Hz in the pulse transfer function (figure 7.2). The deep troughs

in figure 7.3 show a dynamic range of about 50 dB in transfer within a limited bandwidth, while the rms analysis does not show more than 35 dB in the same limited bandwidth. The difference between the two methods can be explained by harmonic distortion, which contributes significantly to the sound pressure and is not considered by Fourier analysis of the spectra.

Further, in the responses to the noise input signal and the pulse input signal, the distortion caused by one frequency overlaps with first order responses to other input signal frequencies. This affects the transfer functions derived with noise or pulse input signals, but it is impossible to tell which frequencies are affected most. The absence of deep troughs is not the result of a poor signal-to-noise ratio to the background noise, as the spectrum of the noise response is above the background noise spectrum for frequencies above 500 Hz (not shown). By assuming linearity and not considering harmonic distortion, Hedeen and Edelstein [1997] have overlooked these problems in their noise transfer function.

For the pulse response, the finite length T of the pulse must be taken into account. In our case, one of the major peaks in the transfer function was at the frequency $1/T$; only taking the spectrum of the acoustic response does not reveal this peak. This may have happened in the research of Tomasi and Ernst [2003]. Compensating with the spectrum of the pulse is not possible, as the spectrum is undefined at the frequency $1/T$.

For the root-mean-square analysis, the background noise level is too high to determine the transfer below 480 Hz at the lowest input amplitudes (0.1–0.5 V, figure 7.5). For the other amplitudes, the acoustic response stays above the background noise, so the background noise is not a limiting factor.

As pointed out by Hennel *et al.* [1999] and Marcar *et al.* [2002], the use of sinusoidal gradients and low gradient slopes can reduce the acoustic output of the MR scanner below background noise. This is due to low transfer at low frequencies. Low frequencies result in long acquisition times while full brain recordings during functional MRI are made in seconds, not minutes. Standard EPI read-out frequencies are around 800 Hz; because of the trapezoidal gradient currents, the acoustic response will also be 800 Hz with the accompanying overtones. Using sinusoidal gradient currents with frequencies above 800 Hz, provides a maximal sound pressure level reduction of 25 dB for this scanner.

The major differences between the methods for deriving transfer functions are found in the regions of low transfer, the very regions we are interested in. From the three methods using Fourier analysis, the frequency sweep data gives the deepest troughs in the transfer function. This is not due to the higher acquisition time for the frequency sweep data, providing a higher frequency selectivity, it is solely caused by omitting the harmonic distortion.

During our experiments, the amplitudes of the signals to the scanner could easily be adjusted. Differences in transfer between the transfer functions for different input amplitude signals quickly reveal nonlinearities in the system. The depths of

the troughs differ for the different input signal amplitudes. For frequencies above 800 Hz, in the Fourier method, the differences are often over 20 dB, whereas in the rms method, the differences are never above 16 dB.

7.4 Conclusions

To determine the transfer function of a system, the bandwidth of interest has to be presented to the input of the system. If input signals that synchronically offer the complete bandwidth of interest are presented, then no discrimination can be made between contributions by first order responses and distortion.

For a good frequency separation, all frequencies in the bandwidth of interest have to be presented separately. Frequency sweep signals are well fit to do so. Piecewise analysis of frequency sweep signals shows distortion after Fourier transformation; this distortion is not considered when the ratio of output and input spectra is taken to be the transfer function.

The harmonic distortion is considered when the average sound pressure produced by a single frequency input signal is related to the electric gradient current. This especially enhances the transfer function at frequencies of low transfer, which are important for low acoustic output during MR scanning. Such a transfer function can only be used to predict sound pressure levels.

Gradient currents in fMRI experiments are usually trapezoidal shaped, resulting in a series of frequencies that are presented to the scanner. By changing the readout frequency, these frequencies shift. All these frequencies have to be considered to predict the maximum sound pressure level reduction in fMRI. With sinusoidal gradient currents, the maximum reduction from the worst case (which may be 130 dB for 3T MRI scanners) is 25 dB for this scanner. This still leaves sound pressure levels over 100 dB during fMRI.

Acknowledgments

The authors would like to thank Anita Kuiper, MRI technician at the BCN Neuroimaging Center, Groningen, The Netherlands, and Patrick Limpens and Paul Bunk from Philips Medical Systems, Best, The Netherlands, for their technical assistance.

Chapter 8

Considerations in laser Doppler interferometry of MR scanner bore vibrations[1]

8.1 Introduction

During magnetic resonance imaging (MRI), Lorentz forces acting on the gradient coil array induce vibrations. These forces are inherent to the technique, and different approaches are investigated to reduce the effects of these vibrations. One of these effects is acoustic noise. The vibration distribution over the outer surfaces of the scanner is complex, and depends on the location of the coils and their suspension. Quantifying these vibrations and their distribution can give insight in the contribution of different parts of the scanner to the acoustic noise. This sound source localization can lead to directed vibrational control. These data can also be used for predicting the sound field inside the scanner.

Measuring the vibrations of the scanner's surfaces can be performed with vibration transducers, such as a piezoelectric transducers or laser Doppler interferometry. Piezoelectric transducers have been used in the MR environment (Tomasi and Ernst [2003]) to detect and quantify vibrations. Apart from the extra load on the vibrating surface, piezoelectric transducers may be sensitive to magnetic fields, and therefore the functioning may be hampered. The advantage of laser Doppler interferometry (LDI) is the contact-free measurement, but LDI poses other difficulties to overcome. This chapter discusses these difficulties.

First, the choice of interference method is motivated. Secondly, the theory of

[1] This chapter is written in close collaboration with Kees Smith, master student at the Biomedical Engineering department in Groningen.

the Doppler effect and the mathematics of interferometry are discussed. Then, the practical considerations and limitations for laser Doppler interferometry inside the MR scanner bore are discussed.

8.2 Laser interferometers

A laser interferometer is capable of showing displacements in the order of nanometers, which has been used by Michelson in his famous experiment. The purpose of the laser interferometry setup is to combine two beams of light. The parallel and overlapping beams interfere and produce a pattern that depends on the frequencies of the respective beams, and their phase difference. The use of a standard interferometers to detect vibrations in the nanometer order is not feasible. The changing interference pattern will vary noticeable, but be relatively stable, *e.g.*, the fringes are not displaced much. The variation of the resulting signal is too small for easy processing. Using two monochromatic beams with light of different frequencies, leads to a constantly changing phase difference, and consequently, an interference pattern that changes correspondingly. By modulating the optical path length in one of the beams, the change of the interference pattern is modulated in conformance with the change in optical path length.

Such use of a Michelson interferometer is not possible without extensive modifications to the standard setup. With one laser source, after the beam splitter, the frequency of at least one beam has to be shifted. After scattering, the beams must be brought together. In the standard setup, this is done with the same beam splitter. The returning beam(s), however, cannot pass trough the frequency shifter(s) again.

The Mach-Zehnder interferometer splits the original light beam into two beams. In such a setup, the frequencies of both beams can be shifted free from problems. However, the vibrating surface cannot be in the optical path in a standard setup. A modification to the setup is given below where the laser beam is guided to the vibrating surface and is reflected back to the setup. The transfer of the laser to the vibrating surface can be done by either free-beam (figure 8.1) or by a fiber (figure 8.2). Both setups are discussed briefly.

8.2.1 Mach-Zehnder based interferometer

The interferometer in figure 8.1 consists of two mirrors and three half-silvered mirrors. The half-silvered mirror HM1 divides the beam coming from the laser L into two beams. Half mirror HM2 deflects the incoming beam to the vibrating mirror M1, this is called the target beam. The returning beam is combined at half-silvered mirror HM3 with the so-called reference beam, which travels via mirror M2. The combined beams fall onto the detector D. The Bragg cells B1 and B2 shift the frequencies of the laser beams.

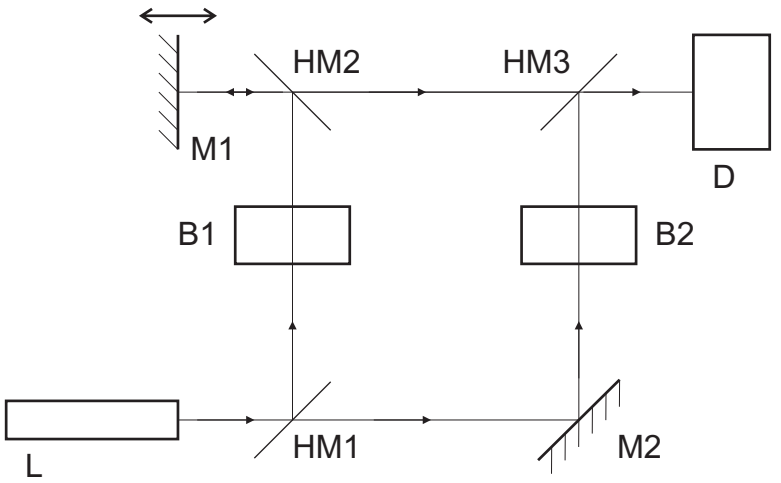

Figure 8.1: The setup for a Mach-Zehnder based interferometer.

8.2.2 Mach-Zehnder based interferometer with fibers

In the basis, the setup in figure 8.2 differs only from the previous with the replacement of mirror M2 by a fiber F2, and the inclusion of a fiber F1 in the path to the vibrating mirror M1. The length of fiber F2 should be twice the length of fiber F1. The light traverses F1 twice and the optical path length is therefore equal in both arms.

8.3 Theory laser Doppler interferometer

In this section, the theory is presented which describes the detection of the velocity of a vibrating surface. This surface is assumed to vibrate sinusoidally, with an amplitude A_M and a frequency ω_M. The resulting displacement x_M and velocity u_M are:

$$x_M(t) = A_M \sin(\omega_M t) \tag{8.1}$$

$$u_M(t) = \omega_M A_M \cos(\omega_M t). \tag{8.2}$$

It is shown that the theory can be generalized to all vibrations.

8.3.1 Doppler shift

In a reference frame, laser light has a radial frequency ω_0 related to the wave number k:

$$\omega_0 = kc, \tag{8.3}$$

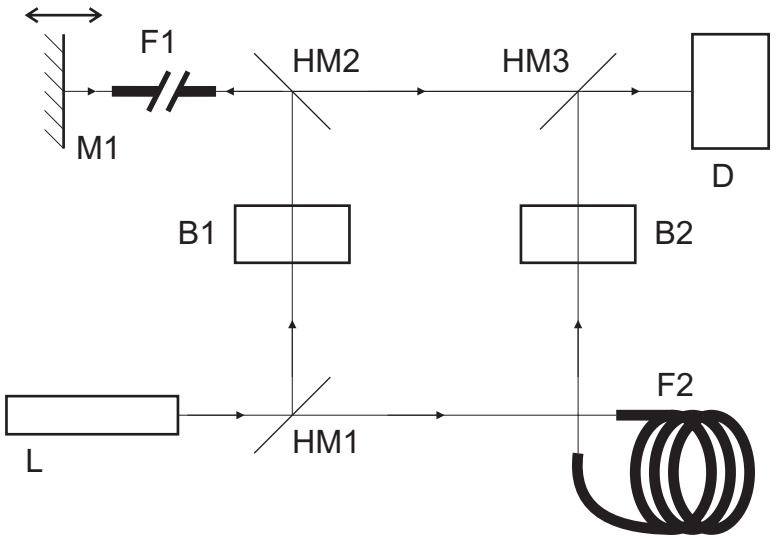

Figure 8.2: The setup for a Mach-Zehnder based interferometer with arms that go through fibers.

where c is the speed of light. Measuring the frequency of the light in a frame that moves with a speed u in the same direction as the laser light, gives

$$\omega = k(c - u). \tag{8.4}$$

If the light is scattered in the opposite direction, from the moving frame back to the reference frame, then the observed frequency in the reference frame is shifted more:

$$\omega = k(c - 2u). \tag{8.5}$$

For a sinusoidally vibrating surface, with the substitution of equations 8.3 and 8.2, the observed instantaneous frequency ω of the laser light is

$$\omega(t) = kc - 2ku = \omega_0 - 2k\omega_M A_M \cos(\omega_M t), \tag{8.6}$$

where

$$2k\omega_M A_M \cos(\omega_M t) = \omega_D \tag{8.7}$$

is the Doppler shift in frequency.

A frequency modulated signal $s(t)$ can in general be written as

$$s(t) = A\cos\big(\omega_0 t + \phi(t)\big) \tag{8.8}$$

where A is constant, and $\phi(t)$ is time-varying. The argument Φ of the cosine is defined as:

$$\Phi(t) = \omega_0 t + \phi(t). \tag{8.9}$$

The instantaneous radian frequency is defined as the time derivative of the argument

$$\omega_i(t) = \frac{\mathrm{d}}{\mathrm{d}t}\Phi(t) = \omega_0 + \frac{\mathrm{d}}{\mathrm{d}t}\phi(t) \tag{8.10}$$

(Fante [1988]).

On the other hand, when the instantaneous frequency ω_i is known, the argument is derived by integrating ω_i:

$$\Phi(t) = \int_0^t \omega_i(\tau)\mathrm{d}\tau. \tag{8.11}$$

For the Doppler shifted frequency (equation 8.6), the argument Φ of a wave is

$$\Phi(t) = \int (\omega_0 - \omega_D)\mathrm{d}t = \omega_0 t - 2kA_M \sin(\omega_M t) + \phi, \tag{8.12}$$

with ϕ the integration constant.

8.3.2 Interferometry

Interferometry requires two monochromatic laser beams, a target beam and a reference beam, with arguments Φ_T and Φ_R (with their own frequencies and phases, as described by equation 8.9), and amplitudes E_{0T} and E_{0R}, respectively. The respective time signals of the target and reference laser beams can be described by plane harmonic waves as:

$$E_T(t) = E_{0T}\sin\Phi_T \tag{8.13}$$

$$E_R(t) = E_{0R}\sin\Phi_R. \tag{8.14}$$

The interfering laser beams produce a current I_D in a detector D with a sensitivity K_D:

$$\begin{aligned} I_D =& K_D[E_{0T}\sin(\Phi_T) + E_{0R}\sin(\Phi_R)]^2 = \\ & \tfrac{1}{2}K_D\Big\{E_{0T}^2 + E_{0R}^2 \\ & - [E_{0T}^2\cos(2\Phi_T) + E_{0R}^2\cos(2\Phi_R)] \\ & - 2E_{0T}E_{0R}\cos(\Phi_T + \Phi_R) \\ & + 2E_{0T}E_{0R}\cos(\Phi_T - \Phi_R)\Big\}. \end{aligned} \tag{8.15}$$

Working out the arguments Φ, the detector current is

$$\begin{aligned} I_D = \tfrac{1}{2}K_D\Big\{& E_{0T}^2 + E_{0R}^2 \\ & - [E_{0T}^2\cos 2(\omega_T t + \phi_T) + E_{0R}^2\cos 2(\omega_R t + \phi_R)] \\ & - 2E_{0T}E_{0R}\cos\left[(\omega_T + \omega_R)t + (\phi_T + \phi_R)\right] \\ & + 2E_{0T}E_{0R}\cos\left[(\omega_T - \omega_R)t + (\phi_T - \phi_R)\right]\Big\}. \end{aligned} \tag{8.16}$$

In equation 8.16, there are basically 5 terms with different frequencies. The DC term consists of $E_{0T}^2 + E_{0R}^2$, then there are terms with frequencies $2\omega_T$, $2\omega_R$, and their mean $\omega_T + \omega_R$. The last term comprises the difference frequency $\omega_T - \omega_R$. Band-pass filtering this signal leaves

$$I_D = K_D E_{0T} E_{0R} \cos(\Phi_T - \Phi_R). \tag{8.17}$$

In practice, this means that if the frequencies are identical, then the intensity on the detector is constant. The term in equation 8.17 then contributes to the DC term. Having two slightly different frequencies, however, results in an intensity on the detector that is fluctuating with an angular frequency of $\omega_T - \omega_R$. A graphical representation of this is given in figure 8.3.

Now, let the target beam be backscattered from the reflecting vibrating surface. The argument Φ_T (equation 8.12) then is

$$\Phi_T = \omega_T t - 2kA_M \sin(\omega_M t) + \phi_T. \tag{8.18}$$

The argument Φ_R of the reference beam is not frequency modulated, hence, equation 8.11 therefore yields

$$\Phi_R = \omega_R t + \phi_R. \tag{8.19}$$

Substitution of equations 8.18 and 8.19 into equation 8.17 leads to

$$I_D = K_D E_{0T} E_{0R} \cos\left[(\omega_T - \omega_R)t - 2kA_M \sin(\omega_M t) + (\phi_T - \phi_R)\right]. \tag{8.20}$$

This is a frequency or a phase modulated signal, of which the argument of the cosine in given in equation 8.20. With a frequency tracker, the phase modulations can be detected. The output of the frequency tracker is proportional to the instantaneous frequency of the detector current (equation 8.10), in this case

$$\omega_i = \omega_T - \omega_R - 2k\omega_M A_M \cos(\omega_M t). \tag{8.21}$$

The frequency $\omega_T - \omega_R$ is constant, and the AC part of equation 8.21 gives, apart from some constants, the speed of the vibrating surface u (equation 8.2). The AC output of the tracker therefore is:

$$V_{\text{out}} = -2Kku, \tag{8.22}$$

where K is the sensitivity of the frequency tracker. The unit of K is Volts/Hz (van Netten [1988]). Note that V_{out} is the response to the instantaneous speed, and that the frequency of the vibrating surface is the frequency of the voltage.

In this section, u is assumed to be sinusoidal. The system is linear so that, without loss of generality, u can be replaced throughout this section by a nonstationary signal.

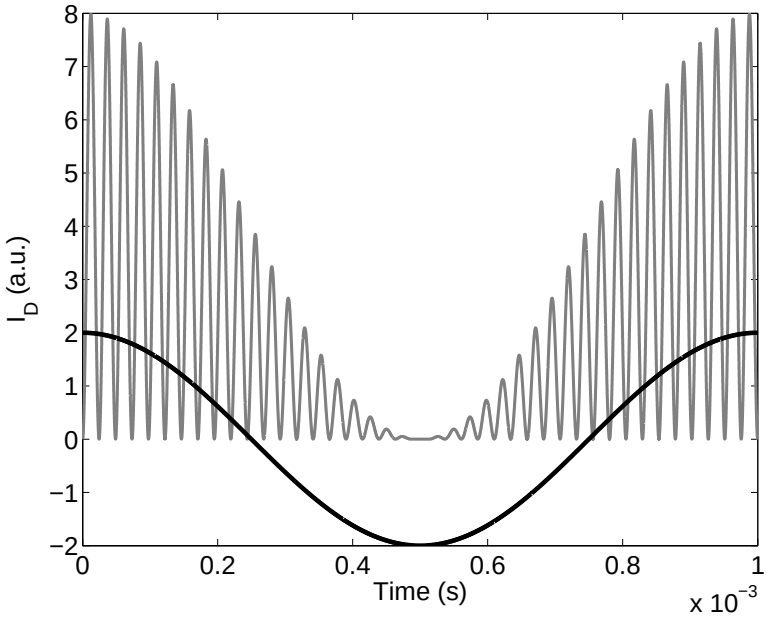

Figure 8.3: Detector current I_D. Two interfering laser beams ($f_T = 21000$ Hz, $f_R = 20000$ Hz) produce a detector current in the detector. The grey line represents equation 8.16. The black line is the band-pass filtered signal from equation 8.17. The period of the black line is 1 ms, which corresponds to the difference frequency $f_T - f_R$, being 1000 Hz.

8.3.3 Measured vibrational data

With laser Doppler interferometry, the vibrating surface speed u can be found. The time signal coming from the demodulator is a measure for this u. Equation 3.2 shows that the root-mean-square value of u is proportional to the rms sound pressure immediately near the surface. With these data from the complete surface, the complete sound field can be modelled (Yao *et al.* [2004]).

8.4 Optical considerations

The use of fibers pose some specific problems. Fibers consist of a core (index of refraction n_1) which is surrounded by a cladding layer (index of refraction n_2), and a protective surround. Through internal reflections, the light stays inside the core. These internal reflections occur when the angle of incidence on the core-cladding boundary is greater than the critical angle $i_B = \sin^{-1} n$, where $n = n_2/n_1$. From figure 8.4, it can be seen that this poses a limitation on the angle incident to the fiber ending. This is called the acceptance angle, which is the inverse sine

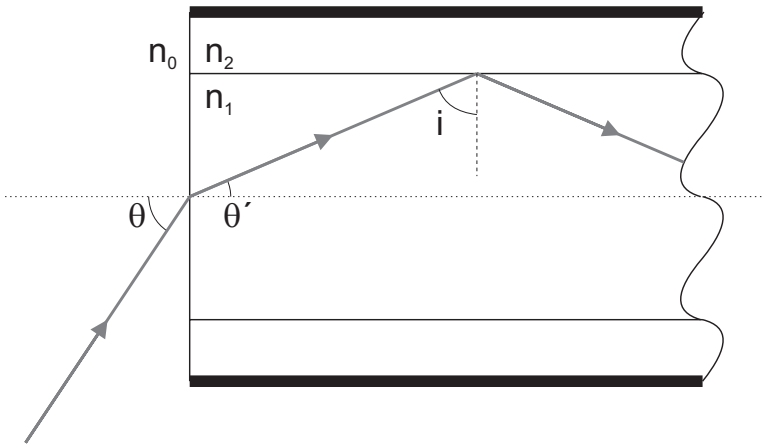

Figure 8.4: Schematic view of a fiber. If i is equal to the critical angle, then θ is the acceptance angle of the fiber. In this graph $n_0 \sin\theta = n_1 \sin\theta' = n_1 \cos i$ $(n_1 > n_2 > n_0)$.

of the numerical aperture (NA) of the fiber: $\sin^{-1} \mathrm{NA} = i_A$. For a good collection efficiency, all light coming from the source should be focused within a cone, having a half top-angle i_A. All energy outside this cone is not coupled into the fiber. For an incoming parallel bundle, with a bundle diameter equal to the lens diameter, this means that the objective lens must have a numerical aperture smaller than or equal to that of the fiber. The size of the fiber core can result in different modes of the light transmitted by the fiber. Through consecutive internal reflections, the optical path lengths of different rays may vary considerable. Destructive self-interference upon leaving the fiber degrades the beam quality, and makes it less suitable for interference experiments. By reducing the core diameter, only one mode is guided by the fiber. This is called the TEM_{00} (transverse electro-magnetic) mode.

In general, the manufacturer of the fiber provides objective lenses and mounting devices that fulfill all requirements. Nevertheless, the laser beam must enter the lens and fiber straight. This is of particular importance with a monomode or single-mode fiber, where the core diameter is typically 5 μm. Bringing the beam diameter back from a millimeter to this spot size requires high grade optics. The beam has a certain divergence and is therefore not completely parallel. Not all rays meet at the focal point which should be at the fiber entrance. The increased spot size leads to a reduced coupling efficiency, and also to scattered light back from the fiber entrance into the setup. The divergence depends on the beam diameter, thus a wider diameter conserves the parallel beam better. A beam diameter greater than the lens diameter is undesirable.

For a free laser beam, it is also true that a wider beam gives a less diverging beam waist. In experiments done with free beams, a wide beam should be employed to

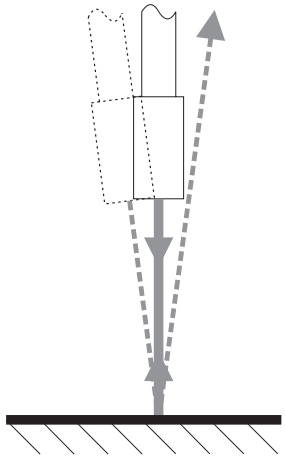

Figure 8.5: Two measurement situations with fibers. The angle of incidence to the scanner surface of the laser beam must be 90°. Full lines: the laser beam reflects from the surface and enters the fiber again. Dotted lines: the angle of the fiber end to the surface is not perpendicular. In the worst case, the laser light does not enter the fiber again.

minimize the divergence and the loss of intensity because of that (Young [2000]).

8.5 Practical considerations

Regardless the method, free beam or fiber, the laser beam must be aligned in such a way that, after scattering, it is reflected back in the same direction. For the free beam, deviations from this alignment result in the beam not returning via the same path. The returning beam must be combined at HM3 with the reference beam. A deviating beam is harder to be made parallel and overlapping. For the fiber, misalignment yields coupling inefficiency, or in the worst case, no light returning into the fiber at all (figure 8.5). The alignment must be done precise, and possibly with a certain ease. The fiber end must be placed in an adjustable lever, which can be adjusted as the MR outer surfaces are curved, and not necessarily symmetric. Within the bore, the lever is difficult to reach, therefore the ease of adjusting is an important factor during operation. For the free beam, a similar argumentation holds. The mirror that deflects the laser beam to the surface, should also be easy adjustable (figure 8.6). The tolerances in misalignment are small, as the beam diameter, or the spot size, are small as well. Producing a diverging beam increases this tolerance, as light is more likely to leave the fiber, scatter perpendicular at the surface, and re-enter the fiber in such a setup (figure 8.7). The loss of intensity, however, is considerable.

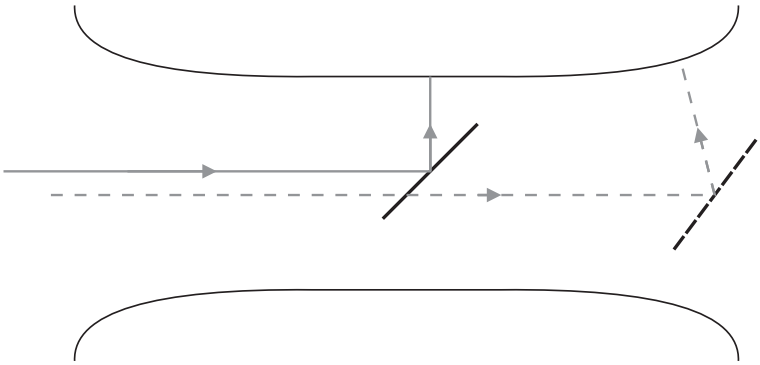

Figure 8.6: Two measurement situations with mirrors. The angle of incidence to the scanner surface of the laser beam must be 90°. Full lines: the mirror is under an angle of 45°, and the laser beam is parallel to the scanner surface under investigation. Dotted lines: the laser beam has a smaller angle of incidence to the mirror, as the scanner surface is curved.

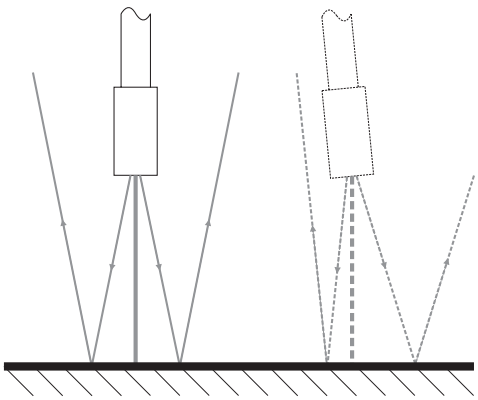

Figure 8.7: With a diverging beam, the reflected laser light can enter the fiber again. The angle with the normal must be smaller than half the top-angle of the beam emerging from the fiber. The thicker lines are perpendicular to the surface, and correspond to the light that is scattered back into the fiber.

In both the fiber setup and the mirror setup, the instrumentation within the scanner room, or at least in the vicinity of the bore, cannot be magnetic nor conducting. The vibrations to measure arise from the switching of gradient magnetic fields. These same fields can induce eddy currents in conductors, which then evoke Lorentz forces in the conductors. The resulting vibrations lead to a disturbance of the measurements.

Vibrations can be transferred from the scanner to the measurement setup. For adequate measurements, such transfer should be prevented. The mounting of the measurement system must be isolated from the scanner system as much as possible. Airborne vibrations, the acoustic noise, can also induce vibrations in the measurement system. Resonance frequencies of the construction must lie outside the frequency range of testing. Furthermore, the interferometry setup must be located outside the sound field. The components in such a setup are small and sensitive to vibrations. Speech in the vicinity of the interferometry setup is already quite noticeable.

Deflection of the scattered light due to the surface vibrations can be neglected. A 1000 Hz signal at 130 dB SPL leads to 2.4×10^{-5} m rms amplitude (at standard temperature and pressure). Under the assumption that this value does not change significantly over the spot area, no significant deflections are generated. If at all, these are $\ll 1$ degree, and be of influence only if the free beam path is long. In any case, the alignment must be perpendicular to the surface.

8.6 Problems/restrictions

8.6.1 Placement and alignment

The scanner surface looks like a cylinder, but is in fact not. It is in general not rotational symmetric, and has a curved surface in the Z-direction (figure 8.6). A construction for free beam experiments as used by Yao *et al.* [2004] is not therefore feasible in a real scanner environment. The rotation of the mirror is necessary to direct the beam in another direction. For alignment purposes, the mirror needs to be translated in the XY plane as well (see figure 8.8). In experimental setups containing fibers, the fiber end must be guided to the scanner surface. The fiber-head place keeper can be mounted on a rotating device, also to scan the surface all round. The place keeper must give enough directional freedom to align the laser beam perpendicular to the surface (figure 8.9). Especially the fiber end must have rotational freedom for alignment purposes.

If possible, the measurements ought to be performed with a subject or dummy inside the scanner bore. The sound field may depend on the volume it radiates into, with the scanner bore design as a crucial factor (Hedeen and Edelstein [1997]; Kuijpers [1999]; Price *et al.* [2001]). Further, loading the bed and perhaps the scanner

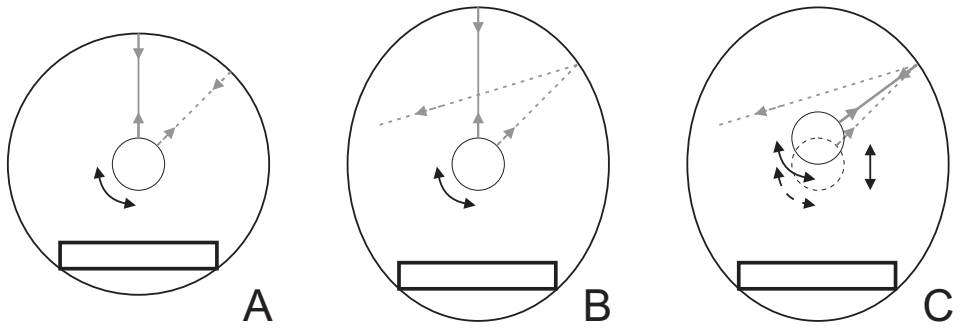

Figure 8.8: The scanner bore in cross section. The central circle depicts the rotating mirror holder. A: With a rotational symmetric bore, the mirror holder only needs to rotate for measurements. B: If the bore is not rotational symmetric, then only rotating the mirror leads to light scattered round (dotted lines). C: To avoid situation B (dotted lines), the mirror holder needs translational freedom in the XY plane as well, to be placed in the correct position (solid lines).

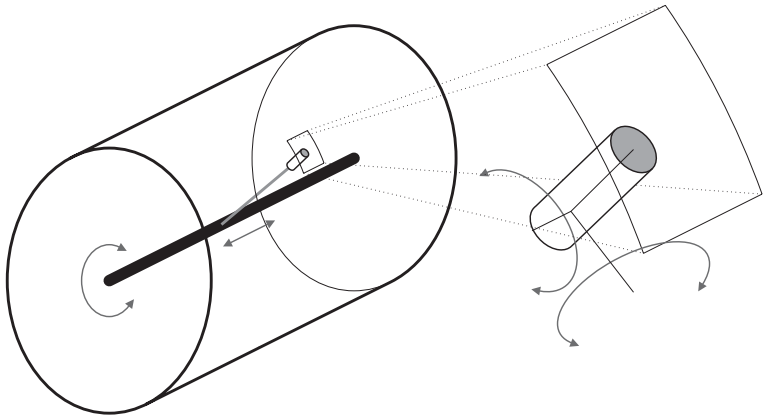

Figure 8.9: The scanner bore is depicted in thick black lines. The central thick black line represents the mounting of the fiber place keeper to the floor. From the small cylinder to the thick black line is a grey line, this represents the connection from the fiber end (small cylinder) to the floor mount. All arrows indicate the rotations and translations that are necessary in a setup with fibers.

bore with extra mass, may alter the vibrational characteristics. The laser interferometric setup should not interfere with the scanner sound field, nor the vibrational characteristics. This poses serious restrictions to the size and construction of such a setup.

The complete measurement setup should be supported by the floor, and not touch the vibrating scanner. Still, it has to be placed in such a way, that the mirror or fiber end can be located accurately in the scanner bore, or near the scanner wall.

8.6.2 Limits of LDI

Laser Doppler interferometry in a setup as presented is capable of detecting nanometer displacements (van Netten [1988]). For sinusoidal vibrations with a constant amplitude, the velocity depends linearly on the frequency (equation 8.2). Low frequency, low amplitude signals give a low V_{out}. Irrespective of frequency, the demodulator gives an output depending on the measured velocity. The sensitivity of the demodulator, however, limits the maximum velocity to be measured. The background noise inside the scanner bore are more than 50 dB(A). It is not clear whether this is due to scanner induced vibrations, and that the scanner surface vibrates with corresponding velocities. It does however provide a lower limit to the measurement values of interest. This, in combination with the knowledge about the highest measured sound pressure levels (138 dB peak level in Ravicz *et al.* [2000]), determine the required demodulator sensitivity and recording resolution.

The output signal of the demodulator is not depending on the intensity of the photo signal on the detector. The detector current, however, depends on the intensities of both the target beam and the reference beam (equation 8.20). For a detector current with enough signal-to-noise, the intensity of the reference beam should be as high as possible. The backscattered signal with intensity E_{0T} can then be low, without compromising measurements. There is a lower limit to E_{0T}, the literature however does not state the minimally required ratio of E_{0T} and E_{0R}. During measurements, the noise floor of the demodulator needs to be taken into account. If the signal-to-noise ratio of the demodulator input signal is too low for the demodulator to function properly, the detector current signal needs amplification.

Related to the backscattered signal intensity is the reflectivity of the vibrating surface. Absorption and diffuse scatter of incoming beam decrease the intensity of the reflected beam. The use of a mirror, glued to the surface, or retroreflective tape, can reduce this problem. The increase of mass can be so low that the vibrational characteristics are not altered. Joining the mirror to the surface together must be done tight. A layer of glue can lead to resonance frequencies of the mirror.

In addition, the measurement time is a serious constraint in such experiments. The actual measurement is not the limiting factor. Relocating and aligning the setup may be time consuming. A high number of measurement points is needed for ac-

curate sound pressure level prediction. The spacing of points depends on the wavelength of the vibrations. Without considering harmonics, the minimum wavelength in air is about 10 cm. Spacing measurement points 2.5 cm apart in a bore (diameter 60 cm, length 150 cm), leads to 4500 separate measurements. Automation of this process would require electronics to navigate the mirror or the fiber place keeper. Electronics are in general not compatible with strong magnetic fields.

8.7 Conclusion

In this chapter, the considerations that need to be taken in laser Doppler interferometry of the scanner bore surface are discussed. The advance of LDI is contact-free measurement of vibrations. Both free-beam and fiber setups are possible, with their shortcomings and advantages. Fibers give a better beam preservation, and give a higher freedom to lead the laser beam to the scanner surface. Free beams need a less complicated construction for placement inside the scanner bore, but leading the beam into the bore might lead to difficulties.

The most serious constraint of LDI measurements inside the scanner bore, is time. In a laboratory setup, the alignment is already difficult. In a setup that changes after every measurement, the alignment takes considerable time of the total measurement time. Automation is difficult, if not impossible. The number of measurement points with a piezoelectric transducer is equal to that with LDI, just like the time to move to a new measurement location. However, the gain in time comes from the alignment procedure. The LDI experiment should be done in combination with piezoelectric transducers. Comparing the results from such an experiment will make clear which measurement system should be chosen.

Chapter 9

Conclusion

9.1 Summary and conclusions

Magnetic Resonance Imaging is an outstanding modern technique and a powerful tool in brain research. It comes, however, with some problematic technical properties. A strong magnetic field and the use of RF signals prevent its use for certain persons, *e.g.*, because of pacemakers or tattoos. The use of strong electric currents within the static magnetic field of the scanner leads to Lorentz forces acting on the scanner housing. In particular, the alternating currents generate alternating forces which induce scanner vibrations in the audio-frequency range. In other words, these resulting vibrations are the source of the loud acoustic noise that accompanies MRI scanning. Subjects examined in MRI report that this noise is one of the main causes of discomfort. Chapter 5 presents an overview of the acoustic noise effects. It also discusses the evoked physiological effects, which pose limits on the use of MRI for functional brain research. These effects include general annoyance, distraction from tasks, and can results in a reduction of brain activation. Obviously, the high sound pressure levels generated in MRI, and in particular fMRI (up to more than 110 dB(A)), imply that MR examination should be performed only on subjects wearing proper hearing protection.

All studies on MRI sound production indicate the necessity to reduce the generation of acoustic noise during (functional) magnetic resonance imaging. Sound reducing methods are found in hardware modifications of the scanner. A combination of several approaches may lead to substantial reduction of the acoustic noise. Additional reduction of the noise can be achieved by the design of the scanner gradient currents, i.e., in a software design approach. The vibration of the gradient coils is due to these gradients currents. Avoiding resonance frequencies of the gradient coil structure and/or the MRI scanner, leads to a decrease of the generated acoustic noise.

The resonance frequencies of the scanner are determined experimentally, by

measurement of the acoustic transfer function of the MRI scanner. This function relates the generated sound wave to the driving current. In general, this provides the tools with which the response can be predicted. However, some practical complications arise. The output spectra obtained for flat input spectra contain relatively narrow troughs for which the standard procedures produce ambiguous results. This ambiguity appears to be largely due to harmonic distortion and other background noise. In section 3.5, a sound pressure transfer function is proposed that takes these two factors into account. Other methods, such as the noise response and the pulse response, do not take these factors into account (chapter 7).

In chapters 6 and 7 the sound pressure transfer function is applied, in combination with frequency sweep signals. With these signals, the frequencies of interest are presented consecutively, and not simultaneously as with the other methods. This means that the harmonic distortion and noise can be dealt with properly. The limitations of frequency sweep signals, *e.g.*, the sweep rate, are discussed. The sound pressure transfer function shows the best agreement over sweep rates. With respect to input signal amplitudes, however, there are differences that are caused by nonlinearities in the amplitude responses. The sound pressure transfer functions also show the limits of the attenuation that can be achieved by redesigning gradient currents.

Chapter 8 presents a discussion of laser Doppler interferometry measurements of scanner vibrations. These vibrations vary over the surface of the scanner bore, and over the surface of the scanner. Laser Doppler interferometry appears to be a promising technique to perform vibration measurements and to establish the vibration patterns. It should be noted that this method requires precise and elaborate alignment of laser beams and a high number of test points.

9.2 Perspectives

The longer measurement times for frequency sweep signals, can be reduced by decreasing the averaging window with increasing frequency. Averaging should take place over a number of periods of the periodic signal, and not necessarily over 125 ms.

In the literature dealing with acoustics of fMRI, the measurements of the acoustic transfer functions are made without subjects inside the scanner bore. The presence of a subject changes the sound field (Hedeen and Edelstein [1997]; Price *et al.* [2001]). This leads to a change in perceived sound pressure level, and should thus be taken into account.

The auditory frequency sensitivity is level dependent. Therefore, the use of the A-weighting scale is less useful for high sound pressure levels. The use of a loudness scale should be preferred over a sound pressure scale. The loudness can be calculated from the sound pressure levels, when measured in third octave bands. With a loudness matching task, the loudness transfer can be determined directly.

Such a loudness transfer function accounts for all sound and vibration conduction pathways.

Appendix A

Acquisition

A.1 Acquisition program

The acquisition program as mentioned in chapter 4 consist of three parts: the control program, the actual acquisition program, and the trigger program. In figure A.1, the flowchart for the three cooperating programs is presented. Here the functionality of the separate programs is enclosed within the thick black lines.

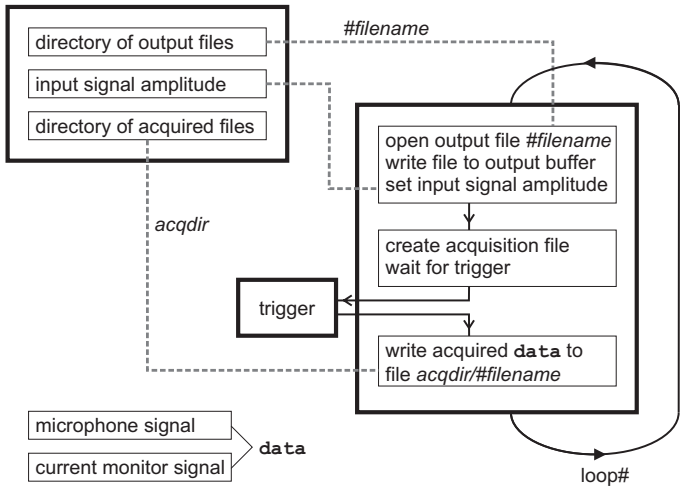

Figure A.1: Flow chart of the acquisition programs. See text for details.

The files containing the signals are made with a MATLAB program, and saved as 16-bit integer files in the directory of output files. The control program needs three inputs: the directory path of the output files, the required signal amplitude, and the directory path where the acquired files are stored (*acqdir*). After filling out these

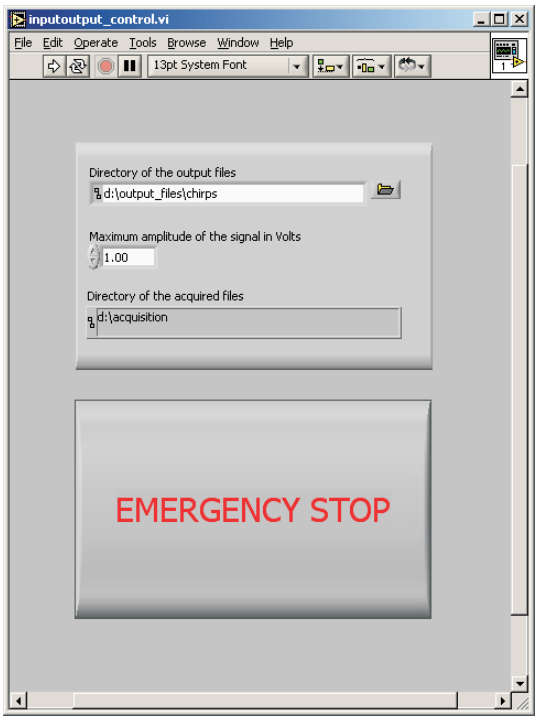

Figure A.2: The appearance of the LabVIEW control program. The necessary data has to be filled in at the appropriate location.

data in the corresponding fields (figure A.2), the program is started and these data are transferred to the acquisition program.

The acquisition program is adapted from the existing LabVIEW *Cont Acq to File (binary).vi* program. A trigger program is integrated in the acquisition program to start the output of the signal at the same time as the acquisition. The acquisition program is placed in a loop, which runs as many times as there are output files. Within one loop (*loop#*), the program opens one of the output files (*#filename*), and write the (normalized) contents, multiplied with the desired signal amplitude, to the buffer of the acquisition board. The next step before acquisition, is the creation of a file into which the acquired data is written. This file has the same name as the output file *#filename*. Before storing acquired data, all the settings of the board and the channels are stored in the file header.

When all parameters are set, and the program is ready to start acquisition, a window pops up. By pushing a button, a digital trigger is given to the acquisition board, and the output of the signal starts, together with the acquisition of the current monitor signal and the microphone signal. After the trigger is given, the trigger window closes again.

In the window of the acquisition program (figure A.3), the course of acquisition can be followed. The acquisition within one loop stops as the end of the output file is reached. The program stops after completing the loop. In the case the output needs to be stopped during a run, the emergency stop button (figure A.2) can be clicked. All output and acquisition stops immediately.

A.2 Acquisition hardware

As measurements would take place at at least two locations in different cities, the acquisition hardware had to be transportable. A HP Compaq Evo Desktop d500 series computer (H $\times$ W $\times$ D = 10 $\times$ 34 $\times$ 38 cm), with room for a PCI card, was purchased. This computer fitted in a suitcase together with the Brüel & Kjær 2260 Investigator and some additional hardware (break-out box, adapter, cables). The KEMO filter and a keyboard and mouse were transported in separate bag. The combined weight can be carried over not too long distances.

The National Instruments PCI/PXI-6052E card, for the recording of the analog signals, was chosen as it was one of the few digital acquisition boards that could simultaneously record 5 channels at hi-fi audio quality (16-bit resolution, sampling rate of 44.1 kHz or higher), with an input range that matched signals coming from the MR scanner.

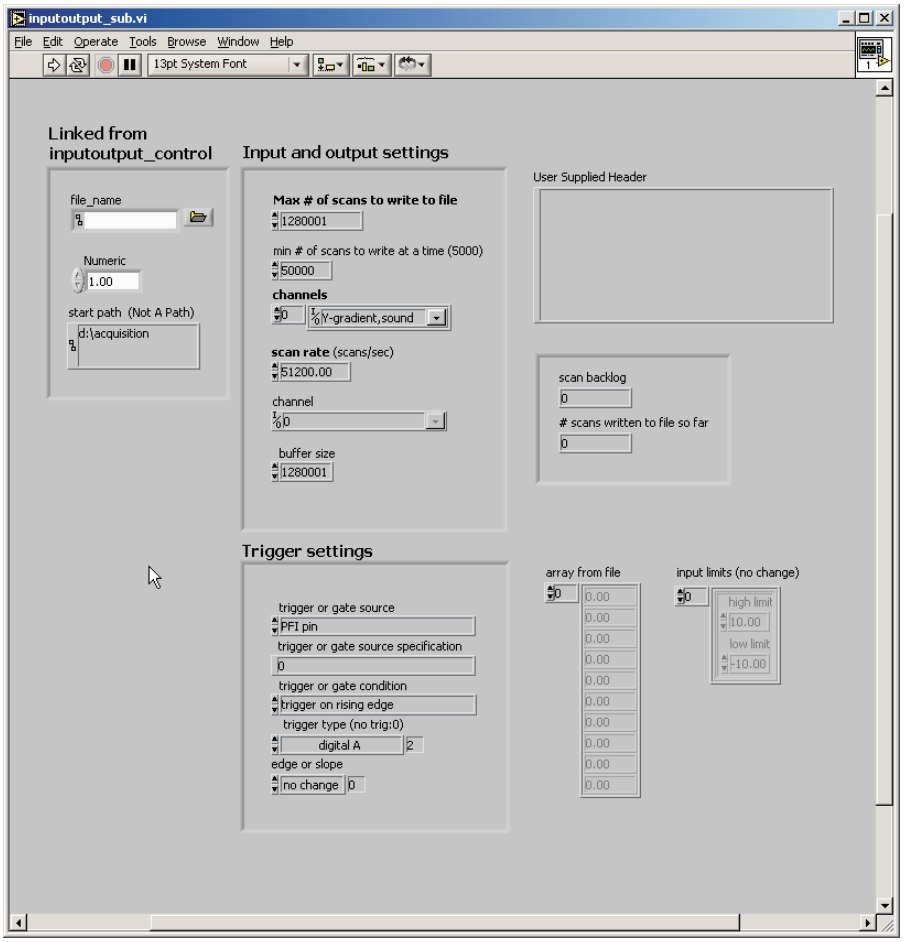

Figure A.3: The appearance of the LabVIEW actual acquisition program. The data from the control program is linked to the upper left panel. Settings that are constant during one run are in the other panels.

Appendix B

Mathematical derivations

B.1 Fourier transform of frequency sweep signal

The known Fourier transforms are:

$$\begin{aligned}\mathcal{F}\{\cos(\omega_0 t)\} &= \sqrt{\frac{\pi}{2}}\big(\delta(\omega-\omega_0)+\delta(\omega+\omega_0)\big)\\ \mathcal{F}\{\sin(\omega_0 t)\} &= \imath\sqrt{\frac{\pi}{2}}\big(\delta(\omega-\omega_0)-\delta(\omega+\omega_0)\big)\end{aligned} \tag{B.1}$$

$$\begin{aligned}\mathcal{F}\{\cos(\beta t^2)\} &= \frac{1}{\sqrt{4\beta}}\big(\cos[\frac{\omega^2}{4\beta}]+\sin[\frac{\omega^2}{4\beta}]\big)\\ \mathcal{F}\{\sin(\beta t^2)\} &= \frac{1}{\sqrt{4\beta}}\big(\cos[\frac{\omega^2}{4\beta}]-\sin[\frac{\omega^2}{4\beta}]\big).\end{aligned} \tag{B.2}$$

Using the trigonometric expansion for formula 3.12 yields:

$$\begin{aligned}&\mathcal{F}\{\cos\big((\omega_0+\beta t)t\big)\}=\\ &\mathcal{F}\{\cos(\omega_0 t+\beta t^2)\}=\\ &\mathcal{F}\{\cos(\omega_0 t)\cos(\beta t^2)-\sin(\omega_0 t)\sin(\beta t^2)\}=\\ &\mathcal{F}\{\cos(\omega_0 t)\cos(\beta t^2)\}-\mathcal{F}\{\sin(\omega_0 t)\sin(\beta t^2)\}=\\ &\mathcal{F}\{\cos(\omega_0 t)\}*\mathcal{F}\{\cos(\beta t^2)\}-\mathcal{F}\{\sin(\omega_0 t)\}*\mathcal{F}\{\sin(\beta t^2)\}.\end{aligned} \tag{B.3}$$

Replacing the separate terms in equation B.3 with those from equations B.1 and B.2, and working out the convolutions, results in:

$$\begin{aligned}&\mathcal{F}\big(\cos\big((\omega_0+\beta t)t\big)\big)=\\ &\frac{1}{4\sqrt{\beta}}\Bigg\{(1-\imath)\cos\left(\frac{(\omega-\omega_0)^2}{4\beta}\right)+(1+\imath)\sin\left(\frac{(\omega-\omega_0)^2}{4\beta}\right)+\\ &\qquad(1+\imath)\cos\left(\frac{(\omega+\omega_0)^2}{4\beta}\right)+(1-\imath)\sin\left(\frac{(\omega+\omega_0)^2}{4\beta}\right)\Bigg\}.\end{aligned} \tag{B.4}$$

Taking the Fourier transform of equation B.4 convolved with a rectangular window between $T_c - T$ and $T_c + T$ leads, according to Mathematica 5.0 (Wolfram Research, Inc.), to:

$$\begin{aligned}
&\int_{T_c-T}^{T_c+T} \cos\big((\omega_c+\beta t)t\big)e^{-\imath\omega t}\mathrm{d}t = \\
&\quad \frac{1}{\sqrt{\beta}}\Bigg\{(\frac{1}{4}+\frac{\imath}{4})\sqrt{\frac{\pi}{2}}\Bigg(\imath\cos\left[\frac{(\omega-\omega_c)^2}{4\beta}\right]+\sin\left[\frac{(\omega-\omega_c)^2}{4\beta}\right]\Bigg)\times \\
&\quad \Bigg[\mathrm{erfi}\left[\frac{(\frac{1}{2}+\frac{\imath}{2})\big(2\beta(T_c-T)-(\omega-\omega_c)\big)}{\sqrt{2\beta}}\right]- \\
&\quad \mathrm{erfi}\left[\frac{(\frac{1}{2}+\frac{\imath}{2})\big(2\beta(T_c+T)-(\omega-\omega_c)\big)}{\sqrt{2\beta}}\right]+ \\
&\quad \left(\cos\left[\frac{\omega^2+\omega_c^2}{2\beta}\right]+\imath\sin\left[\frac{\omega^2+\omega_c^2}{2\beta}\right]\right)\times \\
&\quad \left(\mathrm{erf}\left[\frac{(\frac{1}{2}+\frac{\imath}{2})\big(2\beta(T_c-T)+(\omega+\omega_c)\big)}{\sqrt{2\beta}}\right]- \right. \\
&\quad \left.\mathrm{erf}\left[\frac{(\frac{1}{2}+\frac{\imath}{2})\big(2\beta(T_c+T)+(\omega+\omega_c)\big)}{\sqrt{2\beta}}\right]\right)\Bigg]\Bigg\},
\end{aligned} \tag{B.5}$$

where ω_c is the frequency at T_c. This is graphically depicted in figure 4.2, panels A and B. The results of multiplying the time signal with a Kaiser-Bessel window are in panels C through F. These graphs are obtained with Digital Fourier Transforms in Matlab (The MathWorks, Inc.).

B.2 Noise cancellation

The addition of two sinusoidal signals in opposite phase may lead to cancellation. This principle is used in active noise cancellation (section 5.4.2). The remaining signal s is:

$$\begin{aligned}
s &= a_1\sin(\omega t) - (a_1+\delta a)\sin(\omega t+\delta\phi) \\
&= -(a_1+\delta a)\big[\sin(\omega t)\cos(\delta\phi)+\cos(\omega t)\sin(\delta\phi)\big]+a_1\sin(\omega t).
\end{aligned} \tag{B.6}$$

With perfect phase matching ($\delta\phi = 0$), the remaining signal $s = -d\sin(\omega t)$, and for perfect amplitude matching ($\delta a = 0$),

$$s = -a_1\big[\sin(\omega t)\cos(\delta\phi)+\cos(\omega t)\sin(\delta\phi)\big]+a_1\sin(\omega t). \tag{B.7}$$

This can be approximated by

$$s = -a_1\delta\phi\cos(\omega t), \tag{B.8}$$

when $\delta\phi$ is small.

Bibliography

E. Amaro, Jr., S.C. Williams, S.S. Shergill, C.H. Fu, M. MacSweeney, M.M. Picchioni, M.J. Brammer, and P.K. McGuire. Acoustic noise and functional magnetic resonance imaging: current strategies and future prospects. *J.Magn Reson.Imaging*, 16:497–510, 2002.

ANSI S1.13-1995. American National Standards Institute, R1999.

G. Aurilio, A. Cavallo, L. Lecce, E. Monaco, L. Napolitano, and C. Natale. Fuselage frame vibration control using magnetostrictive hybrid dynamic vibration absorbers. *Fith European Conference on Noise Control, Naples, Italy, 19-21 May*, Paper ID: 227, 2003.

P.A. Bandettini, A. Jesmanowicz, J. Van Kylen, R.M. Birn, and J.S. Hyde. Functional MRI of brain activation induced by scanner acoustic noise. *Magn Reson.Med.*, 39: 410–416, 1998.

M.F. Barnothy, editor. *Biological effects of magnetic fields*. Plenum Press, New York, 1964.

L. Barrett. It's so noisy, you can't think straight. *Trends Cogn Sci.*, 6:197, 2002.

P. Belin, R.J. Zatorre, R. Hoge, A.C. Evans, and B. Pike. Event-related fMRI of the auditory cortex. *Neuroimage*, 10:417–429, 1999.

E.H. Berger, J.R. Franks, A. Behar, J.G. Casali, C. Dixon-Ernst, R.W. Kieper, C.J. Merry, B.T. Mozo, C.W. Nixon, D. Ohlin, J.D. Royster, and L.H. Royster. Development of a new standard laboratory protocol for estimating the field attenuation of hearing protection devices. Part III. The validity of using subject-fit data. *J.Acoust.Soc.Am.*, 103:665–672, 1998.

E.H. Berger and J.E. Kerivan. Influence of physiological noise and the occlusion effect on the measurement of real-ear attenuation at threshold. *J.Acoust.Soc.Am.*, 74:81–94, 1983.

E.H. Berger, R.W. Kieper, and D. Gauger. Hearing protection: surpassing the limits to attenuation imposed by the bone-conduction pathways. *J.Acoust.Soc.Am.*, 114:

1955–1967, 2003.

D. Bilecen, E.W. Radu, and K. Scheffler. The MR tomograph as a sound generator: fMRI tool for the investigation of the auditory cortex. *Magn Reson.Med.*, 40:934–937, 1998.

A. Brechmann, F. Baumgart, and H. Scheich. Sound-level-dependent representation of frequency modulations in human auditory cortex: a low-noise fMRI study. *J.Neurophysiol.*, 87:423–433, 2002.

S.C. Brennan, W.H. Redd, P.B. Jacobsen, O. Schorr, R.T. Heelan, G.K. Sze, G. Krol, B.E. Peters, and J.K. Morrissey. Anxiety and panic during magnetic resonance scans. *Lancet*, 2:512, 1988.

R.W. Brown, Y.C. Cheng, T.P. Eagan, T.K. Kidane, H. Mathur, R.G. Petschek, W.G. Sherwin, S.M. Shvartsman, and J.D. Willig. Toward shielding improvements in MRI gradients and other systems. *MAGMA.*, 13:186–192, 2002.

R.E. Brummett, J.M. Talbot, and P. Charuhas. Potential hearing loss resulting from MR imaging. *Radiology*, 169:539–540, 1988.

J.G. Casali and E.H. Berger. Technology advancements in hearing protection circa 1995: active noise reduction, frequency/amplitude-sensitivity, and uniform attenuation. *Am.Ind.Hyg.Assoc.J.*, 57:175–185, 1996.

J. Chambers, M.A. Akeroyd, A.Q. Summerfield, and A.R. Palmer. Active control of the volume acquisition noise in functional magnetic resonance imaging: method and psychoacoustical evaluation. *J.Acoust.Soc.Am.*, 110:3041–3054, 2001.

B.L.W. Chapman, B. Haywood, and P. Mansfield. Optimized gradient pulse for use with EPI employing active acoustic control. *Magnetic Resonance in Medicine*, 50: 931–935, 2003.

B.L.W. Chapman and P. Mansfield. A quiet gradient-coil set employing optimized, force-shielded, distributed coil designs. *Journal of Magnetic Resonance Series B*, 107:152–157, 1995.

Z.H. Cho, S.C. Chung, D.W. Lim, and E.K. Wong. Effects of the acoustic noise of the gradient systems on fMRI: A study on auditory, motor, and visual cortices. *Magnetic Resonance in Medicine*, 39:331–335, 1998a.

Z.H. Cho, S.T. Chung, J.Y. Chung, S.H. Park, J.S. Kim, C.H. Moon, and I.K. Hong. A new silent magnetic resonance imaging using a rotating DC gradient. *Magn Reson.Med.*, 39:317–321, 1998b.

Z.H. Cho, S.H. Park, J.H. Kim, S.C. Chung, S.T. Chung, J.Y. Chung, C.W. Moon, J.H. Yi, C.H. Sin, and E.K. Wong. Analysis of acoustic noise in MRI. *Magn Reson.Imaging*, 15:815–822, 1997.

S.A. Counter, A. Olofsson, E. Borg, B. Bjelke, A. Haggstrom, and H.F. Grahn. Analysis of magnetic resonance imaging acoustic noise generated by a 4.7 T experimental system. *Acta Otolaryngol.*, 120:739–743, 2000.

J.A. de Zwart, P. van Gelderen, P. Kellman, and J.H. Duyn. Reduction of gradient acoustic noise in MRI using SENSE-EPI. *Neuroimage.*, 16:1151–1155, 2002.

G. DeMeester, M. Morich, A. Byrne, F. Davies, D. Melotte, and A. Thomas. Challenges of short magnet design. *MAGMA.*, 13:193–198, 2002.

F. Di Salle, F. Esposito, T. Scarabino, E. Formisano, E. Marciano, C. Saulino, S. Cirillo, R. Elefante, K. Scheffler, and E. Seifritz. fMRI of the auditory system: understanding the neural basis of auditory gestalt. *Magn Reson.Imaging*, 21:1213–1224, 2003.

F. Di Salle, E. Formisano, E. Seifritz, D.E.J. Linden, K. Scheffler, C. Saulino, G. Tedeschi, F.E. Zanella, A. Pepino, R. Goebel, and E. Marciano. Functional fields in human auditory cortex revealed by time-resolved fMRI without interference of EPI noise. *Neuroimage*, 13:328–338, 2001.

W.A. Edelstein, R.A. Hedeen, R.P. Mallozzi, S.A. El Hamamsy, R.A. Ackermann, and T.J. Havens. Making MRI quieter. *Magn Reson.Imaging*, 20:155–163, 2002.

G.F. Eden, J.E. Joseph, H.E. Brown, C.P. Brown, and T.A. Zeffiro. Utilizing hemodynamic delay and dispersion to detect fMRI signal change without auditory interference: the behavior interleaved gradients technique. *Magn Reson.Med.*, 41: 13–20, 1999.

W.B. Edmister, T.M. Talavage, P.J. Ledden, and R.M. Weisskoff. Improved auditory cortex imaging using clustered volume acquisitions. *Hum.Brain Mapp.*, 7:89–97, 1999.

D.N. Elliott and W.D. Fraser. *Foundations of Modern Auditory Theory*, volume I, chapter 4, pages 115–155. Academic Press New York and London, 1970.

M.R. Elliott, R.W. Bowtell, and P.G. Morris. The effect of scanner sound in visual, motor, and auditory functional MRI. *Magn Reson.Med.*, 41:1230–1235, 1999.

R.L. Fante. *Signal Analysis and Estimation: an introduction*, chapter 1, pages 20–21. John Wiley & Sons, 1988.

J.R. Foster, D.A. Hall, A.Q. Summerfield, A.R. Palmer, and R.W. Bowtell. Sound-level measurements and calculations of safe noise dosage during EPI at 3 T. *J.Magn Reson.Imaging*, 12:157–163, 2000.

F. Girard, V.L. Marcar, F. Hennel, and E. Martin. Anatomic MR images obtained with silent sequences. *Radiology*, 216:900–902, 2000.

X. Golay, K.P. Pruessmann, M. Weiger, G.R. Crelier, P.J. Folkers, S.S. Kollias, and

P. Boesiger. PRESTO-SENSE: an ultrafast whole-brain fMRI technique. *Magn Reson.Med.*, 43:779–786, 2000.

D.A. Hall, M.P. Haggard, M.A. Akeroyd, A.R. Palmer, A.Q. Summerfield, M.R. Elliott, E.M. Gurney, and R.W. Bowtell. "Sparse" temporal sampling in auditory fMRI. *Hum.Brain Mapp.*, 7:213–223, 1999.

D.A. Hall, A.Q. Summerfield, M.S. Goncalves, J.R. Foster, A.R. Palmer, and R.W. Bowtell. Time-course of the auditory BOLD response to scanner noise. *Magn Reson.Med.*, 43:601–606, 2000.

F.J. Harris. *Modern spectrum analysis, II*, pages 172–204. IEEE Press selected reprint series. IEEE Press, 1978. ISBN 0-87942-203-3.

L.M. Harris, S.R. Cumming, and R.G. Menzies. Predicting anxiety in magnetic resonance imaging scans. *Int.J.Behav.Med.*, 11:1–7, 2004.

R.A. Hedeen and W.A. Edelstein. Characterization and prediction of gradient acoustic noise in MR imagers. *Magn Reson.Med.*, 37:7–10, 1997.

F. Hennel. Fast spin echo and fast gradient echo MRI with low acoustic noise. *J.Magn Reson.Imaging*, 13:960–966, 2001.

F. Hennel, F. Girard, and T. Loenneker. "Silent" MRI with soft gradient pulses. *Magn Reson.Med.*, 42:6–10, 1999.

A. Jesmanowicz, P.A. Bandettini, and J.S. Hyde. Single-shot half k-space high-resolution gradient-recalled EPI for fMRI at 3 Tesla. *Magn Reson.Med.*, 40:754–762, 1998.

A. Katsunuma, H. Takamori, Y. Sakakura, Y. Hamamura, Y. Ogo, and R. Katayama. Quiet MRI with novel acoustic noise reduction. *MAGMA.*, 13:139–144, 2002.

L.E. Kinsler, A.R. Frey, A.B. Coppens, and J.V. Sanders. *Fundamentals of acoustics*, chapter 5, pages 113–133. John Wiley & Sons, Inc., 4th edition, 2000. ISBN 0-471-84789-5.

C. Kittel. *Introduction to solid state physics*, chapter 16. John Wiley & Sons, 7th edition, 1996.

A.H.W.M. Kuijpers. *Acoustic modeling and design of MRI scanners*. PhD thesis, Eindhoven University of Technology, The Netherlands, 1999.

T. Loenneker, F. Hennel, U. Ludwig, and J. Hennig. Silent BOLD imaging. *MAGMA.*, 13:76–81, 2001.

P. Mansfield, B.L. Chapman, R. Bowtell, P. Glover, R. Coxon, and P.R. Harvey. Active acoustic screening: reduction of noise in gradient coils by Lorentz force balancing. *Magn Reson.Med.*, 33:276–281, 1995.

P. Mansfield, P.M. Glover, and J. Beaumont. Sound generation in gradient coil structures for MRI. *Magn Reson.Med.*, 39:539–550, 1998.

P. Mansfield and B. Haywood. Principles of active acoustic control in gradient coil design. *MAGMA.*, 10:147–151, 2000.

P. Mansfield, B. Haywood, and R. Coxon. Active acoustic control in gradient coils for MRI. *Magn Reson.Med.*, 46:807–818, 2001.

V.L. Marcar, F. Girard, Y. Rinkel, J.F. Schneider, and E. Martin. Inaudible functional MRI using a truly mute gradient echo sequence. *Neuroradiology*, 44:893–899, 2002.

K. Mathiak, A. Rapp, T.T. Kircher, W. Grodd, I. Hertrich, N. Weiskopf, W. Lutzenberger, and H. Ackermann. Mismatch responses to randomized gradient switching noise as reflected by fMRI and whole-head magnetoencephalography. *Hum.Brain Mapp.*, 16:190–195, 2002.

A. Mazard, B. Mazoyer, O. Etard, N. Tzourio-Mazoyer, S.M. Kosslyn, and E. Mellet. Impact of fMRI acoustic noise on the functional anatomy of visual mental imagery. *J.Cogn Neurosci.*, 14:172–186, 2002.

M. McJury, A. Blug, C. Joerger, B. Condon, and D. Wyper. Short communication: acoustic noise levels during magnetic resonance imaging scanning at 1.5 T. *Br.J.Radiol.*, 67:413–415, 1994.

M. McJury and F.G. Shellock. Auditory noise associated with MR procedures: a review. *J.Magn Reson.Imaging*, 12:37–45, 2000.

M. McJury, R.W. Stewart, D. Crawford, and E. Toma. The use of active noise control (ANC) to reduce acoustic noise generated during MRI scanning: some initial results. *Magn Reson.Imaging*, 15:319–322, 1997.

C.K. Mechefske, R. Geris, J.S. Gati, and B.K. Rutt. Acoustic noise reduction in a 4 T MRI scanner. *MAGMA.*, 13:172–176, 2002a.

C.K. Mechefske, Y. Wu, and B.K. Rutt. Characterization of acoustic noise and magnetic field fluctuations in a 4 T whole-body MRI scanner. *Mechanical Systems and Signal Processing*, 16:459–473, 2002b.

C.K. Mechefske, Y. Wu, and B.K. Rutt. MRI gradient coil cylinder sound field simulation and measurement. *J.Biomech.Eng*, 124:450–455, 2002c.

A. Moelker, R.A. Maas, and P.M. Pattynama. Verbal communication in MR environments: effect of MR system acoustic noise on speech understanding. *Radiology*, 232:107–113, 2004.

A. Moelker and P.M.T. Pattynama. Acoustic noise concerns in functional magnetic resonance imaging. *Human Brain Mapping*, 20:123–141, 2003.

A. Moelker, M.W. Vogel, and P.M. Pattynama. Efficacy of passive acoustic screening: Implications for the design of imager and MR-suite. *J.Magn Reson.Imaging*, 17: 270–275, 2003a.

A. Moelker, P.A. Wielopolski, and P.M. Pattynama. Relationship between magnetic field strength and magnetic-resonance-related acoustic noise levels. *MAGMA.*, 16: 52–55, 2003b.

C. Oesterle, F. Hennel, and J. Hennig. Quiet imaging with interleaved spiral readout. *Magn Reson.Imaging*, 19:1333–1337, 2001.

A. Papoulis. *Signal analysis*, chapter 12, pages 379–380. Electrical & Electronic Engineering Series. McGraw-Hill, Inc., 1984. ISBN 0-07-048460-0.

C. Preibisch, U. Pilatus, J. Bunke, F. Hoogenraad, F. Zanella, and H. Lanfermann. Functional MRI using sensitivity-encoded echo planar imaging (SENSE-EPI). *Neuroimage.*, 19:412–421, 2003.

D.L. Price, J.P. De Wilde, A.M. Papadaki, J.S. Curran, and R.I. Kitney. Investigation of acoustic noise on 15 MRI scanners from 0.2 T to 3 T. *J.Magn Reson.Imaging*, 13:288–293, 2001.

K.P. Pruessmann, M. Weiger, M.B. Scheidegger, and P. Boesiger. SENSE: sensitivity encoding for fast MRI. *Magn Reson.Med.*, 42:952–962, 1999.

M.E. Quirk, A.J. Letendre, R.A. Ciottone, and J.F. Lingley. Anxiety in patients undergoing MR imaging. *Radiology*, 170:463–466, 1989a.

M.E. Quirk, A.J. Letendre, R.A. Ciottone, and J.F. Lingley. Evaluation of three psychologic interventions to reduce anxiety during MR imaging. *Radiology*, 173: 759–762, 1989b.

S. Ramamoorthy, K. Grosh, and T.G. Nawar. Structural acoustic silencers–design and experiment. *J.Acoust.Soc.Am.*, 114:2812–2824, 2003.

M.E. Ravicz and J.R. Melcher. Isolating the auditory system from acoustic noise during functional magnetic resonance imaging: examination of noise conduction through the ear canal, head, and body. *J.Acoust.Soc.Am.*, 109:216–231, 2001.

M.E. Ravicz, J.R. Melcher, and N.Y. Kiang. Acoustic noise during functional magnetic resonance imaging. *J.Acoust.Soc.Am.*, 108:1683–1696, 2000.

J.A. Sanders. *Functional Brain Imaging*, chapter 4, pages 145–186. Mosby-Year Book, Inc., 1995.

D.J. Schaefer, J.D. Bourland, and J.A. Nyenhuis. Review of patient safety in time-varying gradient fields. *J.Magn Reson.Imaging*, 12:20–29, 2000.

J.F. Schenck. Safety of strong, static magnetic fields. *J.Magn Reson.Imaging*, 12:

2–19, 2000.

V.J. Schmithorst and S.K. Holland. Event-related fMRI technique for auditory processing with hemodynamics unrelated to acoustic gradient noise. *Magn Reson.Med.*, 51:399–402, 2004.

N.J. Shah, S. Steinhoff, S. Mirzazade, O. Zafiris, M.L. Grosse-Ruyken, L. Jancke, and K. Zilles. The effect of sequence repeat time on auditory cortex stimulation during phonetic discrimination. *Neuroimage.*, 12:100–108, 2000.

F.G. Shellock. Radiofrequency energy-induced heating during MR procedures: a review. *J.Magn Reson.Imaging*, 12:30–36, 2000.

F.G. Shellock, G. Cosendai, S.M. Park, and J.A. Nyenhuis. Implantable microstimulator: magnetic resonance safety at 1.5 Tesla. *Invest Radiol.*, 39:591–599, 2004.

S.M. Shvartsman, R.W. Brown, Y.C. Cheng, T.P. Eagan, H. Fujita, M.A. Morich, L.S. Petropoulos, and J.D. Willig. Application of the SUSHI method to the design of gradient coils. *Magn Reson.Med.*, 45:147–155, 2001.

T.M. Talavage, W.B. Edmister, P.J. Ledden, and R.M. Weisskoff. Quantitative assessment of auditory cortex responses induced by imager acoustic noise. *Hum.Brain Mapp.*, 7:79–88, 1999.

H. Tanaka, N. Fujita, Y. Watanabe, N. Hirabuki, M. Takanashi, Y. Oshiro, and H. Nakamura. Effects of stimulus rate on the auditory cortex using fMRI with 'sparse' temporal sampling. *Neuroreport*, 11:2045–2049, 2000.

D.G. Tomasi and T. Ernst. Echo planar imaging at 4 Tesla with minimum acoustic noise. *Journal of Magnetic Resonance Imaging*, 18:128–130, 2003.

W.D. Tope and F.G. Shellock. Magnetic resonance imaging and permanent cosmetics (tattoos): survey of complications and adverse events. *J.Magn Reson.Imaging*, 15: 180–184, 2002.

C.M. Tsai and D.G. Nishimura. Reduced aliasing artifacts using variable-density k-space sampling trajectories. *Magnetic Resonance in Medicine*, 43:452–458, 2000.

J.L. Ulmer, B.B. Biswal, L.P. Mark, V.P. Mathews, R.W. Prost, S.J. Millen, J.N. Garman, and D. Horzewski. Acoustic echoplanar scanner noise and pure tone hearing thresholds: The effects of sequence repetition times and acoustic noise rates. *Journal of Computer Assisted Tomography*, 22:480–486, 1998.

S.M. van Netten. Laser interferometer microscope for the measurement of nanometer vibrational displacements of a light-scattering microspcopic object. *J. Acoust. Soc. Am.*, 83:1667–1674, 1988.

K. Wu, A. Schwinn, and H. Janocha. Active vibration control using embedded piezoceramics as both actuators and sensors. *Fith European Conference on Noise Control,*

Naples, Italy, 19-21 May, Paper ID: 369, 2003.

Y. Wu, B.A. Chronik, C. Bowen, C.K. Mechefske, and B.K. Rutt. Gradient-induced acoustic and magnetic field fluctuations in a 4T whole-body MR imager. *Magn Reson.Med.*, 44:532–536, 2000.

Y. Yang, A. Engelien, W. Engelien, S. Xu, E. Stern, and D.A. Silbersweig. A silent event-related functional mri technique for brain activation studies without interference of scanner acoustic noise. *Magn Reson.Med.*, 43:185–190, 2000.

G.Z. Yao, C.K. Mechefske, and B.K. Rutt. Characterization of vibration and acoustic noise in a gradient-coil insert. *MAGMA*, 17:12–27, 2004.

M. Young. *Optics and lasers, including fibers and optical waveguides*. Springer-Verlag Berlin Heidelberg New York, 5th edition, 2000.

Samenvatting

In de medische diagnostiek wordt veelvuldig gebruik gemaakt van beeldvormende technieken die werken met röntgenstraling (CT), positron emissie (PET) en magnetische resonantie (MRI). Het grote voordeel van MRI is dat deze techniek geen gebruik maakt van gevaarlijke ioniserende straling. Van het gebruik van MRI op levend weefsel zijn geen schadelijke gevolgen bekend; dat betekent echter niet dat iedereen in de scanner geplaatst kan worden voor onderzoek. Vanwege het sterke magneetveld mogen mensen met ferromagnetische metalen voorwerpen in het lichaam –ijzersplinters, implantaten, piercings, pacemakers– niet in de scanner geplaatst worden, dit vanwege de krachten die op deze voorwerpen uitgeoefend worden. Ook de gebruikte radiostraling kan inwerken op bijvoorbeeld tatoeages en implantaten waardoor deze opwarmen en brandwonden kunnen veroorzaken. Naast deze fysische beperkingen kunnen patiënten of proefpersonen fysiologische bijwerkingen ondervinden. Het snel schakelen van gradiëntmagneetvelden kan leiden tot zenuwstimulatie. Goede screening vooraf en het beperken van de schakelsnelheid zou alle voornoemde problemen moeten voorkomen. Echter, de nauwe buis en het harde geluid kunnen psychisch belastend zijn voor personen die gescand worden, en bovendien kan het harde geluid ook gehoorbeschadiging opleveren. Ook levert het harde geluid een auditieve stimulus die gemeten wordt tijdens functionele MRI (fMRI). Alle breinactiviteit die gemeten zal worden, is vervuild door het scannergeluid; dit is zeker het geval in onderzoek naar breinfunctie bij auditieve taken.

Het geluid van de scanner wordt veroorzaakt door krachten die op de gradiëntspoelen werken. Sterke electrische stromen door de gradiëntspoelen wekken een magnetisch veld op dat voor een gecontroleerde verandering van het hoofdmagneetveld zorgt. Door de verandering van magneetveldsterkte krijgen atoomkernen een andere resonantiefrequentie. De radiogolven die deze kernen dan kunnen absorberen en uitzenden, geven informatie over de aanwezigheid van kernen op een specifieke lokatie. Op deze manier kan frequentie-informatie omgezet worden naar lokatie-informatie en kunnen afbeeldingen gemaakt worden van de verdeling van bijvoorbeeld waterstofkernen. Dit levert de bekende MR-plaatjes op. Deze theorie is beschreven in **hoofdstuk 2**.

De wisselwerking tussen de sterke electrische stromen en het hoofdmagneetveld

wekt de krachten op die op de gradiëntspoelen werken. Deze Lorentzkrachten variëren met de stroomsterkte. De wisselende Lorentzkrachten veroorzaken trillingen die worden doorgegeven aan de hele scanner en ook aan de lucht. In **hoofdstuk 3** wordt de fysische achtergrond hiervan beschreven en verder ook de theorie die belangrijk is voor de rest van dit proefschrift.

De bovengenoemde effecten van het lawaai worden uitgebreider beschreven in **hoofdstuk 5**. In hetzelfde hoofdstuk wordt een analyse gemaakt van studies naar geluidsreducerende maatregelen. Eerst wordt een onderscheid gemaakt naar geluidsbronnen binnen de MR-kamer en daarna worden de verschillende reductiemethoden besproken. Geluidsreducerende maatregelen kunnen zowel passief als actief zijn. De passieve methoden variëren van oorpluggen en hoofdtelefoons tot het volledig isoleren van de scanner in schuimrubber of het vacuüm zuigen van de ruimte waar de gradiëntspoelen zich in bevinden. Elke methode kent zijn limieten, zowel in reductie als in het frequentiebereik waarbinnen de methode effect heeft. Hetzelfde geldt voor de actieve reductiemethoden. Actieve methoden zijn bijvoorbeeld het actief tegenwerken van de onstane Lorentzkrachten, of met anti-geluid het reeds ontstane geluid weer onderdrukken.

Er wordt in dit hoofdstuk ook een kritische blik geworpen op hoe de gemeten reductie bereikt wordt. Er blijken aanzienlijke verschillen te bestaan tussen de gerapporteerde experimentele meetopstellingen: de meetmicrofoon is geplaatst binnen in de scannerbuis, of juist ver buiten de buis; de reductie die opgegeven wordt, is vaak slechts gemeten voor één frequentie terwijl de breedbandige reductie juist van belang is.

Om de mogelijke reductie te bepalen, wordt vaak de overdrachtsfunctie van een scanner bepaald. Deze functie geeft de relatie tussen de gradiëntstroom en de geluidsdruk. Deze overdracht is over het algemeen laag voor lage frequenties en heeft een grillig verloop voor hogere frequenties. Karakteristiek voor de overdrachtsfunctie zijn enkele pieken die overeenkomen met resonantiefrequenties van het scannersysteem, met name die van de gradiëntspoelen. Met deze overdrachtsfunctie is het mogelijk om met de gradiëntstromen de geluidsdruk te voorspellen. Verschillende methoden om de overdrachtsfunctie te bepalen zijn te vinden in eerdere studies. Daar wordt gebruik gemaakt van ruis- en van (im)pulsoverdrachten, en ook wel van overdrachten met frequentie-gemoduleerde signalen.

In **hoofdstuk 6** wordt de toepassing van frequentie-gemoduleerde signalen uitgebreid geanalyseerd. De *sweep rate* –de verandering van frequentie per seconde– werd veranderd van klein tot zeer groot. De overdrachtsfuncties die hiermee bepaald kunnen worden verschillen voornamelijk voor de frequenties waar de overdracht laag is. Verder wordt er vastgesteld dat de overdracht afhankelijk is van de gradiëntstroomsterkte; dit is het geval voor de resonantiefrequenties maar ook weer voor de frequenties waar de overdracht laag is, onafhankelijk van de *sweep rate*. Deze waarnemingen leidden er toe een andere analysemethode te kiezen die meer aansluit bij de berekening van geluidsdrukniveaus (SPL = sound pressure level), na-

melijk door de geluidsdruk te middelen over de tijd. Zo worden alle frequenties in het geluidssignaal meegenomen, dit in tegenstelling tot het gebruik van de Fouriertransformatie waar alle frequenties gescheiden worden. Er wordt aangetoond dat niet-lineairiteiten een grote bijdrage leveren aan de geluidsdruk. Door Fouriertransformaties te gebruiken, worden deze niet-lineairiteiten niet meegenomen voor het bepalen van de overdracht. Dit leidt tot aanmerkelijke verschillen aangaande het voorspellen van de geluidsdruk. De voorgestelde methode, die met *sound pressure transfer function* aangeduid wordt, geeft een eenduidiger beeld voor de overdrachten, zowel aangaande *sweep rate* als aangaande gradiëntstroomsterkte.

Verder onderzoek wordt gepresenteerd in **hoofdstuk 7**. Er wordt een vergelijking gemaakt tussen de overdrachtsbepaling met ruis-, (im)puls- en frequentiegemoduleerde gradiëntstromen. Voor deze drie verschillende signalen worden overdrachtsfuncties bepaald met Fouriertransformaties en voor de frequentie-gemoduleerde stroom wordt ook de *sound pressure transfer function* bepaald. De verschillen tussen de *sound pressure transfer function* en de Fouriertransformatie bij het frequentie-gemoduleerde signaal zijn gelijk aan die in het vorige hoofdstuk. Voor alle methoden geldt dat de overdracht op resonantiefrequenties met vrijwel gelijke precisie bepaald kan worden. Om de MRI-scanner stiller te maken zijn we juist geïnteresseerd in de frequenties met lage overdracht. De overdracht zoals die bepaald is met de pulsrespons laat zeer lage overdrachten zien; deze zijn, zoals aangetoond in het vorige hoofdstuk, zeer onrealistisch. Verder is een piek zichtbaar die niet daadwerkelijk bestaat. Deze piek is een gevolg van de eindige lengte van de puls. De verschillen tussen de ruisrespons en de *sound pressure transfer function* van het frequentie-gemoduleerde signaal zijn vooral bij de lage frequenties te vinden. Doordat bij lage frequenties de overdracht laag is, wordt er daar vooral omgevingslawaai gemeten bij de *sound pressure transfer function*. De SPL hiervan is hoger dan die veroorzaakt door de gradiëntstroom. Bij de ruisrespons wordt al deze akoestische energie door de Fouriertransformatie verdeeld over het spectrum.

Hoe de overdrachtsfunctie ook bepaald wordt, het exacte scannergeluid kan niet worden voorspeld door de niet-lineairiteiten in de overdracht. De *sound pressure transfer function* is echter beter is staat om de geluidsdruk te voorspellen. Uit het verkregen signaal kan dan het te verwachten geluidsdrukniveau beter worden voorspeld; hierbij gaat het nadrukkelijk om de correcte voorspelling bij lage overdracht.

Een andere manier om het door de scanner geproduceerde geluid te voorspellen, is door modelleren. De scannerwanden trillen niet op elke plek op dezelfde manier, met dezelfde amplitude of niet-lineairiteiten. Om deze te kunnen invoeren in het model, moeten deze worden gemeten. Laser Doppler interferometrie is een manier om deze trillingen contactvrij te kunnen meten. Echter, deze methode is niet eenvoudig toe te passen in een omgeving waar veel trillingen zijn. In **hoofdstuk 8** van dit proefschrift worden voor- en nadelen van deze techniek geanalyseerd. Vanwege de gevoeligheid moet de uitlijning zeer nauwkeurig gebeuren. Dit uitlijnen vergt per meetpunt veel tijd. Het grootste nadeel van Laser Doppler interferometrie-metingen

is dan ook de totale tijd die nodig is voor het grote aantal benodigde meetpunten. De gegevens zouden behalve voor modelleren ook gebruikt kunnen worden om mogelijk lokaal geluids-/trillingsreducerende maatregelen te treffen.

Waargenomen geluid bereikt de cochlea niet alleen door het oorkanaal via geleiding door de lucht, maar ook via beengeleiding. Het hoofd dat op bed ligt dat aan de scanner is bevestigd zal ook via de schedel geluidstrillingen doorgeven. Alleen met een microfoon de overdracht meten, is daarom hoogstwaarschijnlijk niet voldoende. Wat in de toekomst nog moet gebeuren, is een perceptieve overdracht meten. In **paragraaf 9.2** wordt voorgesteld om dit te doen met een luidheidsvergelijkingstest.

Dankwoord

Tijdens mijn afstuderen werd een nieuwe studierichting geïntroduceerd: Biomedische Technologie. Het was te laat voor mij om dat alsnog te gaan studeren, maar de inhoud van BMT sprak mij wel aan. Toen heb ik al eens geïnformeerd naar de mogelijkheid om “dan maar” promotie-onderzoek te doen bij BMT. Later, tijdens de lerarenopleiding, heb ik mijn interesse voor het project aangaande geluid en MRI nogmaals laten blijken. Dat ik een proefschrift heb geschreven over dat onderwerp is uiteraard voornamelijk te danken aan mijn promotor. Alle anderen die hebben bijgedragen aan mijn AIO-periode wil ik hier ook bedanken.

Diek Duifhuis, allereerst heb je er voor gezorgd dat ik dit project kreeg. De scanner is nog niet stiller geworden, maar we hebben wel stappen in die richting gezet. Ik wil je bedanken voor alle vrijheid die je me gegeven hebt, vooral voor de ruimte die ik kreeg om vast te lopen. De hulp waar ik om vroeg, heb je me altijd gegeven en door jouw kritiek op mijn werk ben ik gegroeid.

Remco Renken, vanaf dag één was je mijn kamergenoot. Het kan niet anders dan dat je er op de laatste dag bij bent als paranimf. Van jou heb ik de beginselen geleerd van MRI, MATLAB, LabVIEW, alles wat ik nodig had voor de start van mijn project. Het zou verboden moeten worden om een AIO aan te stellen zonder de beschikbaarheid van een collega zoals jij.

Jelle Bezemer, elke week, dinsdagavond. Als we geen bijbelkring hadden, gingen we poolen. Eerst alle AIO-perikelen bespreken en dan alle frustraties van ons afstoten. Je hebt alle dieptepunten meegekregen, ik ben blij dat je als paranimf ook bij het hoogtepunt wilt zijn.

De komst van kamergenoten uit het buitenland bracht naast veel nadenken over de Nederlandse taal en cultuur ook veel afwisseling en plezier: Sonja Tomašković: hvala, Lavinia Slabu: multumesc, en Carlos Rizzo: gracias.

De eerste stappen op het gebied van digitale acquisitie heb ik gemaakt met Henk Hasper en zijn student Sander Knevelbaard. Mijn eerste eigen data heb ik verzameld in Eindhoven, met de scanner van het Magnetic Resonance Laboratory. Voor die mogelijkheid bedank ik Klaas Kopinga. Larry de Graaf, jij hebt veel werk verzet voor die metingen. Jouw hulp en aanwezigheid bij de metingen maakten de meetdagen nuttig en erg plezierig. Anita Kuiper en Hans Hoogduin, aangaande de scanner in

Groningen en de experimenten daar, hebben jullie me aldoor veel geholpen.

Edsger Smits heeft tijdens zijn stage metingen gedaan waar ik bij het opzetten van mijn experimenten veel aan heb gehad. Kees Smith, het is jammer dat we aan meten niet toe zijn gekomen. Jouw werk heeft wel de basis gelegd voor een van mijn hoofdstukken.

Tijdens het project is er voor verschillende aspecten van geluid en MRI contact geweest met mensen van Philips Medical Systems en Philips Centre for Manufacturing Technology. Ik ben vooral blij met de suggesties en hulp van Patrick Limpens en Paul Bunk. Verder wil ik Sander Slegt, Hans Tuithof, Peter van der Meulen, Bert Roozen, Jouke Smink, David Biloen, Chiel den Harder en Henk & Henk bedanken voor hun bijdragen.

Bij Biomedische Technologie hebben Esther Wiersinga, Ben Pijpker, Lambrecht Kok en alle studenten die bij BMT een stage deden, deze afdeling tot een plezierige omgeving gemaakt. De collegae van Neurobiofysica en het Neuroimaging Centrum hebben me op de verschillende werkplekken thuis laten voelen. Van deze mensen wil ik speciaal de secretaresses Annelies van Leeuwen, Aafke de Wolf en Tinie Alma bedanken voor alle kleine dingetjes die mijn werk aangenamer maakten. Dit geldt ook voor de AIO-coördinator Diana Koopmans en de belichaming van de onderzoeksschool BCN: Rob Visser.

Alle Meije Wink: dude! Koffiepauzes zijn de spaties in de zin van promotieonderzoek; Martijn Keitz, jij zorgde ervoor dat het leesbaar bleef. Ik was niet eenzaam tijdens de nachtelijke werkuren door de veelvuldige aanwezigheid van Christiaan van der Gaag.

Ruud Scheek wil ik bedanken voor het commentaar op mijn MRI-hoofdstuk.

Ich möchte gern den Leuten vom InterGK 'Neurosensorik' für die schönen und interessanten Meetings danken. Vielen Dank an Birger Kollmeier und Stefan Uppenkamp für die Einladung nach Oldenburg. Ferner möchte ich gern meinen Freunden Dirk und Ulrike danken, und insbesondere min skat Sandra.

Tenslotte wil ik mijn ouders, familie, vrienden en alle anderen bedanken die ervoor gezorgd hebben dat ik niet te veel in mijn werk opging. Ik heb nooit veel met jullie over mijn werk gepraat omdat dat er niet toe doet. Anderzijds heb ik dit werk wel kunnen doen door jullie aanwezigheid in mijn leven.

Explicit. Laus Deo.